Evaluation of Ground-Based Interferometric Radar for Civil Engineering Applications

---

A Thesis presented to
the Faculty of the Graduate School
at the University of Missouri-Columbia

In Partial Fulfillment
of the Requirements for the Degree

Master of Science

---

by

WYATT S. JENKINS, BSCE, EIT

Dr. Brent L. Rosenblad, Thesis Supervisor

JULY 2013

The undersigned, appointed by the Dean of the Graduate School, have examined the thesis entitled

EVALUATION OF GROUND-BASED INTERFEROMETRIC RADAR
FOR CIVIL ENGINEERING APPLICATIONS

Presented by Wyatt S. Jenkins, BSCE, EIT,

a candidate for the degree Master of Science in Civil Engineering,

and herby certify that, in their opinion, it is worth of acceptance

_____
Professor Brent L. Rosenblad, PhD

_____
Professor J. Erik Loehr, PhD, PE

_____
Professor Francisco Gomez, PhD

“It's a dangerous business, Frodo, going out your door. You step onto the road, and if you don't keep your feet, there's no knowing where you might be swept off to.”

-J.R.R. Tolkein

ACKNOWLEDGEMENTS

I would like to thank Dr. Rosenblad, my advisor, for his continuous support and encouragement during research campaigns as well as during the thesis process. He has been extremely patient during the steep learning curve required for this work and always willing to help. Dr. Rosenblad has encouraged me to think critically about my research topic and made me a better professional for it.

I would also like to thank Dr. Bowders and Dr. Loehr for their constant attention to research as well as academics. They were always willing to put in extra effort to make sure that each student understood every aspect of a particular topic. Dr. Bowders has been a great personal mentor to me and always willing to discuss life outside the classroom. I would like to thank Dr. Loehr for believing in me some years ago and willing to take a chance on a student who went through a difficult period.

I would like to thank Dr. Gomez for serving on my committee. Dr. Gomez devoted great amounts of time in order to teach me about complex research concepts and was always extraordinarily patient. I would also like to thank him for showing me how to be a true scientist. In addition, I would like to thank Dr. Legarksy for providing technical assistance during my research as well as being an excellent professor in the classroom.

I would like to thank Bjorn Held and Huazeng Deng for research assistance during my fieldwork. Specifically, I would like to thank Bjorn for his camaraderie during my research work. In addition, I would like to thank Joey Cochran, Nathan Hinrichs, Taehoon Kim, and Tayler Day for their assistance during my many research trips.

The funding for this work was provided by the National Science Foundation Grant No. 0923086 as part of the Major Research Instrumentation (MRI) program. The University of Missouri Research Board provided additional funding. I would like to thank both of them for supporting this academic endeavor. The United States Army Corps of Engineers-Kansas City District, Colorado Department of Transportation, and the City of Columbia provided access to many of the sites presented in thesis. Each of the aforementioned entities were accommodating with my many requests and I thank them all for their assistance.

I would like to thank each of my colleagues in the Geotechnical Engineering Group. I would not have succeeded without each and every person's constant support and counsel. Our student group, MUGEO, is acknowledged for providing many opportunities to interact with professional organizations and engage in academic forums. The Civil Engineering Department staff, particularly Connie Taylor and Mary McCush are acknowledged for clerical excellence. Finally, I would like to thank my friends, both here and abroad, and my family for their constant encouragement throughout my research. I would not have been able to complete this work without their constant backing and support.

TABLE OF CONTENTS

ACKNOWLEDGEMENTS ii
LIST OF FIGURES vii
LIST OF TABLES xii
ABSTRACT xiii
Chapter 1: Introduction 1
1.1 Background 1
1.2 Project Motivation and Research Objectives 3
1.3 Organization of Thesis 4
Chapter 2: Overview of Radar and Radar Interferometry 5
2.1 Radar Background 5
2.2 Radar Fundamentals 7
2.2.1 Frequency Modulated- Continuous Wave (FM-CW) Radar 11
2.3 Differential Radar Interferometry 14
2.4 Radar Interferometry Processing Steps 16
2.4.1 Image Coregistration and Resampling 17
2.4.2 Interferogram Generation 17
2.4.3 Coherence Estimation 18
2.4.4 Filtering Processes 19
2.4.5 Interferogram Unwrapping 20
2.4.6 Removing Atmospheric Effects 23
2.5 Summary 25
Chapter 3: Ground-Based Interferometric Radar 27
3.1 Introduction 27
3.2 Ground-based Interferometric Radar Systems 27
3.2.1 Ground Probe 27
3.2.2 IBIS-L 28
3.2.3 GAMMA Remote Sensing 29
3.3 GBIR System at the University of Missouri 30

3.4 Literature Review of Past Applications of GBIR 35
3.5 Motivation for Proposed Study 41
Chapter 4: Monitoring of a Rock Slope 42
4.1 Introduction 42
4.2 Description of Field Site and Experimental Procedures 42
4.2.1 Field Site Description and Data Collection Procedures 42
4.2.2 Data Processing Procedures 46
4.3 Results and Discussion of Displacement Measurements 48
4.3.1 Results of Displacement Measurements 48
4.3.2 Discussion of Displacement Measurements 57
4.4 Results and Discussion Coherence Measurements 60
4.4.1 Coherence Measurement Results 60
4.4.2 Discussion of Coherence Measurement Results 65
4.5 Summary and Conclusions 66
Chapter 5: Long-term Monitoring of an Earth Dam 68
5.1 Introduction 68
5.2 Description of Field Site and Measurement Procedures 69
5.2.1 Field Site Description and Data Collection Procedures 69
5.2.2 Processing Procedures 74
5.3 Field Measurement Results and Discussion 81
5.3.1 Interferometric Phase Measurements 82
5.3.2 Discussion of Interferometric Phase Measurements 88
5.3.3 Coherence Measurements 90
5.3.4 Coherence Measurements Discussion 99
5.3.5 Discussion of Processing Issues using Post-Unwrapping Stacking Method .. 100
5.4 Summary and Conclusions 104
Chapter 6: Monitoring Thermal Expansion of a Geosynthetic Landfill Liner 107
6.1 Introduction 107
6.2 Description of Landfill Site 108
6.3 Data Collection Procedures 110
6.4 Data Processing Procedures 111

6.5 Field Measurement Results 112
6.6 Discussion of Field Measurements from Landfill Liner 121
6.7 Summary and Conclusions 124
Chapter 7: Conclusions and Future Work 126
7.1 Summary 126
7.2 Conclusions 127
7.3 Recommendations 129
REFERENCES 131
APPENDIX 136

LIST OF FIGURES

Figure 2.1 The electromagnetic spectrum 6

Figure 2.2 Illustration of range resolution between two radar targets for a given pulse envelope 9

Figure 2.3 Schematic of resolution parameters for a satellite-based system imaging a target area 10

Figure 2.4 Linear FM-CW signal showing transmitted (red) and received (green) signal 12

Figure 2.5 Block diagram of a FM-CW radar system 13

Figure 2.6 Ground-based radar acquisitions of an earth dam at two times (t_1,t_2), showing phase difference resulting from surface deformation occurring between acquisition times. 15

Figure 2.7 Schematic of general interferometric processing flow. 16

Figure 2.8 Example of an interferogram presented in terms of (a) wrapped phase and (b) unwrapped phase 23

Figure 2.9 Example of atmospheric ramps in interferogram data using a (a) satellite-based radar platform, acquired over one-day (Li, et al., 2007) and (b) ground-based radar device, acquired over several hours. 25

Figure 3.1 GroundProbe SSR device deployed at open pit mine site 28

Figure 3.2 Photo of IBIS-L system applied to monitoring of a concrete dam 29

Figure 3.3 GAMMA Remote Sensing ground based system, GPRI-I 30

Figure 3.4 Photograph of the Ku-band system with major system components identified overlooking a rockfill dam in Colorado. 31

Figure 4.1 Google Earth image of the Glenwood Canyon site in relation to Denver, CO. 44

Figure 4.2 Expanded view of the Google Earth image of Glenwood Canyon showing area of interest (white circle) and radar measurement location (red arrow). 44

Figure 4.3 Rock slope of interest in Glenwood Canyon, CO. 45

Figure 4.4 Panoramic view from radar location. Red circle indicates primary site of interest. 45

Figure 4.5 Aerial photo with superimposed line-of-sight deformation map from May 15, 2012 to May 30, 2012 using (a) 1-inch/cycle scale and (b) ¼-inch/cycle scale. Red circle indicates primary site of interest. 50

Figure 4.6 Line-of-sight deformation map from May 15, 2012 to May 30, 2012 superimposed over a LiDAR DEM model using (a) 1-inch/cycle scale and (b) ¼-inch/cycle scale. 51

Figure 4.7 Aerial photo with superimposed line-of-sight deformation map from May 30, 2012 to June 12, 2012 using (a) 1-inch/cycle scale and (b) ¼-inch/cycle scale. Red circle indicates primary site of interest. 52

Figure 4.8 Line-of-sight deformation map from May 30, 2012 to June 12, 2012 superimposed over a LiDAR DEM model using (a) 1-inch/cycle scale and (b) ¼-inch/cycle scale 53

Figure 4.9 Aerial photo with superimposed line-of-sight deformation map from May 15, 2012 to June 12, 2012 showing (a) 1-inch scale and (b) ¼-inch scale. Red circle indicates primary site of interest. 54

Figure 4.10 Line-of-sight deformation map from May 15, 2012 to June 12, 2012 superimposed over a LiDAR DEM model using (a) 1-inch/cycle scale and (b) ¼-inch/cycle scale. 55

Figure 4.11 Unwrapped interferograms from May 15-May 30, 2012 timespan with a) atmospheric contribution and b) with atmospheric contribution removed 56

Figure 4.12 Average coherence image from imagery collected (a) between 5 minutes and 3 hours on May 15, 2012 (b) between May 15 and May 30, 2012 and (c) between May 15 and June 12, 2012 acquisitions. Areas of higher coherence are shown with yellow and areas of low coherence are shown with blue. Moderate coherence areas are denoted with purple, and black is zero coherence. 62

Figure 4.13 Intensity image of a May 15 radar acquisition with monitored coherence areas indicated. 63

Figure 4.14 Coherence values over different short-term acquisition intervals computed using May 15, 2012 as scene master. 63

Figure 4.15 Averaged coherence values from over different data collection intervals at Glenwood Canyon, computed using May 15, 2012 scene master 64

Figure 4.16 Coherence values versus number of images stacked from May 15-May 30, 2012 dataset. 64

Figure 5.1 Google Earth image of the Milford dam location in relation to Junction City, Kansas. 71

Figure 5.2 Google earth image of Milford Dam showing radar locations relative to dam structures. 72

Figure 5.3 Photograph of Milford Dam taken from the vantage point of Location 2..... 72

Figure 5.4 Reservoir pool elevation at Milford Dam over the timespan of GBIR measurements. 73

Figure 5.5 Radar interferogram image of Milford Dam acquired from Loc. 2 and superimposed on image of the dam. 81

Figure 5.6 Stacked and unwrapped interferograms, using a September 2011 master 83

Figure 5.7 Stacked and unwrapped interferograms, using a September 2011 master, acquired at Loc. 2 84

Figure 5.8 Stacked and unwrapped interferograms, using an October 2011 master, acquired at Loc. 1 using the Ku-band device 85

Figure 5.9 Stacked and unwrapped interferograms, using an October 2011 master, acquired at Loc. 2 using the Ku-band device 86

Figure 5.10 Stacked and unwrapped interferograms, using an October 2011 master, acquired at Loc. 2 using the C-band device 87

Figure 5.11 Example demonstrating different look angles along the dam face, from Loc. 1, as the radar sweeps over the dame face. View "A" would be most sensitive to deformation, while View C, would be the least sensitive to horizontal deformation of the embankment dam. 89

Figure 5.12 Radar intensity image with coherence locations marked for (a) Loc. 1 and (b) Loc. 2 at Milford Dam 92

Figure 5.13 Stacked coherence imagery, using a September 2011 master, acquired at Loc. 1 using the Ku-band device 93

Figure 5.14 Stacked coherence imagery, using a September 2011 master, acquired at Loc. 2 using the Ku-band device 94

Figure 5.15 Time-dependent coherence derived using the September master (Ku-band) for (a) short and (b) long terms at Loc. 1 and 2 95

Figure 5.16 Stacked coherence imagery, using an October 2011 master, acquired at Loc. 2 using the Ku-band device over different timespans: (a) minutes, (b) 1-month, (c) 4-months. Yellow areas represent coherence values from 0.7-1.0, purple represents values from 0.4-0.7, blue represents values from 0.0-0.4, and black represents areas of zero coherence. 96

Figure 5.17 Stacked coherence imagery, using an October 2011 master, acquired at Loc. 2 using the C-band device over different timespans: (a) minutes, (b) 1-month, (c) 4-months. Yellow areas represent coherence values from 0.7-1.0, purple represents values from 0.4-0.7, blue represents values from 0.0-0.4, and black represents areas of zero coherence. 97

Figure 5.18 Time-dependent coherence derived using an October master for (a) short and (b) long terms using C-band, and (c) short and (d) long term coherence using Ku-band at Loc. 2 98

Figure 5.19 Example of failed post-unwrapped interferogram. Unwrapping error is shown inside the black circle. 102

Figure 5.20 Example of single wrapped interferogram with an atmospheric ramp. Black circle indicates area where dropped data points create area where unwrapping program failed. 103

Figure 5.21 Complex interferograms input into first pre-unwrapping procedure stacking attempt (September-October 2011 timespan) 104

Figure 6.1 Google Earth image of the landfill complex with the area of interest (i.e. Cell 5) denoted with a red rectangle. Landfill Cells 4 and 5 are denoted by red boxes, and the observation location of the radar device is indicated with a black arrow. 109

Figure 6.2 Looking onto the site of interest (Cell 5) from Cell 4. The black surfaces are areas of the compacted clay liner overlain with geosynthetic material 109

Figure 6.3 Photo taken prior to placement of geosynthetic in Cell 5 (near ground) with future location of the GBIR on Cell 4 indicated. 111

Figure 6.4 Radar intensity image with areas of the landfill liner denoted. 113

Figure 6.5 Photographs of (a) left side “Side A” and (b) right side “Side B” of landfill geosynthetic liner. Photographs collected days after radar imagery collection. . 114

Figure 6.6 Zoomed-in view of geosynthetic liner, showing drainage trenches with sandbags in the trenches restraining movement of the liner. 114

Figure 6.7 Ambient air temperature and relative humidity logged at radar location during September 8, 2011 landfill acquisition. Time zero is at 6:50 AM. 115

Figure 6.8 Unwrapped interferograms at 5 minutes, 30 minutes and 55 minutes after time zero, without atmospheric trend removed (a-c) and with atmospheric trend removed (d-f) 116

Figure 6.9 Zoomed-in view of Figure 6.8 capturing landfill liner at different acquisition times, relative to the time zero: (a) 5 minutes, (b) 15 minutes, (c) 20 minutes, (d) 25 minutes, (e) 30 minutes, (f) 35 minutes, (g) 40 minutes, (h) 45 minutes, (i) 50 minutes. Drainage trench 119

Figure 6.10 Spatial coherence of the entire scene at: (a) 5 minutes, (b) 15 minutes, (c) 20 minutes, (d) 25 minutes, (e) 30 minutes, (f) 35 minutes, (g) 40 minutes, (h) 45 minutes, (i) 50 minutes. Yellow areas represent coherence values from 0.7-1.0, purple represents values from 0.4-0.7, blue represents values from 0.0-0.4, and black represents areas of zero coherence. 120

Figure 6.11 Intensity image acquired on September 8, 2011 with areas of monitored coherence indicated..... 121

Figure 6.12 Coherence values for selected points on landfill liner over acquisition period. All points are on landfill liner, and are referenced in Figure 6.11. 121

Figure 6.13 Geosynthetic liner effects near drainage trenches. After Take et al. (2012). 122

LIST OF TABLES

Table 2.1 Letter designation for different microwave frequency bands and corresponding wavelengths..... 7

Table 2.2 Selected values of RCS at microwave frequencies..... 14

Table 3.1 Performance Specifications for the Ku-Band and C-Band GBIR Systems..... 33

Table 3.2 Performance specifications for radar devices discussed in Chapter 3..... 34

Table 3.3 Summary of selected previous GBIR studies of note presented in this chapter 40

Table 4.1 Date of data acquisitions and number of images acquired during surveys campaigns in Glenwood Canyon, CO..... 46

Table 4.2 Details of Glenwood Canyon processing for each measurement interval..... 48

Table 4.3 Number of interferograms generated and stacked at Glenwood Canyon..... 48

Table 5.1 Milford dam pool elevations on dates of data acquisition..... 74

Table 5.2 Acquisition dates using the Ku-band system..... 74

Table 5.3 Acquisition dates using the C-band system..... 74

Table 5.4 Processing information for data collected at Location 1 at Milford Dam using Ku-Band..... 78

Table 5.5 Processing information for data collected Location 2 at Milford Dam using Ku-Band..... 79

Table 5.6 Processing information for data collected at Location 2 at Milford Dam using C-Band..... 80

Table 6.1 Processing details for Columbia Landfill data..... 112

Table A.1 Coordinates for radar observation locations presented in this thesis.....136

EVALUATION OF GROUND-BASED INTERFEROMETRIC RADAR FOR CIVIL ENGINEERING APPLICATIONS

Wyatt S. Jenkins

Dr. Brent L. Rosenblad, Thesis Supervisor

ABSTRACT

The ability to measure and monitor deformations of civil engineering structures is important for verifying acceptable in-situ performance and detecting unexpected or unsafe conditions. Ground-based interferometric radar (GBIR) is an emerging technology that offers several advantages over satellite-based measurements for civil engineering applications. The objective of this research is to evaluate and document the performance of GBIR for civil engineering applications that are not well represented in the current literature. These applications include using GBIR to: (1) monitor and detect movements of unstable rockslopes, (2) perform periodic deformation monitoring of earth dams, and (3) measure thermal movements of a geosynthetic landfill liner during construction. Field measurements were conducted at three sites over time spans that ranged from minutes (landfill site) to several months (dam site). Changes in signal coherence for different surface materials were quantified and are presented for short (minutes to hours), intermediate (days to weeks) and long time spans (weeks to months). High coherence values were maintained from the rockslope and riprap materials, indicating that GBIR is a viable technique for repeat-setup monitoring of these sites over month long or greater intervals. Coherence from the landfill liner decreased greatly over the two-hour time span, likely due to changes in the shape and backscattering characteristics of the liner, indicating that GBIR may not work well for monitoring large movements of the landfill liner. Results from applying standard interferometric

processing methods are presented, as well as a discussion of processing pitfalls and strategies for these unique applications.

Chapter 1: Introduction

1.1 Background

Geotechnical engineers are responsible for ensuring that constructed facilities operate safely and effectively, and natural sites, such as earth and rock slopes, do not pose a hazard to the public. Measurements of surface deformations provide valuable information to the engineer regarding the performance and safety of these sites. Historically, surface movements of civil structures have been measured using conventional optical surveying techniques. One drawback of these traditional methods is that they only sample discrete points and do not provide a complete picture of the movements. In recent years, civil engineers have begun to adopt new imaging technologies for deformation measurements. One such emerging technology is interferometric radar.

Using interferometric radar for deformation measurements involves acquiring radar imagery of the same scene at two different times. The radar returns are mathematically combined to detect changes in the phase of the radar returns caused by changes in the source to reflector distance. Phase changes can be related to very small (mm-scale) line-of-sight movements occurring between the measurement times. The radar scans the region of interest resulting in a two-dimensional map of line-of-sight movements of coherent reflectors in the scanned region.

Interferometric radar measurements from satellite-based platforms have been successfully used for many years. Satellite-based platforms capture radar returns from large areas (100 km by 100km) during image acquisitions, with ground pixel sizes on the

order of 5 m to 20 m. Much of the focus of satellite-based measurements has been on large spatial scale (km) geological applications, such as ground subsidence from oil, and water extraction and earthquake movements (Fielding, et al., 1998, Stramondo, et al., 2005). Satellite-based measurements have also been studied for civil engineering applications; such as movements of dams and tunnels, with some success (Coffman, 2009). However, in many ways satellite-based measurements are not ideal for monitoring civil engineering structures, due to: long repeat times (weeks to months) between acquisitions, limited viewing geometry options (near vertical), and data processing challenges for detecting small spatial scale movements.

In recent years, there has been interest in applying radar interferometry from ground-based platforms, which could overcome many of the limitations of satellite-based measurements. Ground-based interferometry is still an emerging technology and is not routinely used in civil engineering practice. Studies of the performance of ground-based radar for full-scale civil engineering applications are sparse in the literature. There is a need for basic studies documenting the performance of ground-based interferometric radar for short (days) to long-term (months to years) monitoring of civil and geotechnical engineering applications. The University of Missouri, in collaboration with GAMMA Remote Sensing, recently completed a Major Research Instrumentation (MRI) project funded by the National Science Foundation (NSF) to develop a unique ground-based interferometric radar system. This thesis reports on results and findings from initial studies performed with this equipment at diverse geotechnical sites.

1.2 Project Motivation and Research Objectives

Ground-based interferometric radar has the potential to provide engineers with new insights into the performance and safety of civil and geotechnical engineering structures which cannot be attained with existing systems. Widespread adoption of GBIR by engineers requires an understanding of the performance capabilities and limitations for a wide range of materials and applications. Geotechnical engineers deal with a variety of natural (soil, rock) and man-made (concrete, steel, geosynthetics) materials, and require deformation information over time scales that may range from minutes to years. The primary motivation of this study was the need for GBIR performance data collected at diverse civil engineering sites and over variable measurement time scales. The published literature on GBIR for civil engineering applications is sparse and is dominated by slope stability applications. In addition, most of the published studies are from GBIR applied using a continuous equipment deployment over relatively short time spans (days to weeks).

The overall objective of this research is to evaluate and document the performance of GBIR for civil engineering applications that are not well represented in the current literature. These applications include using GBIR to: (1) monitor and detect unstable rockslopes, (2) perform periodic deformation monitoring of earth dams, and (3) measure thermal movements of a geosynthetic landfill liner during construction. The specific objectives of this research were to:

1. Quantify changes in coherence over short (minutes to hours), intermediate (weeks), and long (several months) time frames for a range of materials and sites using the Ku-band radar,

2. Assess the viability of using repeat setup data collection for long-term monitoring of earth dams,
3. Identify pitfalls in conventional data processing methods and evaluate data processing strategies to develop reliable interferograms at these sites,
4. Compare the performance of C-band and Ku-band systems for long-term monitoring of earth dams.

1.3 Organization of Thesis

This thesis is comprised of seven chapters. Chapter 1 (current chapter) presents an introduction to the project research, describes project motivations, and research objectives. Chapter 2 is a brief overview of radar methodologies generally used by satellite platforms and ground-based platforms, with an emphasis on ground-based platforms. Chapter 3 is an overview of engineering applications related to ground-based radar, which discusses commercial ground-based radar systems, the system used in this project, and a review of the current literature on GBIR applied to civil engineering problems. The methods, results and findings are presented together in separate chapters for each field study. The rockfall study is presented in Chapter 4, the earth dam study is presented in Chapter 5, and the landfill liner study is presented in Chapter 6. Conclusions and recommendations for future work are presented in Chapter 7.

Chapter 2: Overview of Radar and Radar Interferometry

2.1 Radar Background

A radar system is a device that uses electromagnetic waves for detection, tracking, or imaging purposes (Richards, 2005). The term radar originated as a covert code name used for detection and tracking technology created as a defensive measure during World War II (Skolnik, 2001). Over the years the military code name for the secret weapon, which is an acronym for Radio Detection and Ranging, remained as the name of the technology. Radar systems generally operate in the microwave region of the electromagnetic spectrum (Figure 2.1 and Table 2.1). Successful development of radar technology was based on prior decades of research on electromagnetic wave propagation by many scientists, such as Hertz and Tesla (Richards, 2005). After the war, scientists focused on applying radar for useful peacetime purposes such as astronomical object tracking, metrological events (Skolnik, 2001), and transportation safety issues (Meinel, 1995).

With the advent of space technology, radar systems were mounted on satellite platforms, which allowed monitoring of the earth from space (Richards, 2005). The first radar system to be combined with a satellite platform was the Seasat system in 1978, which was tasked with studying the world's oceans (Hanssen, 2010). The Seasat system operated in the L-band frequency range, which is the lower range of frequencies (i.e. longer wavelength) in the microwave spectrum (Table 2.1).

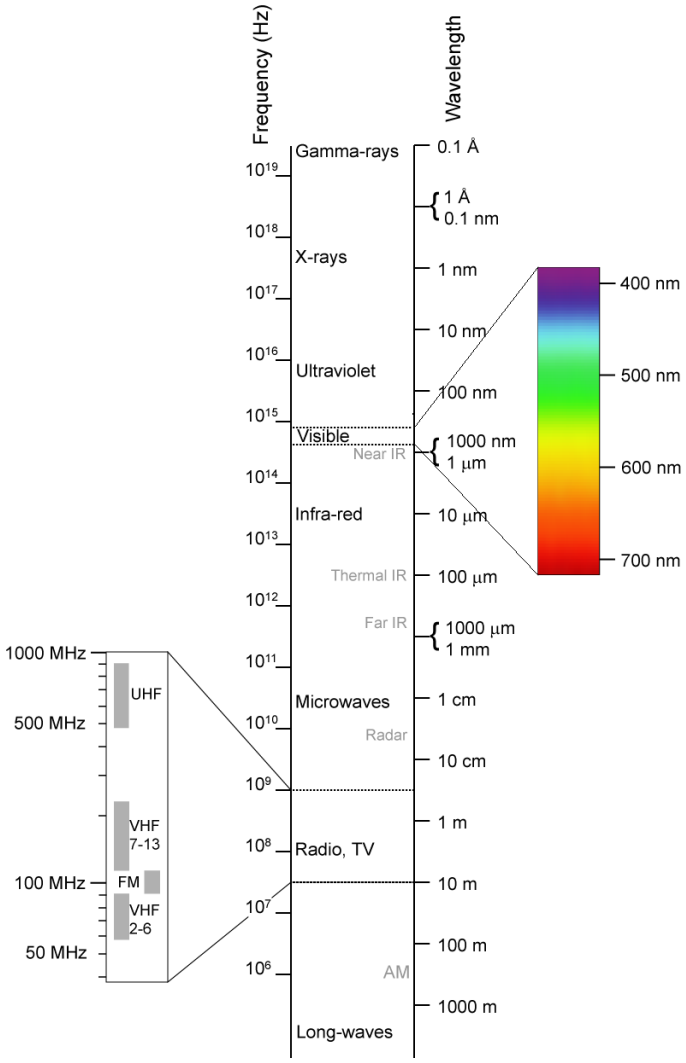

Figure 2.1 The electromagnetic spectrum (Blacus, 2012)

Table 2.1 Letter designation for different microwave frequency bands and corresponding wavelengths

Band	Frequency Range	Wavelength Range
HF	3 - 30 MHz	100 m - 10 m
VHF	30 - 300 MHz	10 m - 1 m
UHF	300 MHz - 1 GHz	1 m - 30 cm
L	1 - 2 GHz	30 cm - 15 cm
S	2 - 4 GHz	15 cm - 7.5 cm
C	4 - 8 GHz	7.5 cm - 3.75 cm
X	8 - 12 GHz	3.75 cm - 2.5 cm
Ku	12 - 18 GHz	2.5 cm - 1.67 cm
K	18 - 27 GHz	1.67 cm - 1.11 cm
Ka	27 - 40 GHz	1.11 cm - 7.5 mm
mm	40 - 300 GHz	7.5 mm - 1 mm

2.2 Radar Fundamentals

Radar systems operate by emitting a signal in the microwave frequency band and then receiving the reflected arrival of the signal from the targets of interest. Radar systems are used to determine the range distance (R) between the source and an object by using the speed of light (c) and measuring the two-way travel time of the radar signal (t_0). The equation to calculate the range distance is:

$$R = \frac{c \times t_0}{2} \tag{2.1}$$

An important concept for understanding the capabilities and limitations of radar imaging is the idea of the *resolution cell*. A resolution cell is an area on the target that contributes to the return echo for any given instant in time (Richards, 2005). The size of the resolution cell in the range direction (direction looking out from the radar) is called the *range resolution* and indicates the ability of the radar to distinguish separate objects in the range direction. For example, consider Figure 2.2 where two reflectors are shown separated by a distance of ΔR in the range direction. If the range resolution is larger than ΔR it will not be possible to distinguish these two objects (i.e. they will appear as a single radar return). The range resolution depends only on the pulse envelope (i.e. pulse length), τ, and the speed of light (c), as presented in Eq. 2.2. Increasing the pulse length increases the range resolution of a cell, thereby decreasing the ability to distinguish closely spaced objects. The size of the resolution cell in the cross-range direction is called the *azimuthal resolution*. As shown in Eq. 2.3, the azimuthal resolution is dependent on the slant range (line-of-sight distance from radar to target), ρ, and antenna beamwidth, β_{az}. Antenna beamwidth is a quantitative assessment of an antenna's radiation pattern. The half-power beamwidth is the angle (expressed in degrees or radians) for which the power of the main lobe of the radiation pattern is one-half of its greatest value. To illustrate azimuth resolution, consider Figure 2.2 but assume the reflectors are now positioned in a line that is perpendicular to the range direction. The azimuth resolution must be smaller than the distance between the reflectors for the radar to distinguish between the two reflectors. While the slant range parameter will depend on

the radar's proximity to the target, the antenna beamwidth is constant for a given device. Therefore, as the slant range distance increases the azimuth resolution parameter will also increase (yielding poorer resolution). It is important to understand that the range and azimuth resolutions presented are only valid for a flat surface. Since radar devices are not often operated on flat ground, it is necessary to calculate the *ground-resolution*, (*r*) as presented in Eq. 2.4 and 2.5. These equations include the angle of inclination (θ) between the radar transmitter relative to a sloping ground surface.

$$r_r = \frac{c \times \tau}{2} \tag{2.2}$$

$$r_{az} = \rho \times \beta_{az} \tag{2.3}$$

$$r_{ground-range} = \frac{c \times \tau}{2 \times \sin\theta} \tag{2.4}$$

$$r_{ground-azimuth} = \frac{\rho \times \beta_{az}}{\sin\theta} \tag{2.5}$$

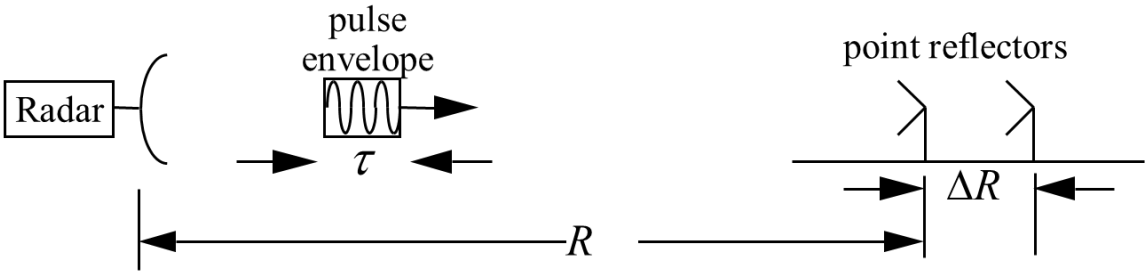

Figure 2.2 Illustration of range resolution between two radar targets for a given pulse envelope (Richards, 2005)

A schematic showing a ground resolution cell for a satellite-based platform is presented in Figure 2.3. The diagram presented in Figure 2.3 is for a radar satellite platform that operates as a synthetic aperture radar (SAR), meaning that the system synthesizes a larger aperture (length L in Figure 2.3) and narrow beamwidth by mathematically combining imagery from multiple acquisitions along the measurement path to improve the spatial resolution of the image. In contrast, real aperture systems use only acquisitions from a single vantage point with the resulting azimuthal resolution controlled by the attributes of the radar device (e.g. length, radar frequency). The radar system utilized in this study is a real-aperture ground-based system, which uses frequency-modulated-continuous wave (FM-CW) radar, as explained in the next section.

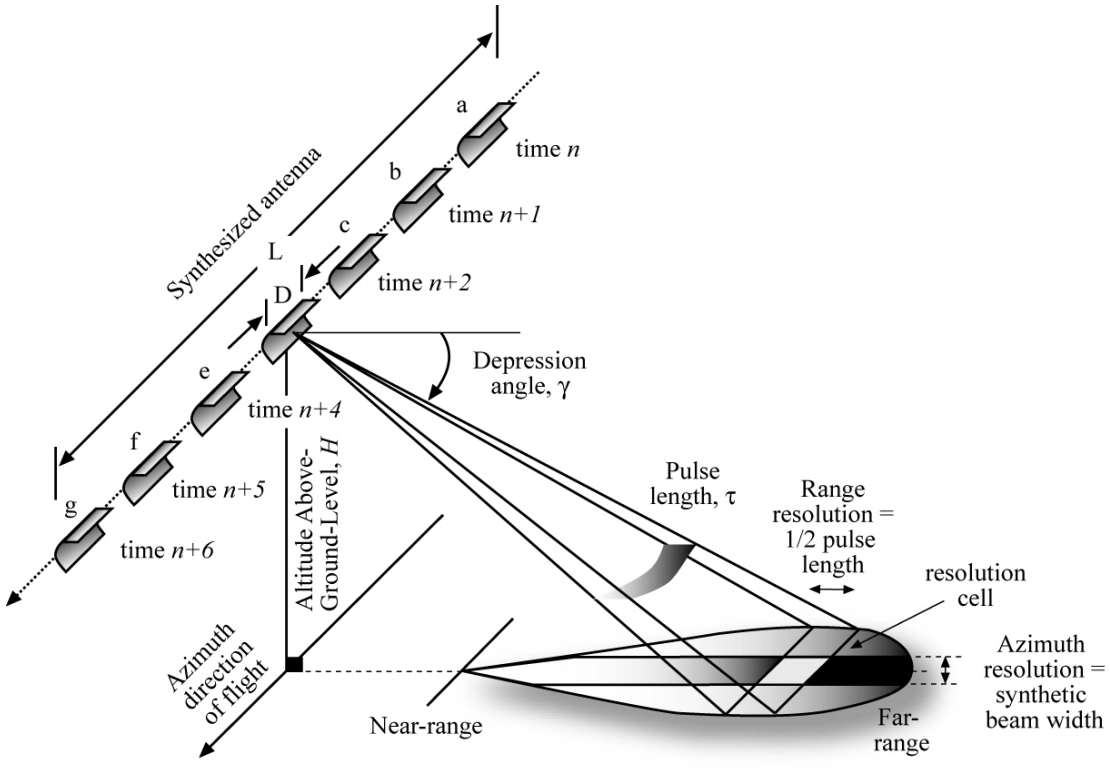

Figure 2.3 Schematic of resolution parameters for a satellite-based system imaging a target area. (Jensen, 2000)

2.2.1 Frequency Modulated- Continuous Wave (FM-CW) Radar

The radar used in this study is a common type of radar system called Frequency-Modulated Continuous Wave (FM-CW) radar. The FM-CW system operates by using a linear modulation technique, where the operating frequency of the radar is swept over a certain range, as illustrated in Figure 2.4. The range over which the frequency is changed (termed bandwidth, *B*) controls the range resolution when using the FM-CW approach (Eq. 2.6). The azimuth resolution is still controlled by the antenna beamwidth, which is specific to each type of antennae. Frequency Modulated-Continuous Wave devices perform well at close ranges where the reflected signal is received during transmission of the signal, as shown in Figure 2.4. These systems typically use separate dedicated transmitter and receiver antennae. The change in frequency (Δf), illustrated in Figure 2.4 and shown in Eq. 2.7, is a function of the speed of light (c), slant range distance (ρ), bandwidth (B), and chirp duration (T). Therefore, each return (or echo) will have a frequency difference that depends on the slant range distance. A range profile can be generated by performing a Fast Fourier Transform (FFT) on the data.

$$r_r = \frac{c}{2B} \tag{2.6}$$

$$\Delta f = \frac{2\rho B}{cT} \tag{2.7}$$

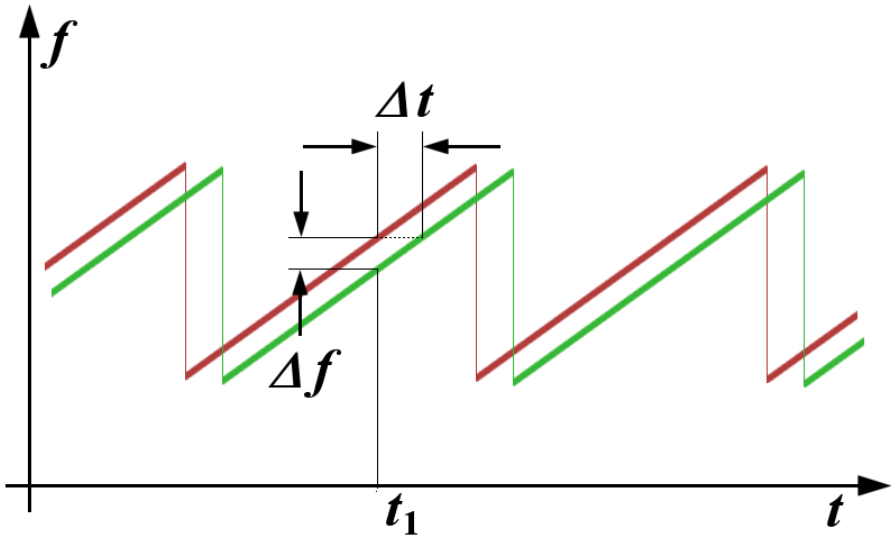

Figure 2.4 Linear FM-CW signal showing transmitted (red) and received (green) signal (modified from Wolff, 2013).

The radar components of a typical FM-CW system include transmitting (TX) antennae, receiving (RX) antennae, modulator, FM transmitter, mixer, and analog to digital converter (ADC). These components are shown in a block diagram in Figure 2.5. The system starts by generating a frequency-modulated signal which is amplified in the FM-TX stage. The modulated signal is then transmitted by the TX antenna. The transmitted signal will reflect from targets in the scan region and a component of the signal is detected with the receiving antennae. The received signal is referenced to the transmitted signal in the mixer. The analog signal is then converted to a digital form for later processing.

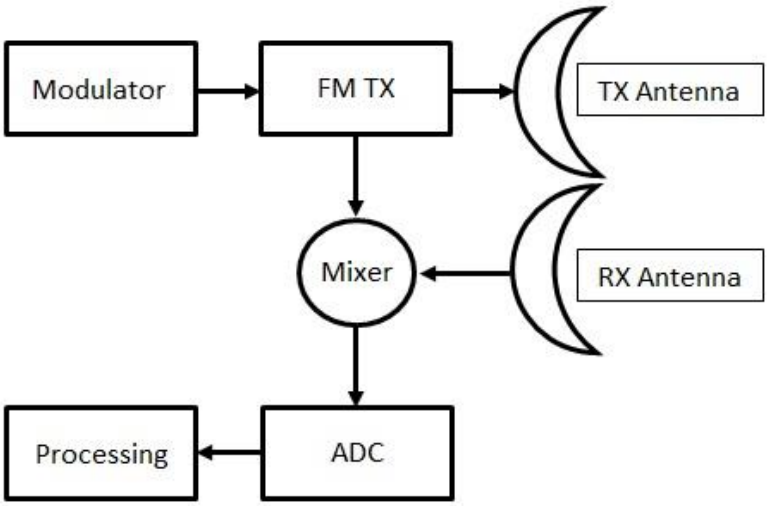

Figure 2.5 Block diagram of a FM-CW radar system

It is often desirable to quantify the power reflected back to the radar device (i.e. returned echoes or pulses), termed backscatter, as the magnitude of backscatter from a target can yield additional information about the target surface. Using several assumptions, such as the target re-radiating power back isotropically, the radar range equation (Eq. 2.8) can be derived (Richards, 2005). This equation relates the reflected power to the transmitted power (P_t), antenna power gain (G), system wavelength (λ), target radar cross section (σ), and range distance (R). While most of these parameters are mechanical or electronically static (specifically, transmitted power, antenna power gain, wavelength, and range distance), radar cross section (RCS) is not a static property that can be controlled by the user of the system. It is important to note that RCS is not the same as the physical-cross sectional area of the target in question. As a reference, Table 2.2 shows typical values of RCS for selected targets at microwave frequencies. The table shows that a large object with a curved shape can have the same RCS as a small object

with a rectangular shape, emphasizing how RCS is dependent not only on material properties but also on the target's shape.

$$P_r = \frac{P_t \times G^2 \times \lambda^2 * \sigma}{(4 \times \pi)^2 \times R^4} \text{ (W)} \tag{2.8}$$

Table 2.2 Selected values of RCS at microwave frequencies. Modified from Richards (2005)

Target	RCS (m^2)
Jumbo Jet	100
Automobile	100
Bicycle	2
Human	1
Bird	0.01

2.3 Differential Radar Interferometry

Differential radar interferometry is the process of combining two radar images of a single scene recorded at two separate times. The measured phase changes between the images are used to determine small-scale deformations occurring between the data collection times. The use of differential radar interferometry to measure deformations is illustrated in Figure 2.6 using a ground-based system for monitoring movements of an earth dam. The radar illuminates the dam face at one point in time (t_1), and collects the reflected signal. At some later time, t_2, the measurement is repeated from the same location and the reflected signal is again collected. It should be remembered that the radar collects returns from the entire surface of the dam resulting in a two-dimensional radar image from each acquisition. If a portion of the dam deforms between the data

acquisition times, the reflected signal will be shifted in phase relative to the original acquisition, as illustrated in Figure 2.6. The two radar images can be mathematically combined to create an interferogram showing regions of constant phase and regions where phase changes occurred.

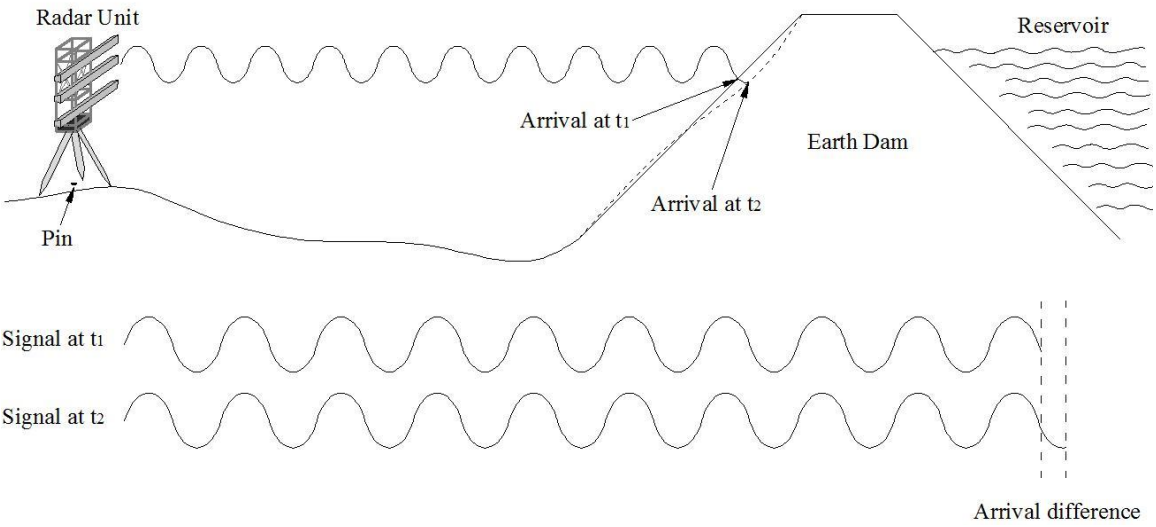

Figure 2.6 Ground-based radar acquisitions of an earth dam at two times (t_1,t_2), showing phase difference resulting from surface deformation occurring between acquisition times.

The phase difference between the two images acquired from the same location or viewpoint can be related to line-of-sight deformation. Eq. 2.9 presents the relationship between line-of-sight deformation (δ_{LOS}), wavelength (λ), and cumulative phase change (φ).

$$\partial_{LOS} = \frac{-\lambda\phi}{4\pi} \tag{2.9}$$

The processing steps involved in the development of an interferogram and the resulting deformation map are presented below.

2.4 Radar Interferometry Processing Steps

To perform radar interferometry, a specialized data processing flow must be followed to produce a reliable result. The following subsections will describe the steps to create an interferogram and ultimately a deformation map. Figure 2.7 displays the general interferometric processing workflow, starting with image coregistration and ending with the phase unwrapping stage. The following information is gleaned from Hanssen (2010), and a more detailed explanation is included in that work.

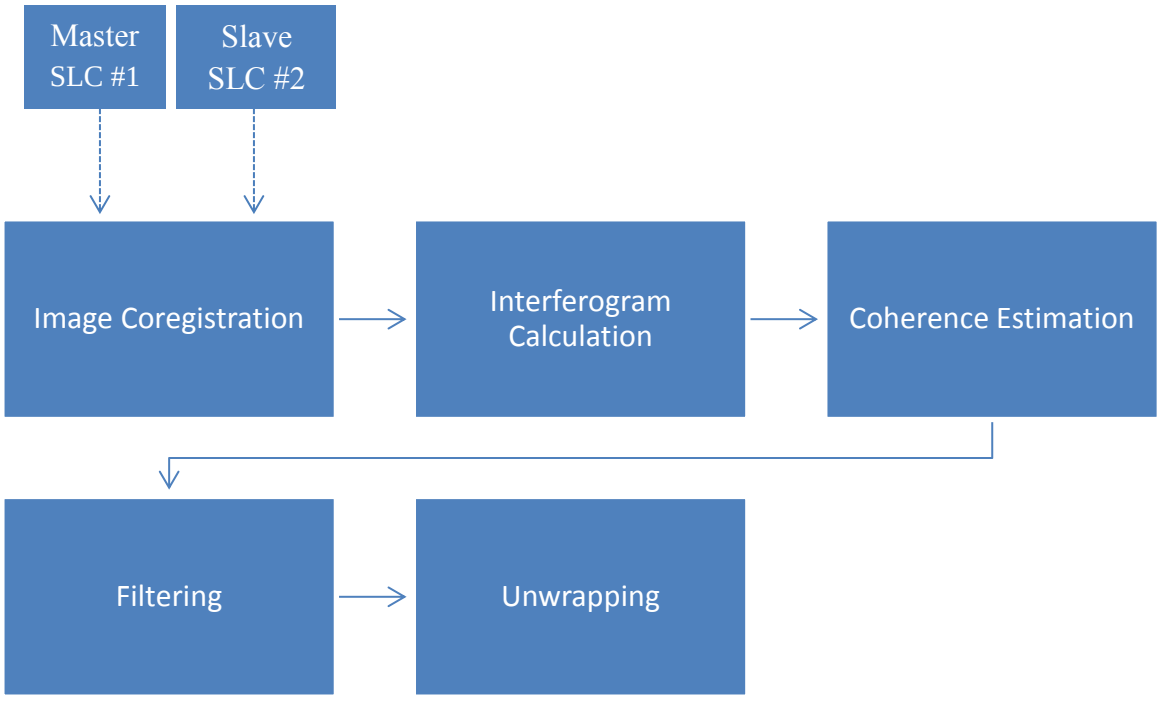

Figure 2.7 Schematic of general interferometric processing flow.

2.4.1 Image Coregistration and Resampling

Image coregistration is the process of matching a slave SLC image to a master (i.e. reference) SLC image, meaning that the slave image is translated into the same coordinates as the master image. The coregistration process starts by calculating the offset distance between known locations in each SLC. This initial process can be performed several different ways, but a common approach and one used in this study is to use a cross-intensity correlation between the two SLC images. The cross-intensity procedure is effective for cases where the observation location has not varied greatly between acquisition of the master and slave images. After offset calculation, the offset distances are input into a statistical function to determine a best fit for the interpolation required to shift the slave geometry into the master geometry. After the interpolation, the scenes (termed resampled SLC or RLSC) should be within 0.2-pixels of one another, which is important for accurate generation of interferograms.

2.4.2 Interferogram Generation

Raw interferograms are generated by using the amplitude and phase data of the radar returns for each pixel from the master SLC and RSLC. Points in the radar image can be represented using complex values (i.e. phasors) consisting of amplitude (y_1 and y_2) and phase values (ψ_1 and ψ_2), as shown in Eq. 2.10 and 2.11. The complex interferogram, ν, is created by pointwise cross multiplication of the phasors in each image (Eq. 2.12). At this stage, the interferometric phase values ($\psi_1 - \psi_2$) are wrapped, meaning the phase is constrained to the interval of [0 to 2π]. In contrast, the values used in Eq. 2.9 to calculate deformations are unwrapped or cumulative phase values. Therefore, the wrapped

interferograms much be unwrapped later in the processing chain (GAMMA Remote Sensing AG, 2007).

$$y_1 = |y_1| \times e^{j\psi_1} \tag{2.10}$$

$$y_2 = |y_2| \times e^{j\psi_2} \tag{2.11}$$

$$v = y_1 y_2^{*} = |y_1||y_2| e^{j(\Psi_1 - \Psi_2)} \tag{2.12}$$

2.4.3 Coherence Estimation

Coherence is a measure of the similarity between the radar signals from the master and slave RSLCs obtained over the same area. It indicates the accuracy of the interferometric phase (i.e. low coherence values have lower signal to noise and reduced accuracy). Ideally coherence would be calculated from ensemble averaging of a large set of measurements collected for the same pixel. However, because interferometric processing has mostly been applied from satellite platforms where many acquisitions of the same scene are not possible coherence values are typically calculated using spatial averages obtained over a limited area surrounding the pixel of interest (Hanssen, 2001). The coherence calculation implemented in the GAMMA Remote Sensing software uses Eq. 2.13. Coherence estimation is computed using a sliding window (N x N-size window) where the user selects a certain window size based on data needs. For example, a larger window will decrease uncertainty but also decrease spatial resolution because a larger area is being considered. The average cross product over the estimation window is multiplied by a factor that accounts for the local topography (GAMMA Remote Sensing

AG, 2007) and normalized by the product of the average power from each image. Coherence values are bounded between 1 (perfect coherence) and 0 (complete loss of coherence). During latter processing stages, it can be desirable to eliminate pixels in an interferogram below a certain *coherence threshold*, as these points of reduced coherence can be problematic during unwrapping because of high phase noise contamination (GAMMA Remote Sensing AG, 2010). This procedure of eliminating points below a coherence threshold is called coherence masking or validity masking in the GAMMA software, and is used during the unwrapping process for unwrapping weighting.

$$\left|\hat{y}\right| = \frac{\left|\sum_{i=1}^{N} g_{1,i}, g_{2,i}^{*} e^{-j\varphi}\right|}{\sqrt{\sum_{i=1}^{N}\left|g_{1,i}\right|^{2}\sum_{i=1}^{N}\left|g_{2,1}\right|^{2}}} \tag{2.13}$$

2.4.4 Filtering Processes

Raw (wrapped) interferograms are inherently noisy, which can cause problems later in the processing chain if not corrected. Filtering is the process of reducing the noise of the raw interferogram. To help facilitate effective unwrapping, it is advantageous to filter the interferogram to reduce spatial noise. One approach to filtering is called *multi-looking* and involves simply averaging pixels to reduce spatial noise (Goldstein, et al., 1988). For example, multi-looking of 1 to 2 means two pixels are averaged in the azimuth direction, while using only a single pixel in the range direction Additional filtering is often needed to ensure that phase residues or phase discontinuities are reduced, as phase residues cause phase unwrapping errors.

There are several techniques to filter interferograms. Only one approach will be discussed here, which is termed adaptive spectral interferogram filtering. In 1998, an adaptive filtering approach was proposed that was based on smoothing, or effectively averaging phase values over a given area in an effort to reduce residues. This smoothing process is performed on the interferogram in patches or sections using the amplitude information of the spectrum (Goldstein and Werner, 1998). In Eq. 2.14 from Goldstein and Werner (1998), Z'(u,v) is the spectrum of the filtered patch area. Therefore, if $\alpha = 0$, the multiplication factor is 1 and no filtering is applied in that window. Conversely, if the factor is increased, the filtering strength is also increased. The main idea of this filtering process is that signal (which is assumed to have strong amplitudes) is improved, while the more noisy areas (again, assumed to be weaker than the signal amplitudes) will be suppressed. This process occurs in overlapping patches. For example, consider a scene that includes a beach, hills and water. In the water areas of the scene the filter would not enhance or suppress signal because all frequency amplitudes would be similar. However, in the hills the algorithm would apply a filter since the frequency amplitudes would be different. Adaptive interferogram filtering is one example of a filtering process, which helps suppress phase discontinues or phase residues in an interferogram.

$$Z'(u,v) = Z(u,v) \times \left| Z(u,v)^{\alpha} \right| \tag{2.14}$$

2.4.5 Interferogram Unwrapping

After interferogram generation and filtering have been performed, the unwrapping stage of the interferogram processing remains. As mentioned above, unwrapping is

necessary because the cross-multiplication of complex values performed to generate the interferogram will provide phase values confined to [0 to 2π] interval. (Goldstein, et al., 1988). The absolute (i.e. cumulative) phase difference must be known at each point for deformation to be calculated. Figure 2.8(a) shows an example of an interferogram with wrapped phase (from 0 to 2π), as compared to the unwrapped or cumulative phase in Figure 2.8(b). The unwrapping is performed by adding integer numbers of 2π phase for each cycle (fringe pattern). This unwrapping procedure can be complicated by issues related to geometry and noise if phase residues are not sufficiently suppressed in the filtering stage (Hanssen, 2010). In Eq. 2.15 and 2.16 presented below, W is the wrapping operator, ΔR is the difference in range direction, and k is the integer ambiguity number. Eq. 2.15 represents the wrapped phase (φ^w), while Eq. 2.16 represents the absolute phase (φ) with an additive noise contribution (φ^N). As shown, it is impossible to solve the integer ambiguity number without some assumptions. Generally, it is either assumed (or known) that the phase gradient between adjacent pixels is less than a complete cycle (Hanssen, 2010). If this is a valid assumption (termed smoothness criterion), then phase unwrapping can be performed. The phase unwrapping is performed by integrating the phase gradients, starting from a known location (e.g. center of image). It should be noted that if one of the estimated gradients is incorrect this error propagates throughout the remaining unwrapping steps (Hanssen, 2010). The smoothness criterion means that the true phase gradient field must equal zero when forming the closed loop (Bamler and Hartl, 1998). However, this is complicated because the gradient of the true phase is unknown, so this value must be estimated from the wrapped phase. Sometimes, noise errors will disrupt the process and cause global errors, thus it is important to use

coherence masking to help eliminate noise errors. For digital images, the smoothness criterion is evaluated by looking at a 2 by 2-pixel window, as shown in Eq. 2.17 (Hanssen, 2010). The value of the r term (residue) can be 0, +1 cycle, or -1 cycle. The phase residues occur due to either inherent phase noise or undersampling (i.e. not averaging enough pixels), which will lead to global unwrapping errors (and thus incorrect deformation values) if not resolved. These residues can be connected to one another, thereby unloading (i.e. resolving the discontinuity) the total interferogram (i.e. branch cut). This is just one of several approaches that can be used to unwrap an interferogram.

$$\varphi^{w} = W\{\varphi\} = \mathrm{mod}\{\varphi + \pi, 2\pi\} - \pi \tag{2.15}$$

$$\varphi = \frac{-4\pi\Delta R}{\lambda} + \varphi_N = 2\pi k + \varphi_N \tag{2.16}$$

$$r = W\left\{\left(\varphi^{W}_{i+1,j} - \varphi^{W}_{i,j}\right)\right\} + W\left\{\left(\varphi^{W}_{i+1,j\_1} - \varphi^{W}_{i+1,j}\right)\right\} + W\left\{\left(\varphi^{W}_{i,j+1} - \varphi^{w}_{i+1,j+1}\right)\right\} + \left\{\left(\left(\varphi^{W}_{i+j} - \varphi^{W}_{i,j+1}\right)\right)\right\} \tag{2.17}$$

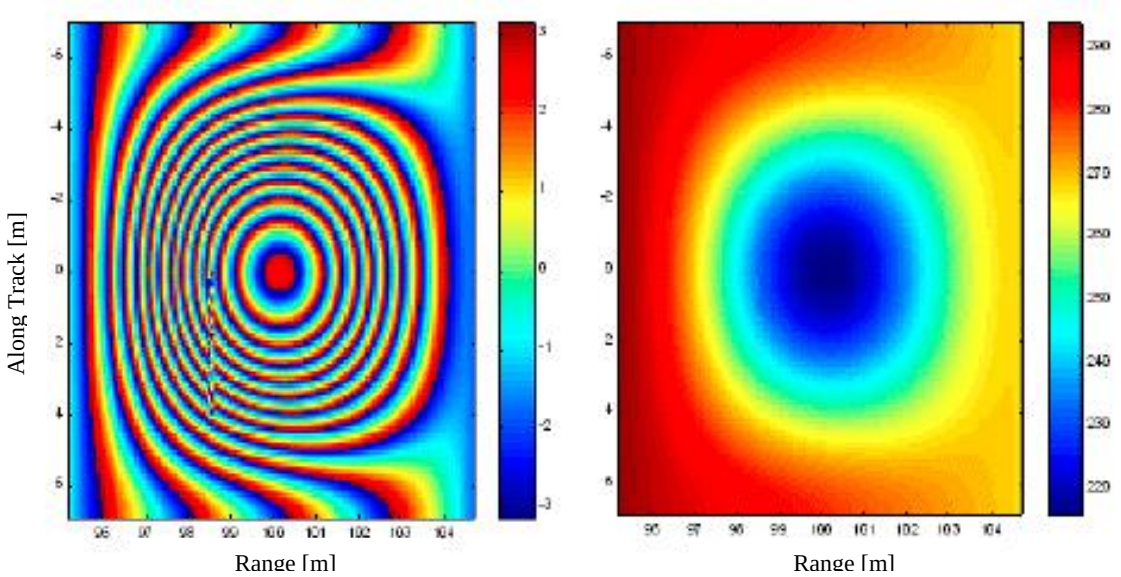

Figure 2.8 Example of an interferogram presented in terms of (a) wrapped phase and (b) unwrapped phase (Richards, 2005).

2.4.6 Removing Atmospheric Effects

Deformation measurements determined from interferometric radar require measuring the unwrapped phase change caused by surficial movements between data acquisitions. Ideally, to determine accurate deformation values from Eq. 2.9, the unwrapped phase change should only be due to surficial movements. However, in practice other unavoidable contributions to the measured phase change complicate the ability to extract deformation information. In addition to phase change due to deformation, phase changes measured from a ground-based system may also occur due to changes in the reflectivity properties of the pixel ($\Delta\varphi_{pixel}$), phase noise in the system ($\Delta\varphi_{noise}$), and phase changes due to propagation velocity changes from different atmospheric (temperature and humidity) conditions ($\Delta\varphi_{atm}$), as shown in Eq. 2.18.

$$\Delta\varphi = \Delta\varphi_{disp} + \Delta\varphi_{atm} + \Delta\varphi_{pixel} + \Delta\varphi_{noise} \tag{2.18}$$

Satellite-based measurements have additional phase contributions from topography, due to a non-zero baseline, and earth curvature. Fortunately, phase contributions due to changes in reflectivity and system noise are relatively small. However, phase changes due to atmospheric effects can be significant and must be removed. The phase changes due to atmospheric effects arise from different amounts of moisture (i.e. water vapor) in the atmosphere during acquisitions of data. For example, if a greater amount of moisture is present in the atmosphere during a repeat-pass scan, the radar waves will take a longer time to pass through the water vapor, which will yield an apparent shift in the phase data. This apparent phase shift can be mistakenly considered deformation, so vigilance must be maintained to avoid this mistake. A hallmark of atmospheric contamination is a so-called "atmospheric ramp." Figure 2.9 shows the effects of changing moisture conditions from data collected from a satellite-based platform as well as a ground-based radar. In the figure, distinct fringes are evident which are characteristic of atmospheric effects, as noted in Li et al., (2007). Once the atmospheric-contaminated interferogram is unwrapped, atmospheric effects can be removed using a quadratic function that is fit to the existing contaminated unwrapped file, and then subtracted from the interferogram yielding a contamination-free unwrapped interferogram (GAMMA Remote Sensing AG, 2008).

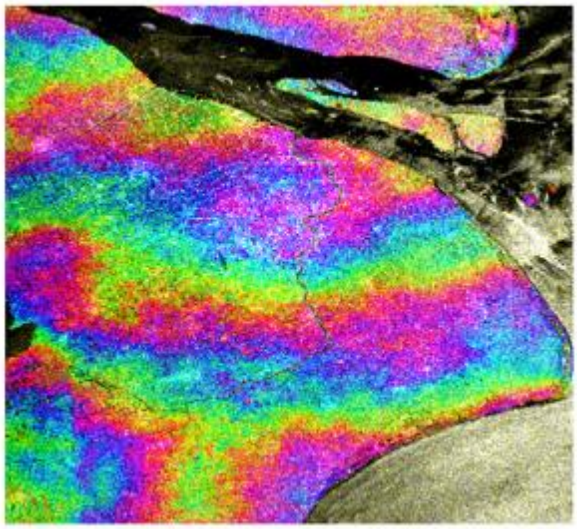

(a)

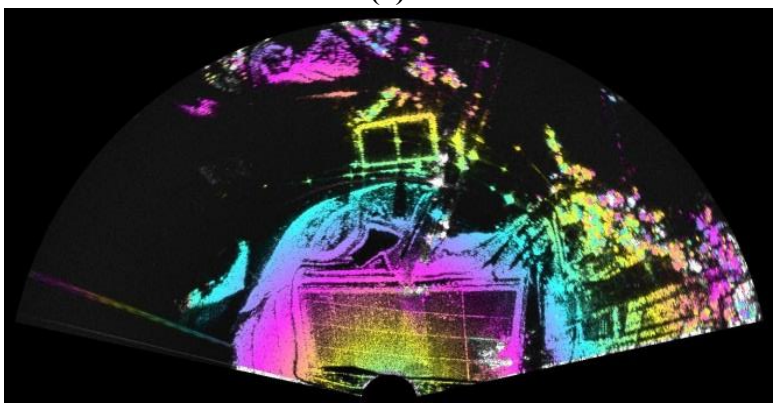

(b)

Figure 2.9 Example of atmospheric ramps in interferogram data using a (a) satellite-based radar platform, acquired over one-day (Li, et al., 2007) and (b) ground-based radar device, acquired over several hours.

2.5 Summary

This chapter provided a general overview of radar and the fundamentals of differential interferometry for deformation measurements; subjects that are not generally familiar to a civil engineering audience. This was followed by a detailed presentation of the interferometric processing chain that was utilized in the work. Important concepts relevant to this research were covered, including: (1) coherence estimation and masking

and (2) atmospheric phase contamination and removal. The specific processing parameters and methods applied in the field are included in separate chapters covering each field testing program.

Chapter 3: Ground-Based Interferometric Radar

3.1 Introduction

Ground-based interferometric radar is an emerging technology with only a few commercially available platforms. This chapter begins with a brief overview of the three commercial GBIR radar systems that are currently available. Next, the GBIR system used in this study is described. The chapter concludes with a review of past relevant studies using GBIR radar and a description of how the topics covered in this thesis contribute to the body of knowledge in this field.

3.2 Ground-based Interferometric Radar Systems

3.2.1 Ground Probe

GroundProbe was developed in 2001 as an offshoot from research performed at the University of Queensland in Australia. The GroundProbe device is a real-aperture radar system that utilizes a dish antenna with diameters ranging from 0.9 m to 1.8 m. It uses a pencil-beam radar that is scanned in two-dimensions across the site of interest. The GroundProbe system has been used primarily to monitor rockwall for mining applications (GroundProbe, 2012). An example of one of the GroundProbe systems is shown in Figure 3.1. The system can rotate 270 degrees in the horizontal direction and can scan 122 degrees in the vertical direction. The company reports centimeter-scale deformation accuracy with the radar (Table 3.2). GroundProbe has recently developed a truck mounted radar dish system (GroundProbe, 2012). The GroundProbe system is

designed to be setup and operate continuously from a single location. It is not designed to be removed and repositioned over the same location for repeat-setup measurements.

Figure 3.1 GroundProbe SSR device deployed at open pit mine site (GroundProbe, 2012)

3.2.2 IBIS-L

Another ground-based radar system, termed IBIS, has been developed over the past decade. The original radar system on which it is based was developed by an Italian research team. The IBIS-L system (a specific model in the IBIS line) is a synthetic aperture system, meaning it synthesizes a large-aperture antenna by translating a horn antenna along a rail, as shown in Figure 3.2. The basic radar system is discussed in Pieraccini, et al. (2000), and since that time five other types of radar devices have been specifically developed for minewall stability and structural monitoring (IDS Corporation, 2013). The IBIS-L system is capable of acquiring data at intervals as short as 5 minutes (due to the time required to translate the antennae over the 2m rail and reset). The company reports 1/10 mm deformation accuracy and the ability to scan at ranges up to 4

km (Table 3.2). This radar system is also capable of running autonomously without the need for an operator in the field (Olson Instruments, Inc, 2012).

Figure 3.2 Photo of IBIS-L system applied to monitoring of a concrete dam (Olson Instruments, 2013)

3.2.3 GAMMA Remote Sensing

In 2008, GAMMA Remote Sensing, Inc. based in Switzerland developed a prototype ground based radar system, as shown in Figure 3.3 (Werner, et al., 2008). The system developed by GAMMA Remote Sensing is a real aperture, tripod-mounted system utilizing a narrow fan-beam antennae pattern which is rotated to scan the region of interest. This radar system consists of one transmitting antennae and two receiving antennae, as shown in Figure 3.3. The original system, termed the GPRI-I, operated on the Ku-frequency band and could scan 90 degrees in the horizontal plane in about 20 minutes (Table 3.2). The system operated over range distances of 0.1 km to 4 km and the developers reported 2-mm deformation precision in the line-of-sight direction. (Werner, et al., 2008). A second generation of this device with improved capabilities was

developed by GAMMA Remote Sensing and is the primary system used in this study, as discussed below.

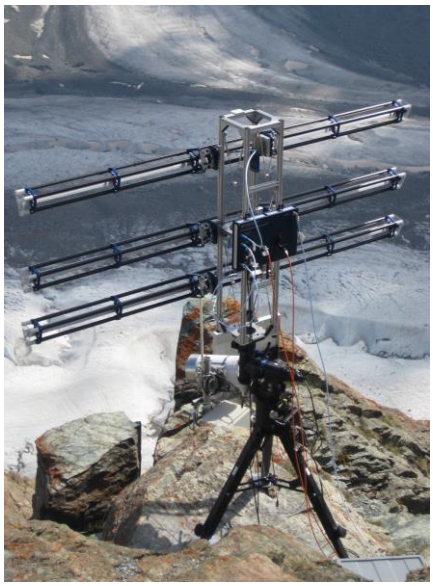

Figure 3.3 GAMMA Remote Sensing ground based system, GPRI-I (Werner, et al., 2009)

3.3 GBIR System at the University of Missouri

The GBIR system in operation at the University of Missouri (MU) consists of the second-generation system (GPRI-II) developed by GAMMA Remote Sensing with additional custom-built components to enhance its capabilities. The base device, shown in Figure 3.4, consists of three antennae (1 transmitting and 2 receiving), a radio frequency controller (RF) box, motor, tribrach, tripod, and field computer to operate the device. The antennae are slotted waveguide members, each approximately two meters in length. The RF box creates the waveforms used in the radar image acquisition. The motor included with the radar apparatus is a precise stepping motor, which allows for rapid and continuous acquisition of imagery (more rapid data acquisition than possible with the first generation device). The tribrach is used to level the radar system, which is required for

accurate measurements. The tribrach also includes a laser plummet that allows for precision set-ups over a monument. The tripod can be set-up over a survey monument with an accuracy of approximately 1/2 mm. It should be noted that as long as the height of the radar above the monument is constant, azimuth shifts from repeat measurements can be easily accounted for during the coregistration process described in Section 2.4. The entire upper structure of the GBIR systems typically is mounted on the tripod, but can also be fitted to a more permanent structure.

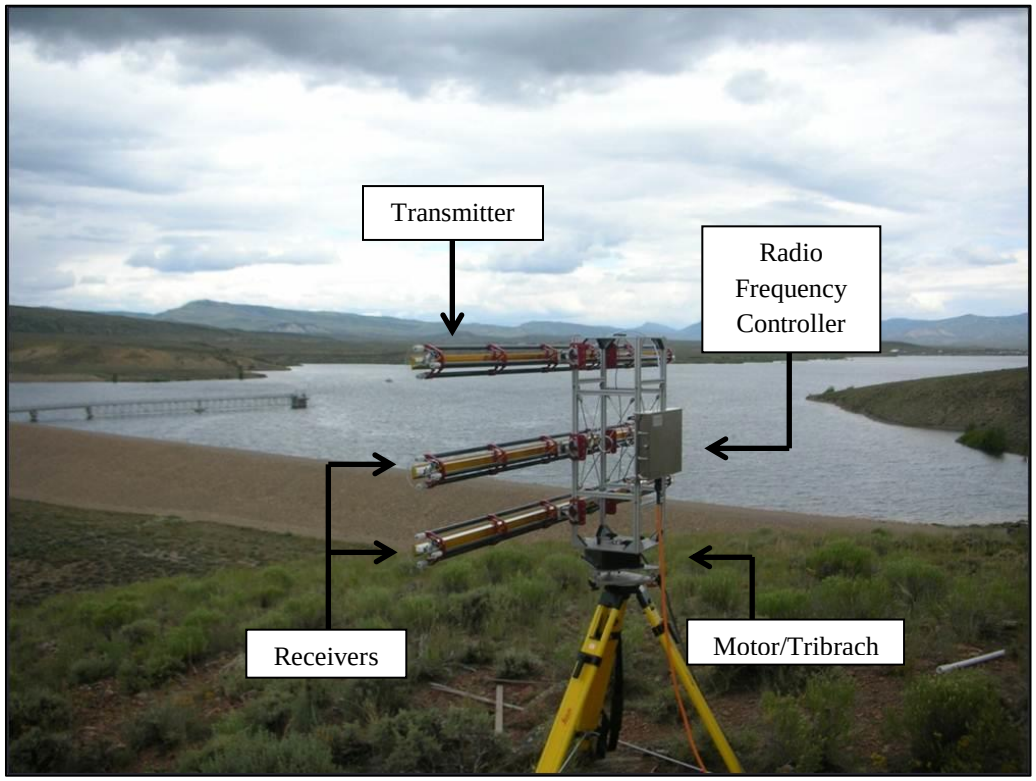

Figure 3.4 Photograph of the Ku-band system with major system components identified overlooking a rockfill dam in Colorado.

In addition to the base system, which operates in the Ku-frequency band, the GBIR system at MU has a custom-made controller and antennae which allow the system to operate at the lower frequency (and longer wavelength) C-band. Systems with a lower

central frequency (or longer wavelength) are less affected by atmospheric path delays and decorrelation due to vegetation (Richards, 2009). However, longer wavelengths are less sensitive to deformation, thus there is a trade-off between resolution and signal coherence. The C-band system developed for the MU device also has the ability to acquire fully polarimetric data (i.e. HH, HV, VH, VV modes), as opposed to the single polarization data acquired with the Ku-band system. Acquiring signal with varying polarizations allows the user to "optimize" the data for the best signal return. In this study, only single polarity acquisitions are presented.

Table 3.1 presents operational and performance specifications for the Ku and C-band GBIR systems at MU. The main differences between these systems, other than operating frequency, are the lower azimuthal resolution of the C-band system due to a wider beam pattern and the polarimetric capability of the C-band system, which is not available on the Ku-band system. The performance specifications of the various GBIR described above systems are compared in Table 3.2.

Table 3.1 Performance Specifications for the Ku-Band and C-Band GBIR Systems (after GAMMA Remote Sensing AG, 2001)

Type	Ku-Band	C-Band
Radar Type	FM-CW	FM-CW
Frequency	17.1-17.3 GHz	5.3-5.5 GHz
Chirp Duration	0.25 - 8 ms	0.25 - 8 ms
Acquisition Mode	Single Polarization 2m Antennae (VV)	Fully Polarization 2m Antennae (HH, HV, VH, VV)
	Single Polarization Horn Antennae (HH, HV, VH, VV)	Single Polarization Horn Antennae (HH, HV, VH, VV)
Transmit Power	100 mW (+20dBm)	100 mW (+20dBm)
Power Consumption	65 W, 110-220 V(AC) or 24 V(DC)	65 W, 110-220 V(AC) or 24 V(DC)
Chirp Bandwidth	200 MHz	200 MHz
Azimuth Scan Time	20 seconds for 180 degree sweep	20 seconds for 180 degree sweep
2m Antennae Pattern	38 degree, 3dB Elevation Beamwidth	38 degree, 3dB Elevation Beamwidth
	0.5 degree, 3dB Azimuth Beamwidth	1.5 degree, 3dB Azimuth Beamwidth
Antennae Polarization	Single Polarization (V)	Dual Polarization (H,V)
Radar Operation Range	50m -10km	50m -10km
Azimuth Resolution	~0.70m at 100m Range Distance	~2.62m at 100m Range Distance
Range Resolution	1 m with Kaiser Weighting	1 m with Kaiser Weighting
	0.75 m without Kaiser Weighting	0.75 m without Kaiser Weighting

Table 3.2 Performance specifications for radar devices discussed in Chapter 3

System	Studies	Radar Band	Resolution		Scanning Rate	Displacement accuracy	Max range (km)	Operational Mode
			Range (m)	Azimuth (m)				
GroundProbe SSR	Mine Stability	Not available	Not available		10°/second	0.3m x 0.3m @ 30 m (range)	3.5	Truck-mounted
IBIS-L	Slope Stability, Dam Deformation	Ku	0.5*	4.5 (rad)	0.021 m/second*	0.1 mm	4	Rail-based
GAMMA GPRI-I	Glaciers, Landslide	Ku	0.75	3.5 @ 500m	0.075°/second	< 2mm	4	Tripod-based
MU GBIR	Current	Ku	0.75	3.5 @ 500m	20°/second	0.5 mm	10	Tripod-based

*Time required to translate along 2m rail and reset

3.4 Literature Review of Past Applications of GBIR

Ground-based interferometric radar is an emerging technology that has not been widely adopted for engineering applications. A review of the literature on GBIR found fewer than 35 publications on the application of GBIR, all of which have been published in the last fifteen years. The majority of the past applications of GBIR have been for slope and mine stability problems; however, GBIR has also been used for other scientific and engineering applications. Presented below are brief summaries of several applications of GBIR reported in the literature. This section concludes with a brief discussion of how this study contributes to the body of knowledge on GBIR for civil engineering applications.

Glacier Study

One application of ground-based interferometric radar has been for measuring glacial movements. In 2007, engineers and scientists used the first generation GAMMA Remote Sensing, Inc. ground-based system, operating on Ku-band frequencies, to monitor movements of the Rhone glacier in Switzerland (Werner, et al., 2009). Four interferograms were generated from fourteen radar scans measured over a time span of 80 minutes using a continuous set-up of the equipment (i.e. the equipment remained in place throughout the study). The displacement map of the glacier created from the interferograms clearly showed deformation of the glacial mass over the span of 80 minutes, which was in good agreement with historical data from the site acquired using aerial photogrammetry and Digital Elevation Models (DEM).

More recently, the GAMMA radar device was deployed to measure a problematic rock glacier in Switzerland known to move between 0.1 and 1.0 m/year due to seasonal variations. The device was deployed in a repeat set-up manner with measurements first performed in August 2009 and a second set of measurements in March 2010 to measure movements of the rock glacier over that time span. Each observation was performed over the span of one day (acquiring data every 15 minutes) from a standoff distance of 1 km. In that study, ground control points from a DEM were incorporated with phase data to constrain the unwrapping problem. After processing data from each observation date, the results showed an increase of almost 10 m in the surface topography due to seasonal changes in the surface (Strozzi, et al., 2012).

Another study of glacier movements was performed in late 2004 using a ground-based SAR system to monitor the retreating Belvedere glacier in the Italian Alps (Luzi, et al., 2007). Much like the IBIS system described in Section 3.2.2, this system consisted of a rail-mounted antenna which translated along the rail during each acquisition. This system operated using C-band frequencies. The device remained setup at the same location for approximately one week while acquiring data every 36 minutes. Interferograms from a two-day span were used to create a displacement model showing deformation values of approximately 30 mm/hour, which were consistent with previous measurements acquired using air photos. In addition to displacement data, coherence over one day was also measured in this study and was shown to remain high for both moving and stationary areas.

Slope and Mine Stability Studies

The most common application of GBIR reported in the literature has been for slope and mine wall monitoring. Much of the work on slope stability monitoring has been performed by researchers from the University of Florence in Italy (Tarchi, et al., 2000, Casagli, et al., 2003, Pieraccini, et al., 2003, Corsini, et al., 2006, Luzi, et al., 2006, Noferini, et al., 2006, Pieraccini, et al., 2006, Lingua, et al., 2008, Teza, et al., 2008, Bozzano, et al., 2010, Casagli, et al., 2010, Del Ventisette, et al., 2011). One of the first slope studies using GBIR (Pieracini et al., 2003) utilized the same rail-based system previously described to monitor an unstable slope near Valdarno, Italy, which was first triggered in December 1998. The ground-based radar survey began in February 12, 2001 and ended on March 19, 2001, a time of intense rainfall during which the slope was visually observed to move. In this case, radar images were collected every 20 minutes during the continous observation period. Three areas of the slope were selected for discrete displacement study, one at the head of the scarp, and two points lower on the scarp). The point located at the head of the scarp moved throughout the study and was evenutually correlated to temperature changes. Movement on order the of 0.5 cm/hr was observed on the scarp.

Another slope stabily case involved monitoring a landslide in Tessina, Italy, where the IBIS and GAMMA systems were deployed. The landslide in Tessina was a 3-km long and 500-m wide rotational slide (Luzi, et al., 2006). The IBIS system operated using C-band frequencies and the GAMMA device operated using Ku-band frequencies. Each of the devices acquired data at approximately the same rate. The Italian device aquired data over the span of almost 5 days, while the GAMMA system aquired data over

the span of 3 days. Displacement measurements were presented for both systems but since both acquired data over different timespans, direct comparions were not possible. However, the displacement rates were similar.

Interferometric radar has also been used extensively to monitor mine wall stability, which can pose hazards to personnel as well as infrastructure (McHugh, et al., 2006, Mecatti, et al., 2010, and GroundProbe, 2012). These areas often present risks because large wall cuts can become unstable and must be monitored to ensure safe working conditions. Two ground-based radar systems have been used to monitor mine walls, the IBIS system described in Section 3.2.2 and the GroundProbe truck-mounted dish system described in Section 3.2.1. In one case, the IBIS system was deployed to a mining site in Firenze, Italy, where it was positioned approximately 800 m away from the slope. Images were collected continuously every two hours over the span of 40 days using Ku-band frequencies. No displacements were observed. However, the authors were able to demonstrate that sub-mm sensitivities could be detected using local corner reflectors (Mecatti et al., 2010). The GroundProbe system has been successfully used in several field sites to date. Notable results from two field sites have been published: Phelps Dodge Sierrita Mine near Tucson, AZ and Leinster Nickel Harmony in Australia. In both of those cases, the GroundProbe device provided employees with several hours of advance warning before portions of the slope became unstable (Noon and Harries, 2007).

Bridge & Concrete Dam Studies

Another important application of ground-based radars has been monitoring deformation of man-made structures, such as bridges and concrete dams (Tarchi et al.,

1999, Pieraccini et. al, 2000, Tarchi, et al., 2000, and Pieraccini, et al., 2004, Alba, et al., 2008). One of the first published studies of GBIR concerned monitoring millimeter-scale bridge deformations (Pieraccini, et al., 2000). In this case, a precursor to the current IBIS system was implemented using a Ku-band frequency system under a bridge to measure deformations caused by four sets of static loading cases. Metal reflectors were positioned on a bridge deck to provide strong radar reflections, and optical sensors were used to provide ground truth measurements. The optical targets were set on a bridge pillar. The bridge in this test was progressively loaded throughout the experiment while deformations were monitored. The authors concluded that there was good agreement between the optical and radar measurements (Pieraccini, et al., 2000).

Monitoring of the deformations of large dams is an ideal potential application of GBIR that has not been studied extensively. Reviews of the literature found only five publications on GBIR applied to dam movements, as of May 2013 (Tarchi, et al., 1999, Alba, et al., 2008, Luzi, et al., 2010, Jenkins, et al., 2012, Olson Instruments, 2013). One study reported on the use of GBIR to monitor a concrete dam in central Italy using the IBIS rail-based system (Olson Instruments, 2013). The studied dam is a double curved concrete structure with a height of 100 m and approximately 400 m in length. In addition to the ground-based radar system, a series of pendulums and extensometers were used to provide ground truth measurements. Previous historic dam records showed that between May to October the dam moved approximately 3-5 cm. Radar data were acquired during seven periodic observations from June to September at two weeks intervals. The authors showed that displacement results from the radar device were in good agreement with ground truth data (Tarchi et al, 1999).

Table 3.3 Summary of selected previous GBIR studies of note presented in this chapter

Study Type	Study Authors	Instrument	Radar Band	Equipment Setup	Observation Timeframe	Scale of Movements
Glacier	Stozzi et al., (2012)	GAMMA	Ku-band	Repeat-pass	15-minutes scans, 7 months	40 cm/day
Mine Wall	McHugh et al.	GroundProbe	Ku-Band*	Continuous	15 minutes	0.2 mm
Glacier	Luzi et al., (2007)	IBIS	C-band	Continuous	36-minutes scans, 14 days	3 cm/hour
Slope Stability	Pieracini et al., (2003)	IBIS	C-band	Continuous	20-minutes scans, 35 days	0.5 cm/hour
Mine Wall	Mecatti et al., (2010)	IBIS	Ku-band	Continuous	2 hour scans, 40-days	0 cm/hour (0.53 mm)**
Bridge	Pieracini et al., (2000)	IBIS	Ku-band	Continuous	Not specified	0.1 cm
Concrete Dam	Tarchi et al., (1999)	IBIS	C-band	Continuous	Every 2 weeks (7 total scans)	1 cm

*Frequency not referenced in literature, likely value is given

**No movement detected on mine wall, movement is parenthesis is manually displaced corner reflector

3.5 Motivation for Proposed Study

Ground-based radar interferometry is a relatively new technology that shows great promise for measuring small-scale deformations of geologic sites and engineering structures. A review of the literature shows that GBIR has been applied to a wide range of problems. Table 3.3 summarizes a selection of relevant studies using GBIR. It can be seen from this table and a review of the literature that most of these studies have been performed using continuous-setup data collection procedures, meaning the device is sequestered for the duration of the study, and later removed after data acquisition is completed. In addition, most of the studies in the literature were performed using short time intervals between measurements (typically tens of minutes apart).

One application that is not well represented in the literature and has not been studied extensively is the use of GBIR for periodic monitoring of engineering sites. This type of application requires repeat set-up of the equipment (equipment is removed and redeployed for each measurement) and involves longer time intervals between measurements (weeks to months). The degradation in coherence over these longer time spans and the possibility of significant atmospheric effects are important research topics for this application.

This research is contributing to the literature in this field by studying the application of GBIR for long-interval, periodic monitoring of civil engineering sites. This project will also contribute results from GBIR measurements at civil engineering sites that are not represented in the literature; namely, natural rock slopes, earth dam embankments and new geosynthetic landfill liners. These studies are presented in Chapters 4 through 6.

Chapter 4: Monitoring of a Rock Slope

4.1 Introduction

This chapter presents results from a field study using GBIR on an active rock slope near Glenwood Springs, Colorado. The measurements were part of a pilot study initiated by the Colorado Department of Transportation (CDOT) to evaluate the potential for GBIR to detect and monitor minute rock movements for use in early warning or long-term monitoring applications. As noted in the literature review in Chapter 3, the use of GBIR for rock slope or rock fall monitoring is not well documented in the current literature. This field trial presented an opportunity to study the capabilities and limitations of GBIR for this application. The specific objectives of this study were to: (1) detect and measure rock mass movements using interferometric measurements performed over time spans of two to four weeks; (2) quantify spatial coherence of the rock slope and vegetated areas over short (days) and intermediate terms (weeks), and (3) evaluate data processing techniques to improve the quality of the results. Descriptions of the field site, data collection procedures and processing methods are presented below. Results from the displacement and coherence measurements are presented and discussed.

4.2 Description of Field Site and Experimental Procedures

4.2.1 Field Site Description and Data Collection Procedures

Glenwood Canyon is located in western Colorado, approximately 150 miles west of Denver (Figure 4.1). The steep canyon walls rise to over 1000 feet above the canyon floor. Interstate 70 passes through Glenwood Canyon, and has been damaged and closed

on several occasions due to rock fall events from the canyon walls (Leib, 2010). An expanded view of the region is shown in Figure 4.2 and a photograph of the specific site of interest where recent rock fall has occurred is shown in Figure 4.3. This site consists of a steep rock face, talus slope, and vegetated areas. The CDOT conducted a field study at this site with promising technologies for rockfall monitoring. Ground-based interferometric radar was one of several methods (including LiDAR and high-resolution optical imagery) evaluated as part of the CDOT study. The only viable location to set up the GBIR was from atop a cliff located approximately 500 m across from the rock slope. The measurement location was accessed using a helicopter to transport equipment and personnel to the site. Specific coordinates are located in the Appendix. Due to the precarious nature of this location, the radar was positioned on a rigid mast bolted into rock instead of the typical tripod system. The mast was secured using four rock bolts that were epoxied into holes drilled in the rock (Figure 4.4). While the mast did not remain in-place throughout the measurement campaign, the rock bolts were fitted with nuts and washers that were secured to provide repeatable positioning of the radar for each return measurement.

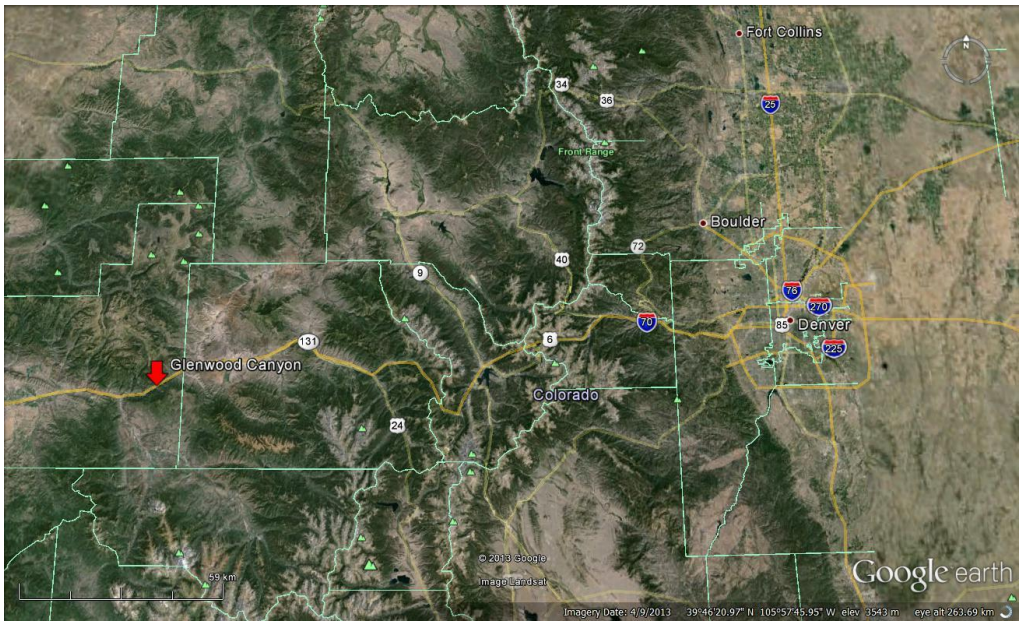

Figure 4.1 Google Earth image of the Glenwood Canyon site in relation to Denver, CO.

Figure 4.2 Expanded view of the Google Earth image of Glenwood Canyon showing area of interest (white circle) and radar measurement location (red arrow).

Figure 4.3 Rock slope of interest in Glenwood Canyon, CO.

Figure 4.4 Panoramic view from radar location. Red circle indicates primary site of interest.

The GBIR system used in this study (described in Section 3.3) is not designed to be left unmanned at a site for an extended period of time. Therefore, the measurements

were performed by selecting three dates, each about two weeks apart, when the GBIR could be transported to the site and data could be collected for several hours. (Over the same time period GBIR measurements were performed using a continuous setup of the IBIS-L radar operated by Olson Engineering, Inc.) The measurement dates and number of images acquired on each day are displayed in Table 4.1. The images were acquired at approximately five minute intervals on each date. These scans were coordinated with the other ground-based radar system (IBIS-L) to avoid signal interference between the two systems.

Table 4.1 **Date of data acquisitions and number of images acquired during surveys campaigns in Glenwood Canyon, CO**

Date	No. of Images Acquired
May 15, 2012	32
May 30, 2012	31
June 12, 2012	30

4.2.2 Data Processing Procedures

The data collected during the three measurement dates were organized into separate folders for each acquisition campaign (i.e. May 15, May 30, and June 12 folders). Before resampling of the radar images was performed, the raw files were focused into SLCs, using the "gpri2_proc_all" command in the GAMMA software package. Each raw file was decimated by a factor of 10 to reduce excessive noise while still providing an appropriate coregistration fit. Next, every image in each of the datasets was coregistered to the first SLC file in the May 15 directory (specifically file number 20120515_001) using the coregistration commands discussed in Chapter 2. This ensured that all images were compared using the same frame of reference.

Processing of interferometric data often requires trial and error to achieve reliable results. Details of the processing parameters used to achieve the final unwrapped imagery are summarized in Table 4.2. However, these parameters were not the initial processing parameters that were used. Initially, a 16-pixel filter window was selected for use, but was abandoned after many of the interferograms were not successfully unwrapped. After the 16-pixel window was abandoned, a larger 32-pixel window was selected to smooth the phase and facilitate proper unwrapping. The unwrapping errors encountered using the 16-pixel window were likely due to shadowed areas and other areas of low coherence resulting in phase discontinuities which caused problems for the unwrapping algorithm. These phase discontinuities were overcome with additional spatial smoothing from the larger filtering window. Once successful unwrapping was achieved, interferograms were stacked, using the "stacking" command in the GAMMA software package. Stacking is the process of time-weighted averaging of multiple interferograms to produce a single stacked interferogram with improved signal to noise values and phase estimation. Details of the data stacking procedures used to process the data for this site are summarized in Table 4.3. As shown in Table 4.3, not every unwrapped interferogram was utilized in the stacking procedure because in some cases portions of the unwrapped interferograms were not successfully unwrapped, even with the larger smoothing filter. These interferograms were identified manually and excluded from the stack. Additional processing issues are discussed in Section 4.3.3 following presentation of the results.

Table 4.2 Details of Glenwood Canyon processing for each measurement interval

Dataset	Interferogram Looks	Filter Used/ Window Size	Validity Mask Used (Coherence/Intensity Threshold)	Filter Coefficient Used	Atmospheric Phase Model Used
5/15/2012 - 05/30/2012	1 & 2	Spectral/ 32	0.25/0.2*	0.4	0: a0 + a1*x + a2*y + a3*x*y + a4*x^2 + a5*y^2
5/30/2012 - 06/12/2012	1 & 2	Spectral/ 32	0.25/0.2*	0.4	0: a0 + a1*x + a2*y + a3*x*y + a4*x^2 + a5*y^2
5/15/2012 - 06/12/2012	1 & 2	Spectral/ 32	0.25/0.2*	0.4	0: a0 + a1*x + a2*y + a3*x*y + a4*x^2 + a5*y^2

*No coherence mask used in coherence study

Table 4.3 Number of interferograms generated and stacked at Glenwood Canyon

Dataset Time Span	Interferograms Generated	Interferograms Stacked
5/15/2012 to 5/15/2012	31	31
5/15/2012 to 05/30/2012	31	22
5/30/2012 to 06/12/2012	28	12
5/15/2012 to 06/12/2012	30	23

4.3 Results and Discussion of Displacement Measurements

4.3.1 Results of Displacement Measurements

The primary objective of this study was to detect and measure rock mass movements using repeat-setup GBIR measurements. The three data acquisition dates allowed for displacement maps of the rock slope to be developed over three different intervals. For each interval, displacement maps created from the stacked interferograms are presented using, (1) a coarse displacement scale (1 inch per color cycle) and (2) a finer scale (¼ inch per color cycle). These displacement maps are presented in two ways: (1) superimposed on a two-dimensional aerial photo of the entire region sampled with the radar, and (2) overlain on a 2-ft digital elevation model (DEM) of the specific cliff face of interest in this study. The displacement maps covering the May 15 to May 30, 2012

timespan are shown in Figures 4.5 and 4.6. The displacement imagery for the next time span from May 30 to June 12, 2012, are shown in Figures 4.7 and 4.8. The displacement imagery spanning over the entire six week time span (May 15-June 12, 2012) are shown in Figures 4.9 and 4.10. Atmospheric phase contributions were removed from the unwrapped phase plots using the function shown in Table 4.2. To illustrate the effects of atmospheric phase, unwrapped interferograms with and without the atmospheric phase contribution are shown in Figure 4.11.

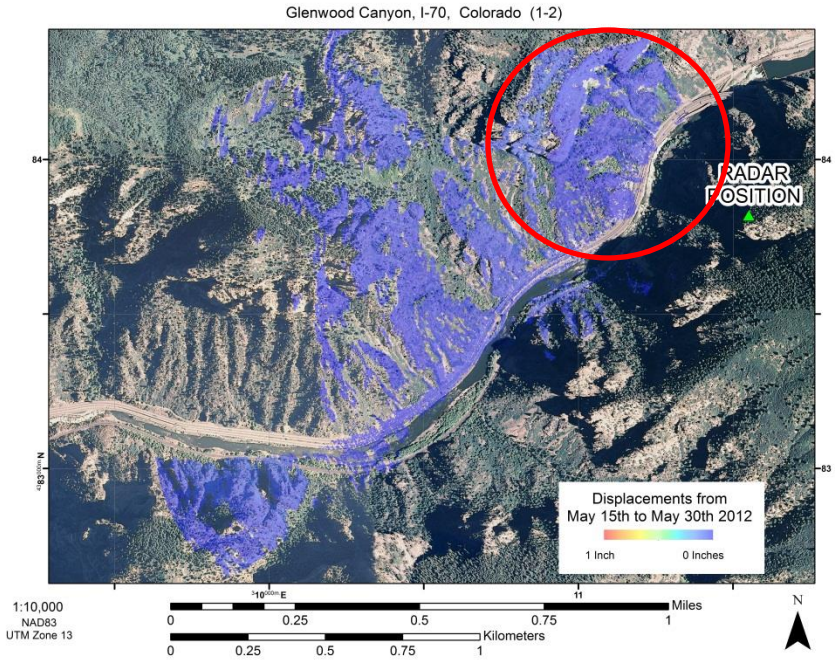

(a)

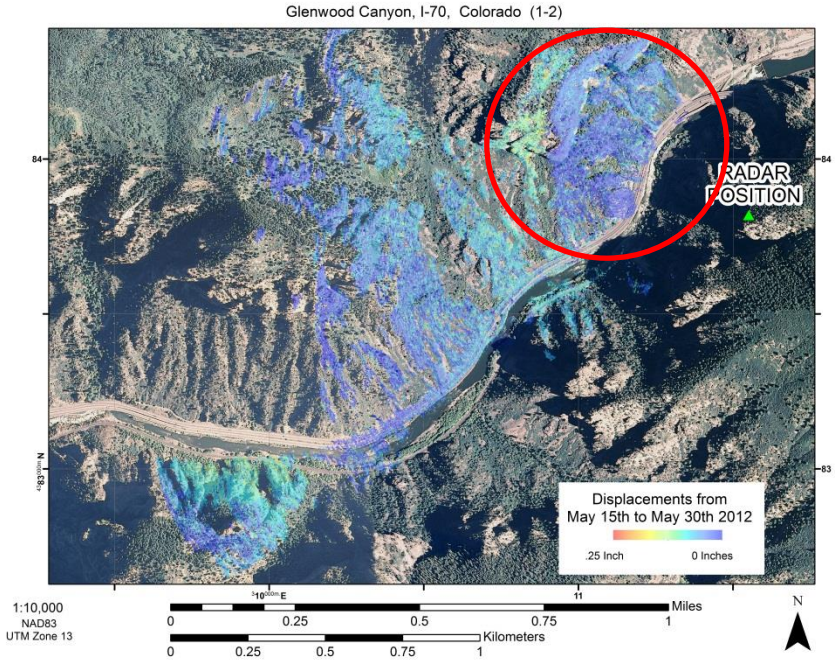

(b)

Figure 4.5 Aerial photo with superimposed line-of-sight deformation map from May 15, 2012 to May 30, 2012 using (a) 1-inch/cycle scale and (b) ¼-inch/cycle scale. Red circle indicates primary site of interest.

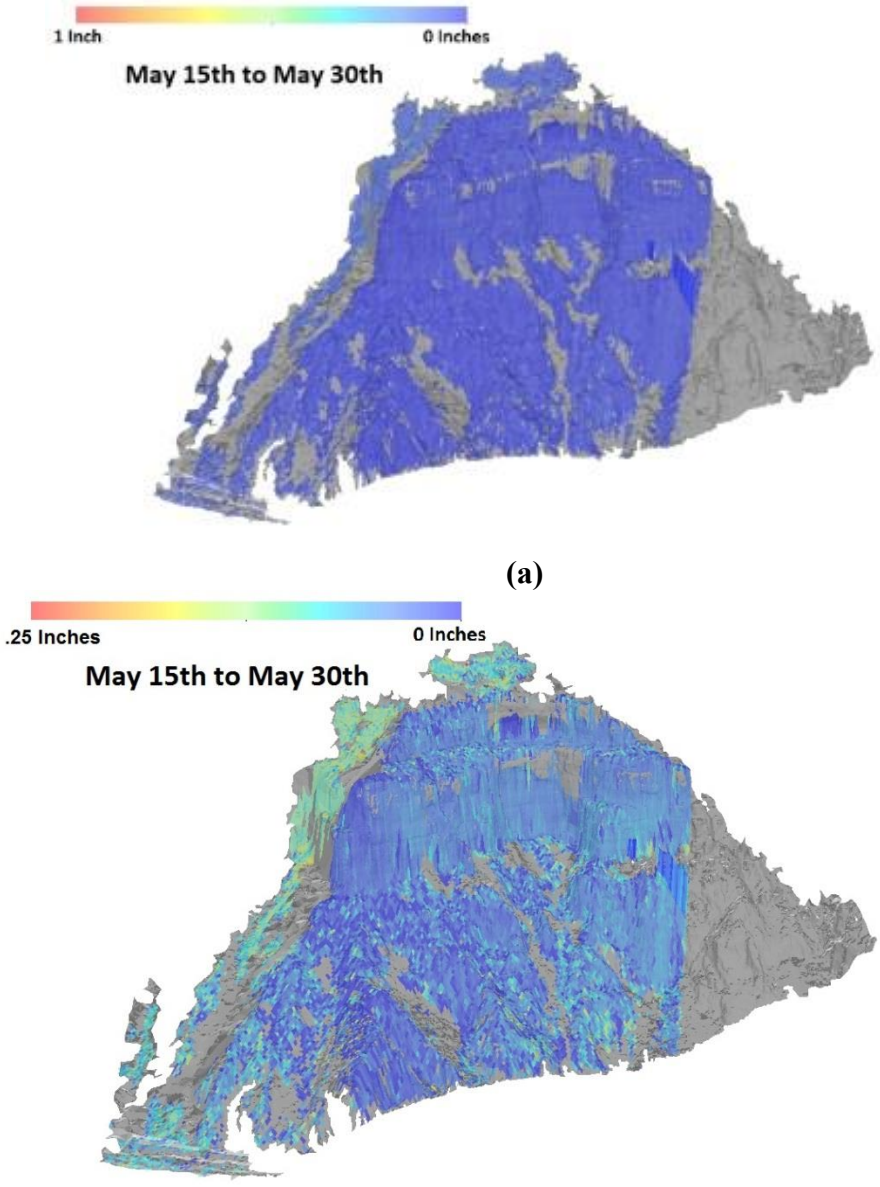

Figure 4.6 Line-of-sight deformation map from May 15, 2012 to May 30, 2012 superimposed over a LiDAR DEM model using (a) 1-inch/cycle scale and (b) ¼-inch/cycle scale.

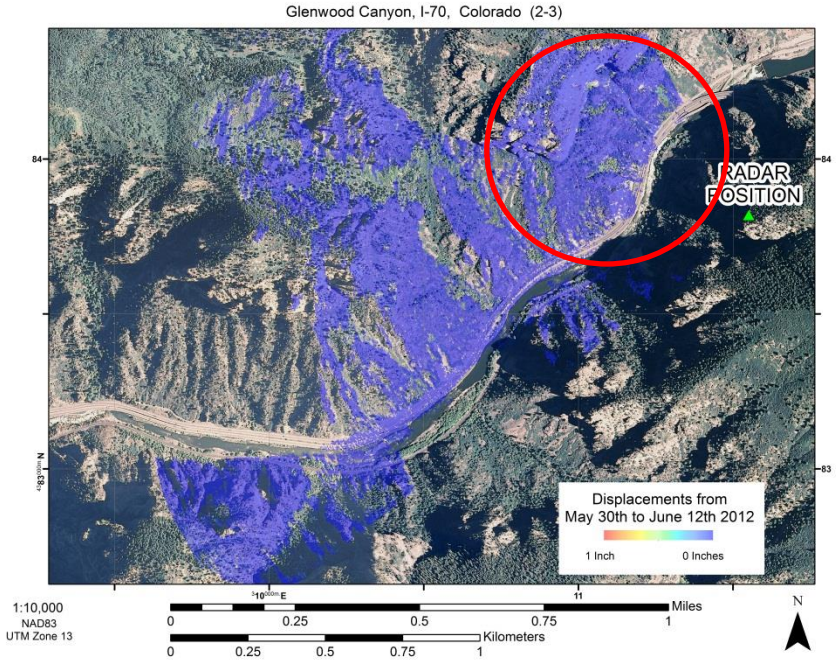

(a)

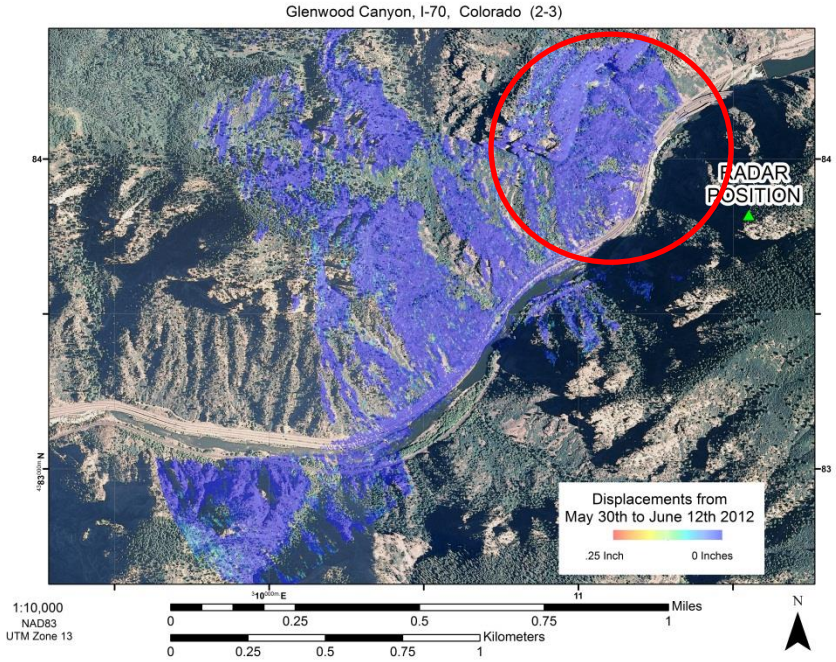

(b)

Figure 4.7 Aerial photo with superimposed line-of-sight deformation map from May 30, 2012 to June 12, 2012 using (a) 1-inch/cycle scale and (b) ¼-inch/cycle scale. Red circle indicates primary site of interest.

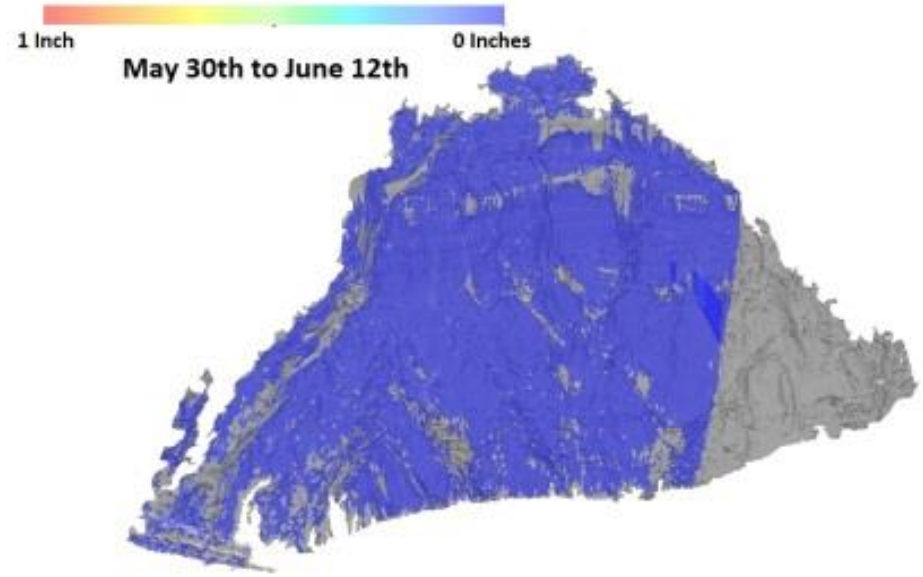

(a)

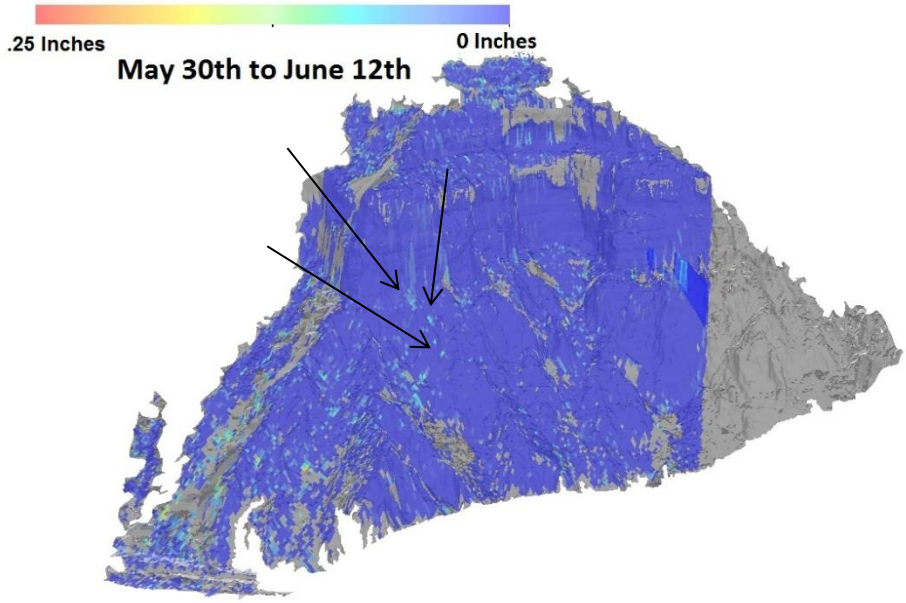

(b)

Figure 4.8 Line-of-sight deformation map from May 30, 2012 to June 12, 2012 superimposed over a LiDAR DEM model using (a) 1-inch/cycle scale and (b) ¼-inch/cycle scale

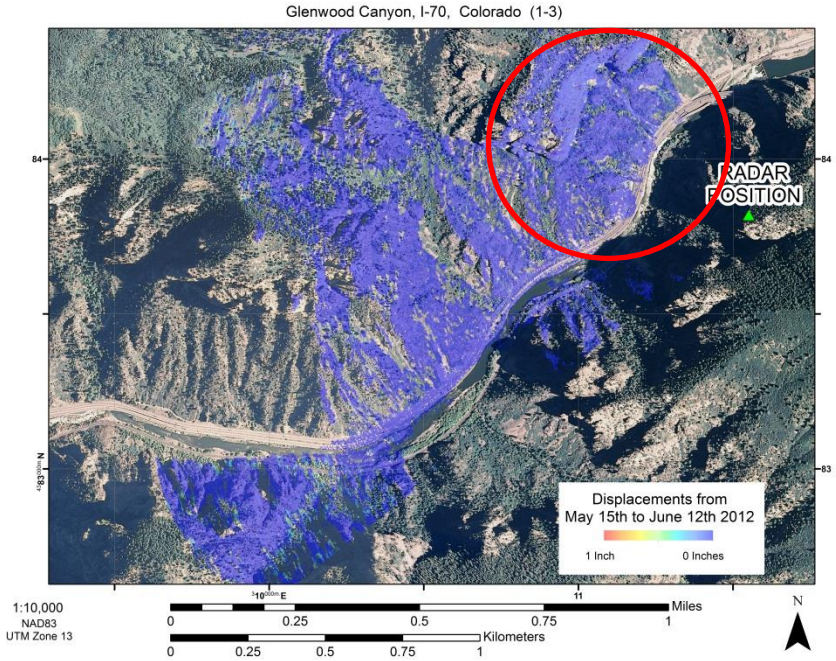

(a)

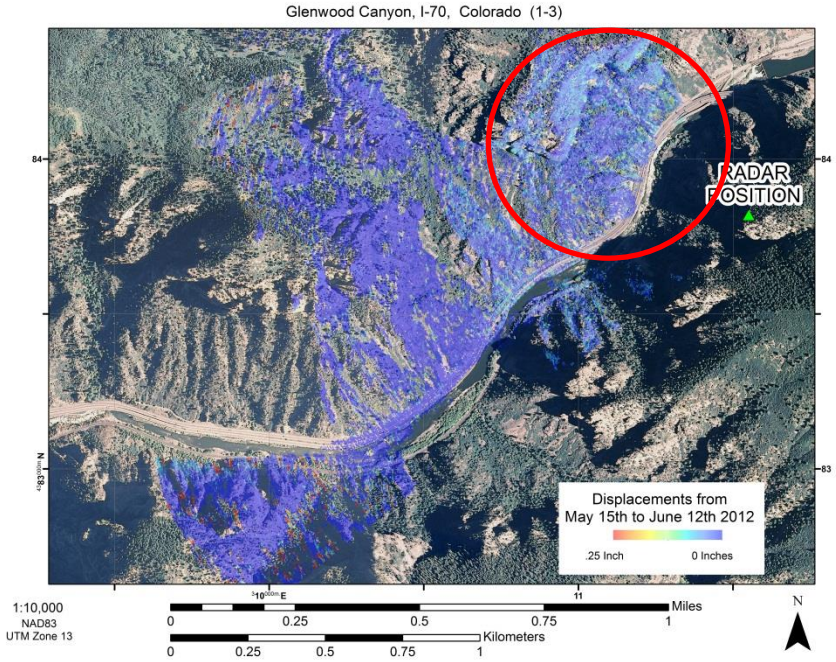

(b)

Figure 4.9 Aerial photo with superimposed line-of-sight deformation map from May 15, 2012 to June 12, 2012 showing (a) 1-inch scale and (b) ¼-inch scale. Red circle indicates primary site of interest.

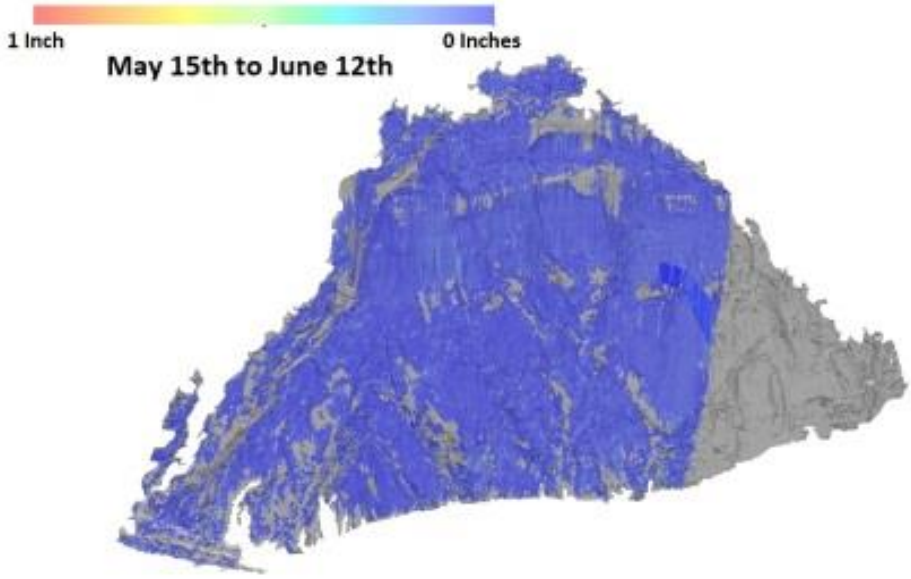

(a)

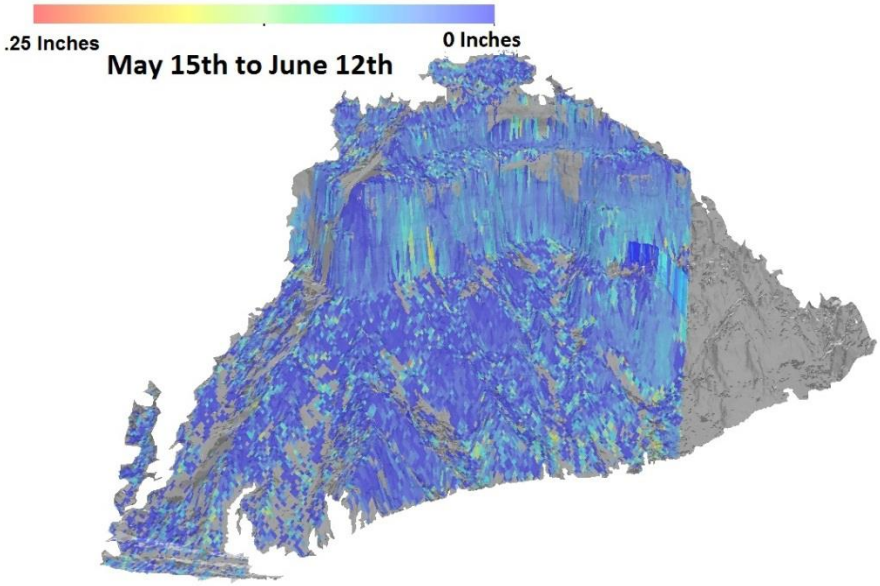

(b)

Figure 4.10 Line-of-sight deformation map from May 15, 2012 to June 12, 2012 superimposed over a LiDAR DEM model using (a) 1-inch/cycle scale and (b) ¼-inch/cycle scale.

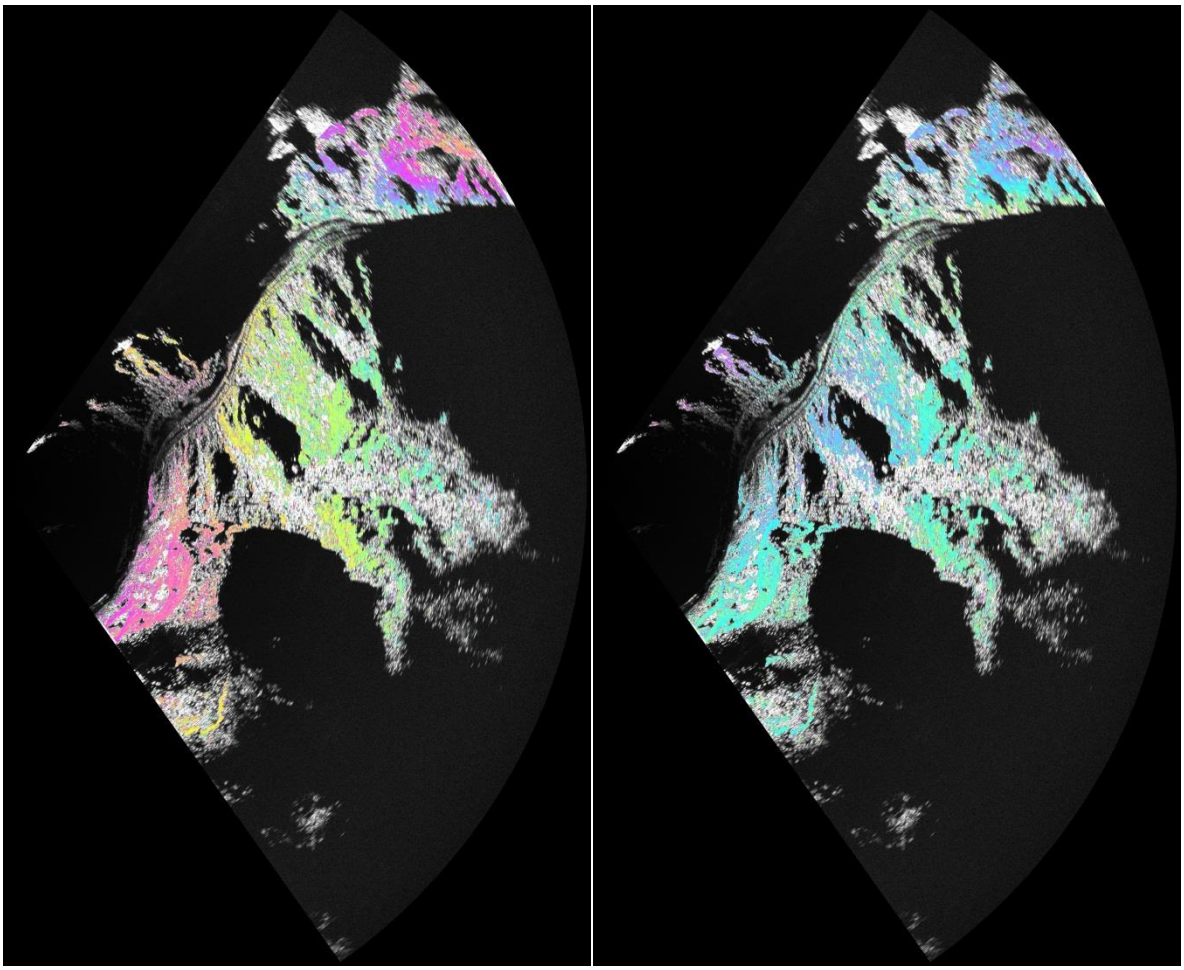

(a) **(b)**

Figure 4.11 Unwrapped interferograms from May 15-May 30, 2012 timespan with a) atmospheric contribution and b) with atmospheric contribution removed

4.3.2 Discussion of Displacement Measurements

The displacement maps with the 1-inch/cycle color scale were produced to allow comparisons to be made with results generated from another GBIR system that was being used to continuously monitor the slope over the same time period. The other system showed some surprising results, with several points appearing to show movements of over a 1 inch per week (Miller, et al., 2013). The displacement maps measured from the study presented in this thesis did not indicate any movements of this scale. The absence of any measured movements in excess of about 0.25 inches over the 2 week to 4 week span is shown by the uniform blue color in each of the plots (Figure 4.6(a) and 4.10(a)) with the color displacement scale of 1-inch/color cycle. Attempts by CDOT to gather ground truth data at some points of interest did not yield meaningful results, so it was not known if any movements truly occurred during the measurement time span. However, if episodic movements of rocks were occurring, it is expected that these movements would be at the mm scale, not at the scale of several inches. The lack of movements in excess of 0.25 inches observed in this study is more consistent with expectations for the magnitude of movements in this environment. It should also be added that other measurements performed at this site (repeat pass LiDAR measurements, high resolution camera) did not detect large-scale movements at this site.

The question of whether smaller-scale (mm) movements of the rock slope occurred during this time frame is more difficult to answer conclusively. When the same displacement data are presented with a smaller displacement scale (¼ in per color cycle) the results appear to show some changes that could be interpreted as movement (e.g. Figure 4.6(b), 4.8(b),4.10(b). For example, in Figure 4.6(b) and 4.10(b), there are several

regions around the cliff face that appear to show displacements in the range of 1/8 to 1/16th of an inch (about 1.5 to 3 mm) as indicated by the cyan color in the plots. These apparent displacements are more likely phase variations attributed to incomplete removal of the atmospheric phase contribution. It is possible for atmospheric conditions in various areas to differ from the general trend of the entire image, thus some residual atmospheric phase can remain after the general atmospheric trend is removed. The large spatial scale interferogram from May 15th to May 30th, shown in Figure 4.5(b), shows incomplete removal of the atmospheric phase trend, which would support the interpretation that variations observed on the cliff face are also due to atmospheric effects. The data from the May 30th to June 12th measurement interval in Figure 4.8 shows a much more complete removal of the atmospheric effects, and a more uniform displacement map in Figure 4.8. There are several localized points in this image that could be interpreted as movements. A few points such points are indicated with arrows in Figure. 4.8. If interpreted as movement, these points would correspond to approximately 4-m by-4 m areas moving about 1.91 mm. Without ground truth data it is not possible to determine conclusively if there were very small localized movements. These results illustrate some of the difficulties involved in trying to detect small magnitude (mm) and localized (pixel size) movements with GBIR. Most previous studies with GBIR have been applied to large spatial scale movements. In these cases, pixel-scale variations in phase are not of concern. There is a need to study and better understand the causes of the phase variations observed in this study. Ideas for future work are presented in Section 4.5.

4.3.3 Discussion of Data Processing Issues

The results presented in Figures 4.5 to 4.11 and discussed previously were obtained from trial and error of different processing schemes until the best result was obtained. The following observations were made regarding the most effective processing procedures for these applications. First, for this application where anticipated movements were only several pixels in size, it was necessary to filter the interferograms (smooth the phase) enough to allow proper unwrapping, without over smoothing the phase such that the displacement signatures were lost. After trial and error, a 32-pixel averaging window was selected as the minimum window size that allowed for successfully unwrapped interferograms. Prior to the unwrapping, a coherence mask was applied (Table 4.2) to remove points with unreliable phase values. However, it was noted that random incoherent speckle in the image survived the masking phase. The random phase had a coherence signature that allowed the noise to survive the coherence masking phase, thus an intensity mask (along with coherence mask) was also applied (Table 4.2). After the phase unwrapping, each unwrapped interferogram was manually inspected as several of the unwrapped interferograms had errors because of gaps in the data arising from areas where phase signatures were not continuous. The non-continuous phase signatures arose from the complicated scene geometry (i.e. non-flat area) and scattered regions of masked low coherence/intensity areas. Interferograms that were not successfully unwrapped were culled from the eventual stacked dataset. Next, individual unwrapped interferogram atmospheric phase ramps were removed prior to stacking since meteorological conditions appeared to change throughout the observation period, even on a given date. Unwrapped interferograms were stacked using all interferograms that were

successfully unwrapped, which allowed for improvements in the quality of the phase estimates.

4.4 Results and Discussion Coherence Measurements

4.4.1 Coherence Measurement Results

Maintaining high coherence values is critical for obtaining high quality interferograms and displacement maps. Low coherence values are masked out and not used in the interpretation of the interferograms. If a large portion of the scene is incoherent, interpretation of the interferogram may not be possible. The radar targets in civil engineering application may be a variety of materials (e.g. concrete, steel, rock, soil, synthetic, etc.) and the time between radar acquisitions may range from minutes to months. This portion of the study was performed to contribute to the second objective of this thesis, which is to measure and quantify short and intermediate-term changes in signal coherence for a variety of materials and time spans. For this study it was only possible to transport the Ku-band system to the site, so no data were obtained using the C-band system.

Coherence images were created by utilizing an algorithm in the GAMMA software called "cc_wave" (GAMMA Remote Sensing AG, 2008). This algorithm computes the magnitude of the coherence for two co-registered SLC images, using Equation 2.13 shown in Chapter 2. To view these images, another algorithm in GAMMA termed "rascc" was employed to generate raster images. During the raster generation process, a minimum level of coherence was selected or masked out. There was no coherence mask used for the coherence study, but one was applied during the

displacement study. No coherence mask was used during the coherence study in order to determine the level of coherence over the entire scene, as a mask would purge values below the acceptable level. Coherence images were calculated for each interferogram calculated (Table 4.3) and the individual coherence images were averaged together. Images of the average coherence values for short (i.e. minutes) and intermediate (i.e. weeks) terms are shown in Figure 4.12. Areas of highest coherence are displayed with brighter colors (i.e. yellow), with areas of medium coherence being shown as purple, lower coherence shown as blue, and coherence levels of zero are shown as black. In addition to the general coherence images, specific regions (Figure 4.13) in each image were selected for coherence monitoring over different timespans. The points selected to be monitored consist of three locations on the rock slope (R1, R2, R3) of interest and two vegetated regions in the scene (V1 and V2). Plots associated with short and intermediate-term, time-dependent coherence monitoring are shown in Figures 4.14 and 4.15. Figure 4.16 shows how the May 15, 2012 dataset coherence values change with varying numbers of scenes input into the average. For each image shown here, each coherence image is relative to the May 15, 2012 master.

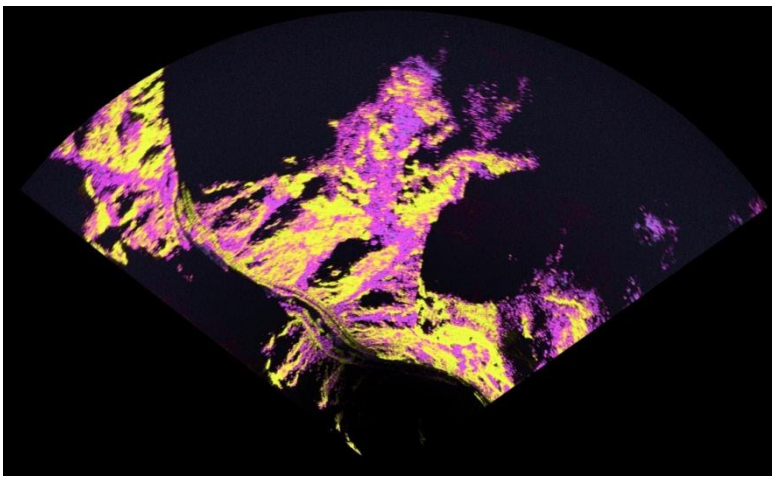

(a)

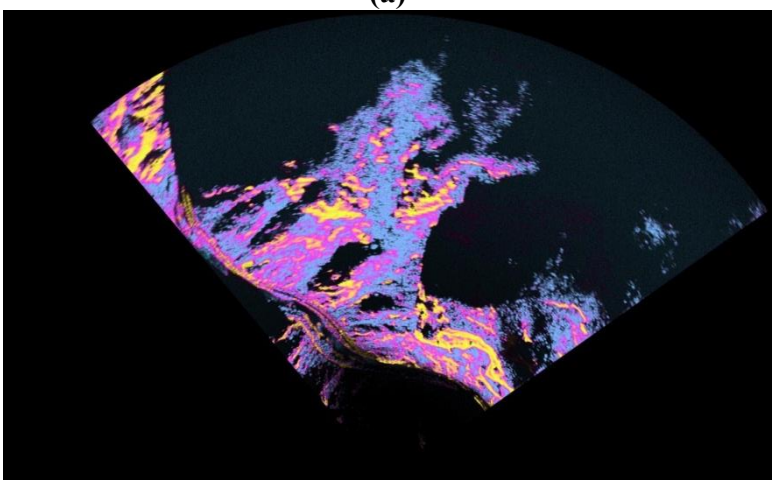

(b)

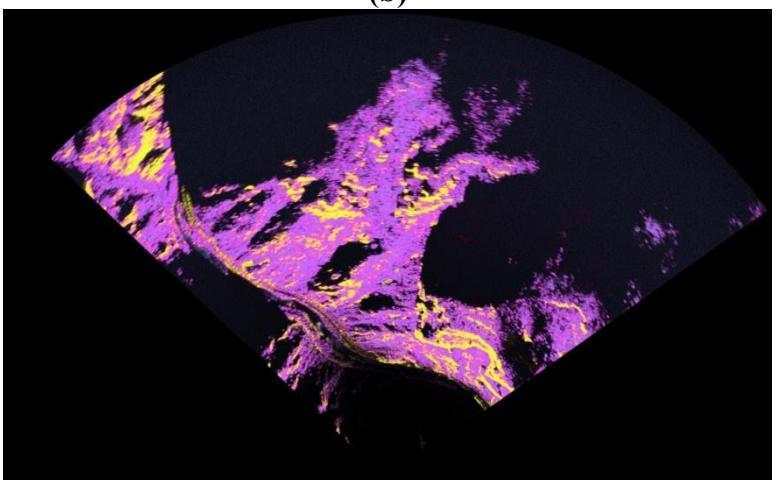

(c)

Figure 4.12 Average coherence image from imagery collected (a) between 5 minutes and 3 hours on May 15, 2012 (b) between May 15 and May 30, 2012 and (c) between May 15 and June 12, 2012 acquisitions. Areas of higher coherence are shown with yellow and areas of low coherence are shown with blue. Moderate coherence areas are denoted with purple, and black is zero coherence.

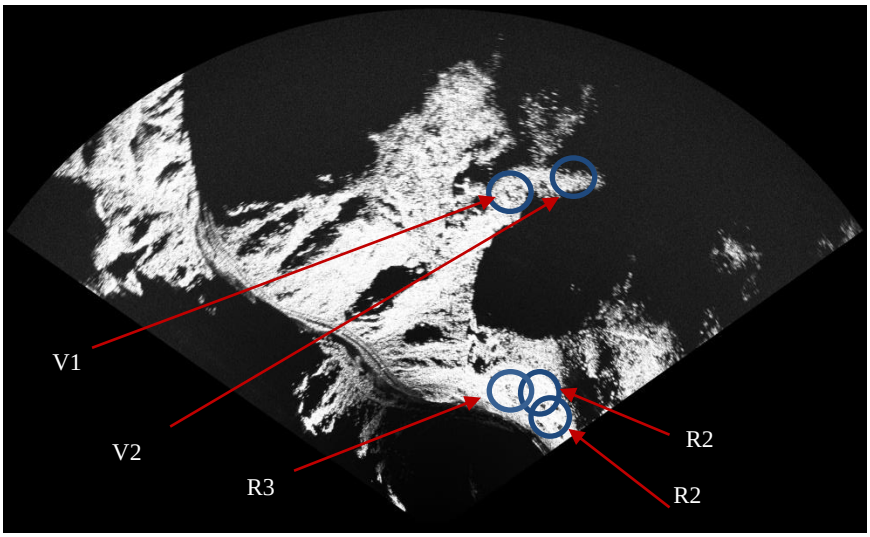

Figure 4.13 Intensity image of a May 15 radar acquisition with monitored coherence areas indicated.

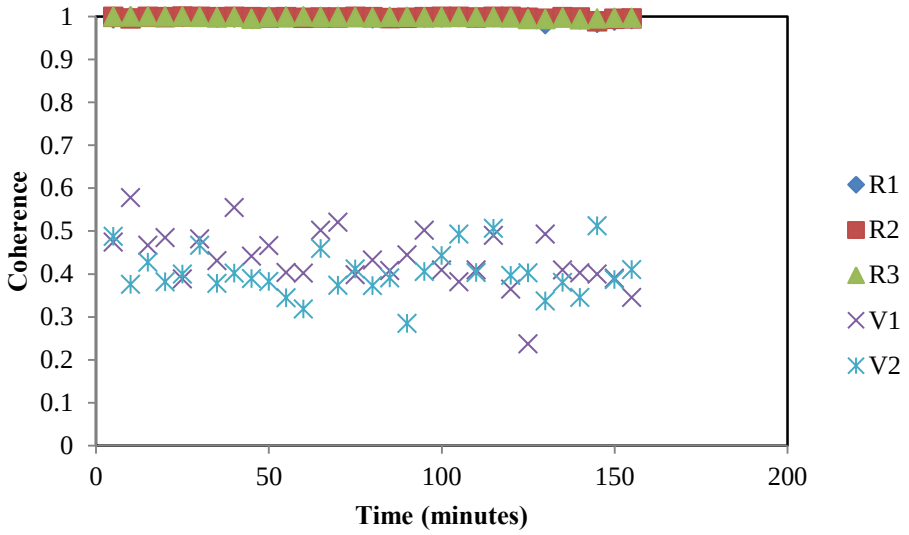

Figure 4.14 Coherence values over different short-term acquisition intervals computed using May 15, 2012 as scene master.

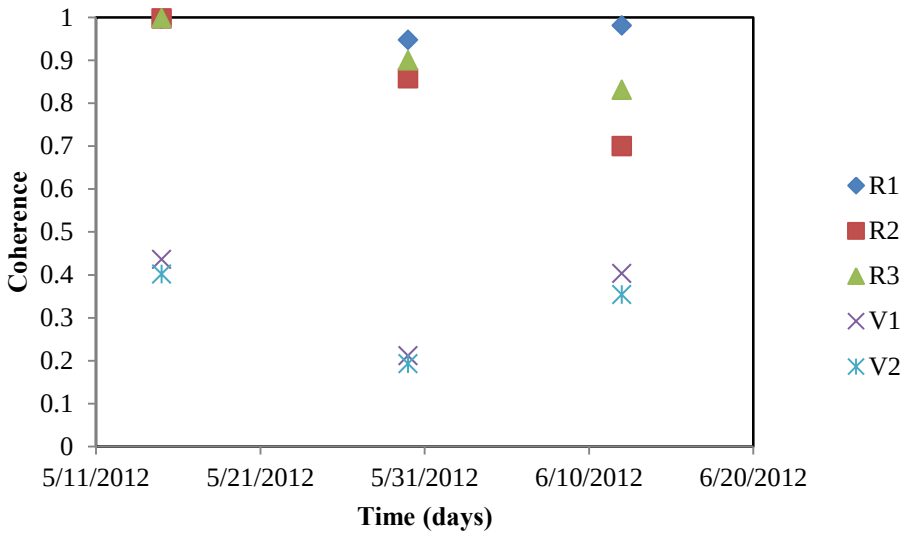

Figure 4.15 Averaged coherence values from over different data collection intervals at Glenwood Canyon, computed using May 15, 2012 scene master

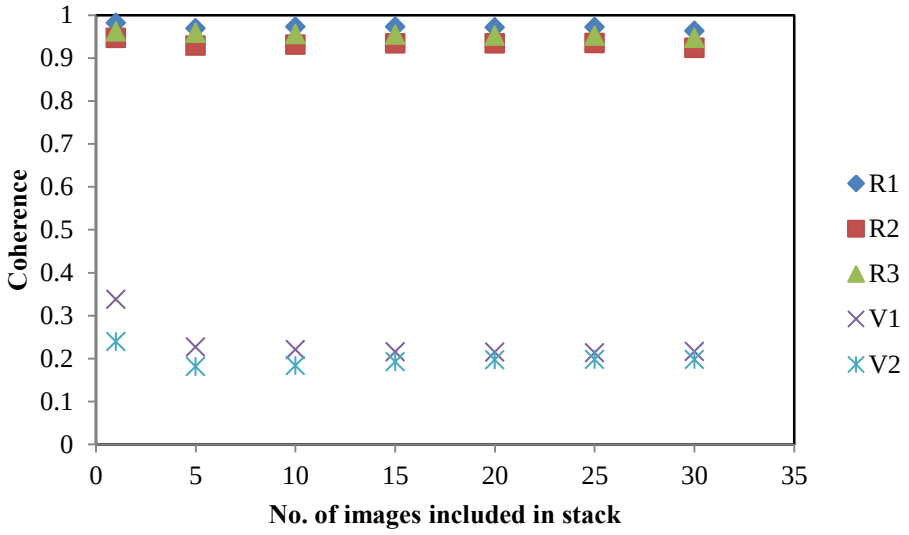

Figure 4.16 Coherence values versus number of images stacked from May 15-May 30, 2012 dataset.

4.4.2 Discussion of Coherence Measurement Results

The single-day, 3-hour coherence results in Figure 4.12(a) show that high coherence (i.e. yellow) is maintained on the rock slope portions of the image, while the vegetated regions (Points V1 and V2) show much lower (i.e. purple) coherence values (although still generally above a cut-off threshold of 0.25). The quantified coherence values over the rock (R1, R2 and R3) and vegetated regions (V1 and V2) show very little change in coherence values over the 3-hr time span (Figure 4.14).

Over intermediate time spans of several weeks the coherence values decrease, as indicated by the changing colors in Figures 4.12(b) and 4.12(c). The quantified values of coherence at R1, R2 and R3 shown in Figure 4.15 generally show a small reduction in coherence over the month-long time span, but all values remain well above typical coherence thresholds (around 0.25). Based on this limited data it appears that the rock face is likely to remain coherent over time frames greater than one month. The quantified values of coherence for the vegetated regions (V1 and V2) did not exhibit a clear coherence trend with time. At the two week interval measurement, coherence values had decreased to about 0.2, however, at the four week measurement the coherence values were again near 0.4 (close to the short term values). The type of vegetation at this site is composed primarily of trees. The low coherence values measured in the short term are likely due to wind moving the trees around and changing the radar reflectors. Over time frames of weeks for this type of vegetation the coherence is likely affected by wind moving the trees around. Therefore, it is not unexpected that the coherence may be variable with time due to changing wind conditions on the different acquisition dates. It

should also be noted that the vegetation in the monitored region is not very dense, which may have contributed to the higher than expected coherence values in some cases.

The coherence values used in this study were calculated using the spatial approach commonly used in satellite processing (Eq. 2.13). Averaging multiple coherence images had little to no effect on the coherence values for this dataset, as shown in Figure 4.16. Unlike satellite measurements, GBIR allows multiple images to be collected over a short time spans. Therefore, a better approach in the future may be to calculate coherence on a pixel-by-pixel basis using multiple interferograms to obtain the coherence estimate.

4.5 Summary and Conclusions

In this chapter, displacement and coherence results from a pilot study of GBIR applied to rockslope monitored conducted with CDOT are shown and discussed. Ground-based measurements were successfully performed at the Glenwood Canyon site in Colorado. No displacements in excess of ¼ in. were observed at the site over the month-long span of the study. However, several areas of phase anomalies consistent with mm-scale movements were identified when using a smaller display scale (i.e. 1/4 inch/color cycle) for the images. Due to a lack of ground truth at this site it is not possible to determine conclusively if these phase anomalies represent true movement or artifacts from data processing. Processing of data at this site presented several challenges, which are documented in this chapter. Detecting mm-scale movements at small spatial scales (pixel size) is a challenging and unique application of GBIR. It was discussed that using a small filter should yield better results, but practically proved difficult since unwrapping

errors persisted as filter sizes decreased To better understand the best practices for processing and interpreting data for this unique application of GBIR, it is recommended that future work focus on sites where the location and extent of movements can be controlled.

Coherence data presented in this chapter indicate that coherence of radar signals from the rock slope portion of the study area remained high throughout the month-long study and are, therefore, likely to remain above threshold levels for longer-term studies. As expected, coherence values of the vegetated areas were much lower and near the threshold values for removal of the data from the processing flow. The coherence values did not show a consistent downward trend with time, but were instead likely controlled by factors such as wind affecting the movement of trees on the slope on a given day.

This study was only a month in duration and it is possible that no movements occurred during this short time span. Future work at this site should focus on a longer year-long study to better capture seasonal movements and track coherence changes with time.

Chapter 5: Long-term Monitoring of an Earth Dam

5.1 Introduction

In this chapter, results are presented from ground-based interferometric measurements performed at an earth dam in Kansas. The objective of this study was to better understand the capabilities and limitations of GBIR for use in long-term monitoring of earth dams. Deformation measurements are an important component of regular dam safety inspections and performance evaluations. A stated objective of the United States Army Corps of Engineers (USACE) dam safety inspection is to "continuously assess the integrity of the dam in order to identify changes over time." (United States Army Corps of Engineers, 2013). The dam safety inspection program is extremely important, as the USACE owns/operates 694 dams in the U.S. The USACE has two general sets of inspection programs, one being an annual inspection to ensure the structure is operated and maintained properly, while the latter is a more rigorous multi-disciplinary inspection which is more infrequent (United States Army Corps of Engineers, 2013). Monitoring of surface deformations typically is performed using widely-spaced point measurements along the dam surface. This coarse sampling of the structure may miss localized deformations. Ground based interferometric radar can provide a spatially continuous deformation map with sub-millimeter sensitivity, allowing for the possible detection of problems before they are visible to the naked eye. Although GBIR appears to be well suited to this application, the potential for loss of data quality over the long intervals between measurements is a possible limitation. The primary objective of this study was to investigate whether sufficient data quality (high coherence)

could be maintained over times spans of several months between measurements. This question was investigated using both the higher frequency (Ku-band) GBIR device and lower frequency (C-band) device. The performance of these systems is compared and discussed

Although the main purpose of this study was not to measure deformations of the dams, some interesting interferograms were generated from this study. These interferograms are presented and discussed. In addition, radar imagery collected at this site presented some unique challenges in the processing and interpretation of the data due to a lack of radar reflections over a large portion of the image. Data processing issues that were encountered and strategies used to overcome these issues are presented and discussed. Presented below is a description of the site, equipment setup and measurements procedures. The data processing procedures utilized are described, and the results from the GBIR deformation and coherence measurements are presented. The chapter concludes with discussion of results and conclusions from this study.

5.2 Description of Field Site and Measurement Procedures

5.2.1 Field Site Description and Data Collection Procedures

Milford Dam is a large earth dam (6300 feet long, 140 feet tall, and 1000 wide at base) located in central Kansas (Figure 5.1) on the Republican River near Junction City, Kansas. The dam is operated by USACE, and was constructed by USACE in the early 1960s (United States Army Corps of Engineers, 2012). There are no known problems or issues with Milford Dam. The dam was selected for this study based on its size and location.

As shown in Figure 5.2, Milford Dam impounds Milford Lake on the west side of the dam. The GBIR measurements presented in this chapter were performed from two vantage points (termed Location 1 and Location 2) on the reservoir side of the north and south abutments where land protrudes into the reservoir (Figure 5.2). The distance to the closest point of the dam from Location 1 is approximately 650 m and from Location 2 is 225 m. The reservoir side of the earth dam is covered with riprap, and the abutments near the observation points are covered with grassy vegetation and some small bushes and trees (Figure 5.2). Figure 5.3 shows a photograph of the dam taken from Location 2. Specific coordinates are referenced in Appendix.

Unlike the GBIR measurements performed at Glenwood Canyon, which used a mast support, the measurements at Milford Dam were performed using the conventional tripod setup over survey pins. The survey pins were 18-in. long, zinc-plated steel rods, which were installed by graduate assistants to a depth of about 17.5-in. By using the tripod setup, the radar was not rigidly attached to the ground surface, thus specific procedures were followed to ensure precise repeatability of the setup each time. These procedures consisted of measuring the azimuth of each tripod leg as well as the amount of extension for each leg, and measuring the distance from the top of the tripod to the monument surface. Azimuth direction measurements were acquired using a compass, and distance measurements were acquired using a measuring tape. The tripod was secured using sandbags or concrete stones to prevent toppling of the GBIR in strong winds. The starting radar scan position (termed the “home run”) was measured using a compass to ensure that the scan region of interest was duplicated during each return measurement.

This measurement was performed prior to powering on the system, but was confirmed after starting up the system.

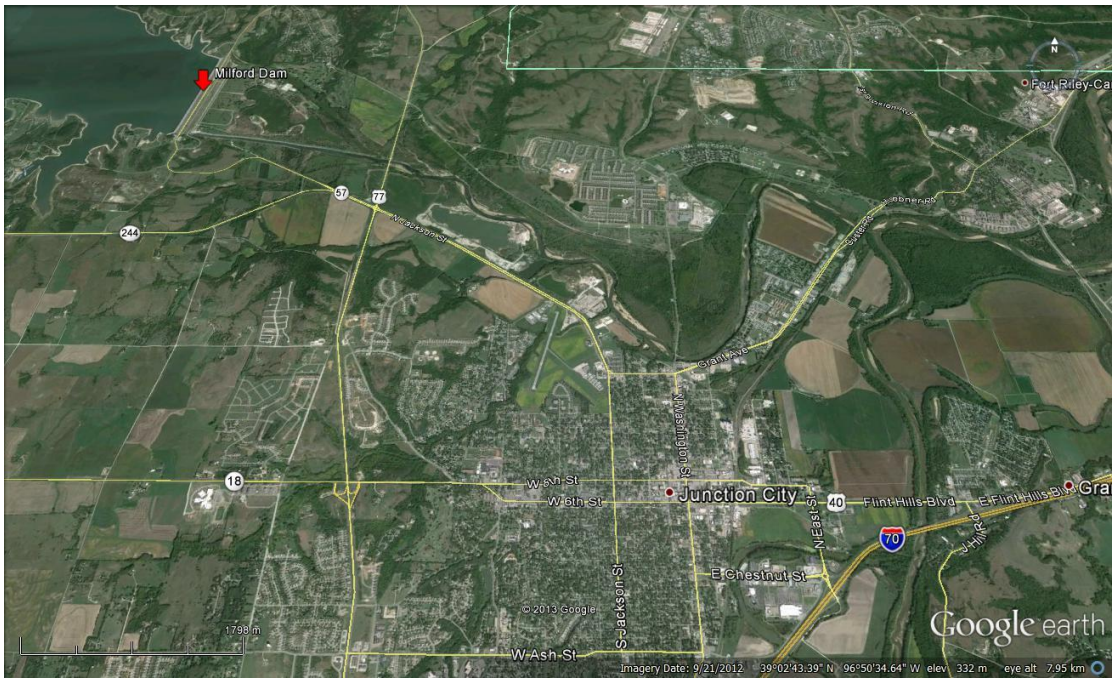

Figure 5.1 Google Earth image of the Milford dam location in relation to Junction City, Kansas.

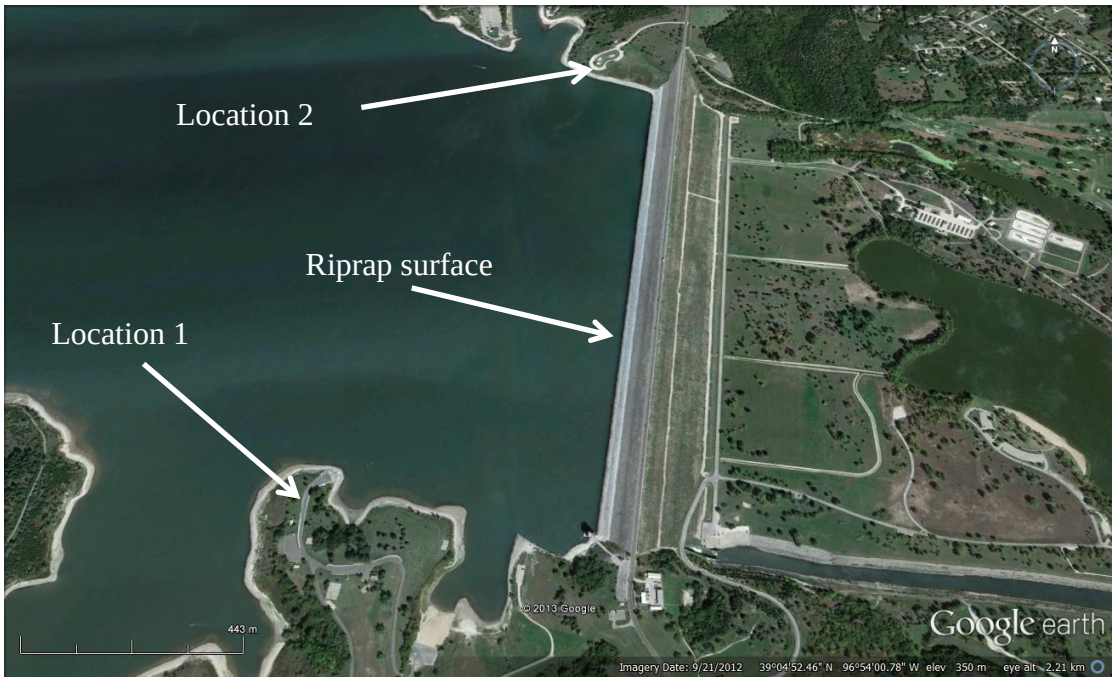

Figure 5.2 Google earth image of Milford Dam showing radar locations relative to dam structures.

Figure 5.3 Photograph of Milford Dam taken from the vantage point of Location 2.

Repeat GBIR measurements were performed at Location 1 and Location 2 using both the Ku-band and C-band systems. During each data acquisition day, approximately

15 Ku-band scans were acquired at 1 minute intervals, while approximately 5 scans were acquired at 2 minute intervals using the C-band device. The measurements were performed over a five-month time span from September 2011 through February 2012. The data acquisition dates using the Ku and C-band systems are shown in Tables 5.2 and 5.3, respectively. The Ku-band acquisitions began in September 2011, while C-band acquisitions began in October 2011 for Location 2 only. Due to operational errors, C-band data acquisition did not start until November 2011 for Location 1. After each measurement, the equipment was completely broken down and removed from the site leaving only the monument pin marking the location of the measurement. Changes in reservoir elevation during the measurement time span were provided by the Kansas City District, USACE (Figure 5.4 and Table 5.1). The reservoir elevation dropped by approximately 12-ft between the first two measurement dates but remained nearly constant (less than 1 feet of elevation change) during the later measurements.

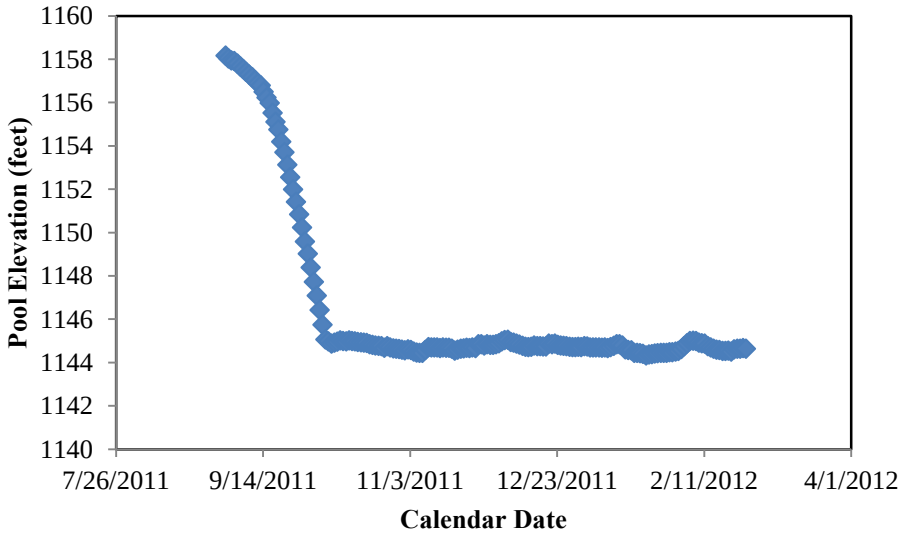

Figure 5.4 Reservoir pool elevation at Milford Dam over the timespan of GBIR measurements.

Table 5.1 Milford dam pool elevations on dates of data acquisition.

Date	Pool Elevation (feet)
Sep-16-11	1156.0
Oct-7-11	1144.9
Nov-17-11	1144.6
Feb-17-12	1144.5

Table 5.2 Acquisition dates using the Ku-band system.

Location	Description	2011			2012
		Sept	Oct	Nov	Feb
1	S. Abutment	18	13	16	16
2	N. Abutment	18	16	16	16

Table 5.3 Acquisition dates using the C-band system

Location	Description	2011		2012
		Oct	Nov	Feb
2	N. Abutment	4	8	4

5.2.2 Processing Procedures

The objective of the data processing was to generate high-quality interferograms between each of the data acquisition dates. Because multiple scans were collected on each data acquisition date, it was possible to stack multiple interferograms to produce a higher quality final unwrapped interferogram. A default processing scheme was established to process all of the data collected at the Milford site. Unfortunately, due to the unique attributes of this site (namely the very small spatial region of coherent signal return) the default approach was not effective for several of the data sets. Therefore, ad-

hoc procedures were employed in some cases. Described below is the default processing procedure applied to each of the data sets, followed by a description of the ad-hoc procedures that were used in some cases. In the description below, each individual radar image containing both amplitude and phase is referred to as an SLC image (single-look complex). The processing procedures used to produce the final images presented in this chapter are summarized in Tables 5.4 to 5.6.

The default processing procedure began with coregistration of each SLC to the first SLC acquired on the reference date (e.g. September 16, 2011 for Ku-band data). Next, each SLC was multi-looked at 1 to 2, meaning that 1-pixel in the range direction and 2-pixels in the azimuth direction were averaged to reduce noise and data file sizes. Interferograms were calculated between individual SLCs from the reference date and the return measurement date. The default filter utilized was the adaptive spectral filter implemented in the GAMMA software, with a relatively small 16-pixel window (chosen to allow for better detection of small spatial-scale deformations). After filtering, each complex interferogram was unwrapped and inspected to confirm that the image unwrapped properly and to identify atmospheric phase ramps in the image. Atmospheric phase ramps were removed by using the GAMMA command "quad_fit". After unwrapping and removal of atmospheric phase, the unwrapped interferograms were stacked (using the stacking algorithm in the GAMMA software) to improve the signal-to-noise ratio. The procedure described above will be referred to as *post-unwrapping stacking* in Tables 5.4 to 5.6.

In some cases the default procedures were not successfully applied, and alternative methods were needed to successfully unwrap interferograms. The problems

encountered with the default procedures can be attributed primarily to the relatively small region of coherent radar returns at this site, due to the presence of incoherent water and the shadowing effect of the dam. Small patches of incoherence on the dam face causing discontinuities in the phase may have disrupted the phase unwrapping algorithm. Also, in cases where low coherence regions were dominated by atmospheric phase effects, the phase continuity may again have been disrupted, resulting in unwrapping errors. These issues required the application of alternative methods or ad-hoc processes to unwrap problematic interferograms. One approach that was used when a problematic scene was identified was to apply a "heavy" filter (i.e. large window and more intense filtering coefficient) to better smooth over incoherent regions in the scene prior to unwrapping. The interferogram was then unwrapped and any atmospheric trend was removed. The atmospheric trend that was removed from the heavily filtered scene was then removed from the original, raw interferogram, and the original default procedure (with the lighter filter) was applied. In many cases, this additional step allowed for successful processing of the data.

In cases where unwrapping failures were caused by low coherence over portions of the dam face, a different stacking technique was utilized. This process termed "*pre-unwrapping*", called for first stacking the wrapped, filtered complex interferograms (using GAMMA algorithm "lin_comb_cpx"), and then unwrapping the stacked complex interferogram. One general assumption with this technique is that image-wide phase values do not vary over the single observation timespan. Meaning, if atmospheric trends were observed between collections they could be removed if the trends themselves did not vary over the single observation span. The atmospheric phase was removed after

unwrapping was completed, using a command in the GAMMA software. Once this atmospheric phase contribution was calculated, the atmospheric phase value was subtracted from the wrapped phase in each complex interferogram to ensure that problematic phase was not affecting real displacement. Once the atmospheric phase was removed from the wrapped complex interferogram, the processing scheme was followed through the filtering and unwrapping stages. The processing procedure utilized for each timespan and location is shown in Tables 5.4, 5.5, and 5.6. Results from utilizing the aforementioned processing methods and discussion of those results are presented in the subsequent displacement and coherence sections. A detailed discussion of the data processing issues at this site is presented in Section 5.3.5.

Table 5.4 Processing information for data collected at Location 1 at Milford Dam using Ku-Band.

Dataset		Interferometry					Unwrapped Interferometry		
Master	**Slave**	**Looks**	**Filter Type**	**Filter Window Size**	**Coherence Mask/ Intensity Threshold**	**Filter Coefficient Used**	**Atmosphere Removed**	**Stacking Technique**	**Images Stacked**
2011 0917	**2011 0917**	1 & 2	ADF	16	0.5/0.25	0.5	NO	Post-Unwrap	16
2011 0917	**2011 1007**	1 & 2	ADF	64	0.25/0.25	0.5	NO	Pre-Unwrap	12
2011 0917	**2011 1118**	1 & 2	ADF	16	0.2/0.25	0.5	YES*	Pre-Unwrap	11
2011 0917	**2012 0217**	1 & 2	ADF	64	0.5/0.25	0.5	YES*	Pre-Unwrap	12
2011 1007	**2011 1007**	1 & 2	ADF	32	0.3/0.25	0.5	NO	Post-Unwrap	8
2011 1007	**2011 1118**	1 & 2	ADF	32	0.3/0.25	0.5	YES*	Post-Unwrap	4
2011 1007	**2012 0217**	1 & 2	ADF	32	0.3/0.25	0.5	YES*	Post-Unwrap	6

*atmospheric model used: a0 + a1*x + a2*y + a3*x*y + a4*x^2 + a5*y^2

Table 5.5 Processing information for data collected Location 2 at Milford Dam using Ku-Band

Dataset		Interferometry					Unwrapped Interferometry		
Master	**Slave**	**Looks**	**Filter Type**	**Filter Window Size**	**Coherence Mask/Intensity Threshold**	**Filter Coefficient Used**	**Atmosphere Removed**	**Stacking Technique**	**Images Stacked**
2011 0917	**2011 0917**	1 & 2	ADF	16	0.5/0.25	0.5	NO	Post-Unwrap	16
2011 0917	**2011 1007**	1 & 2	ADF	16	0.5/0.0	0.5	NO	Post-Unwrap	16
2011 0917	**2011 1118**	1 & 2	ADF	16	0.5/0.25	0.5	YES*	Post-Unwrap	16
2011 0917	**2012 0217**	1 & 2	ADF	16	0.5/0.25	0.5	YES*	Post-Unwrap	12
2011 1007	**2011 1007**	1 & 2	ADF	16	0.5/0.25	0.5	NO	Post-Unwrap	15
2011 1007	**2011 1118**	1 & 2	ADF	16	0.5/0.25	0.5	NO	Post-Unwrap	15
2011 1007	**2011 1118**	1 & 2	ADF	16	0.5/0.25	0.5	YES	Post-Unwrap	15
2011 1007	**2012 0217**	1 & 2	ADF	16	0.5/0.25	0.5	NO	Post-Unwrap	14
2011 1007	**2012 0217**	1 & 2	ADF	16	0.5/0.25	0.5	YES	Post-Unwrap	14

*atmospheric model used: a0 + a1*x + a2*y + a3*x*y + a4*x^2 + a5*y^2

Table 5.6 Processing information for data collected at Location 2 at Milford Dam using C-Band

Dataset		Interferometry					Unwrapped Interferometry		
Master	**Slave**	**Looks**	**Filter Type**	**Filter Window Size**	**Coherence Mask/Intensity Threshold**	**Filter Coefficient Used**	**Atmosphere Removed**	**Stacking Technique**	**Images Stacked**
2011 1007	**2011 1007**	1 & 2	ADF	16	0.5/0.25	0.5	NO	Post-Unwrap	2
2011 1007	**2011 1117**	1 & 2	ADF	16	0.5/0.25	0.5	NO	Post-Unwrap	7
2011 1007	**2012 0217**	1 & 2	ADF	16	0.3/0.25	0.5	YES*	Post-Unwrap	4

*atmospheric model used: a0 + a1*x + a2*y + a3*x*y + a4*x^2 + a5*y^2

5.3 Field Measurement Results and Discussion

Results from interferometric phase and coherence measurements acquired from Milford Dam are presented in this section. The radar imagery is presented in rectangular geometry. To aid the reader's interpretation of the radar imagery, Figure 5.5 provides a front view of the earth dam face with the interferogram superimposed. The two observation points in relation to each other are also shown in this figure. Interferometric phase results will be presented and discussed followed by presentation and discussion of the coherence results. Finally, the data processing issues encountered in this study are presented and discussed.

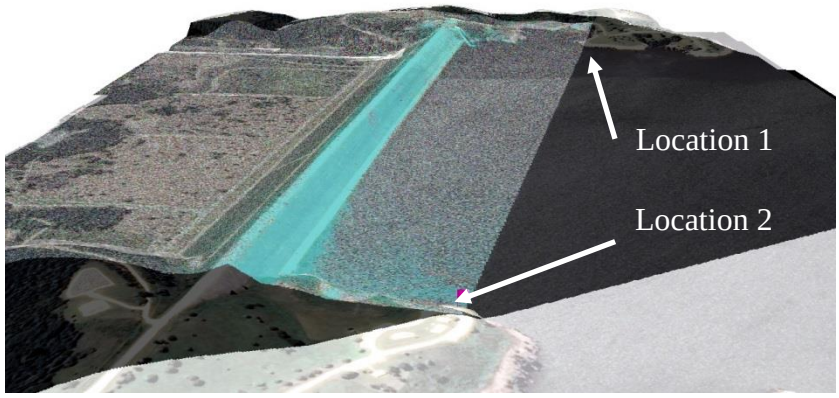

Figure 5.5 Radar interferogram image of Milford Dam acquired from Loc. 2 and superimposed on image of the dam.

5.3.1 Interferometric Phase Measurements

Radar imagery collected at this site were used to develop images of unwrapped interferometric phase. In the absence of other contributions such as noise and atmospheric effects, changes in interferometric phase can be interpreted as movements or deformations in the line of site (LOS) of the radar. Interferograms developed from the Ku-band data collected at Locations 1 and 2 (using the processing schemes summarized in Tables 5.4 to 5.6) and utilizing the September 2011 master, are presented in Figures 5.6 and 5.7, respectively. It is important to note that with the Ku-band device one cycle of phase in the interferograms equates to approximately 7-mm of movement in the line-of-sight of the radar. The color cycle runs from cyan through yellow to purple, and then repeats back to cyan. If no movement occurs, the image should be cyan across the entire image, indicating no change in phase. Interferograms developed from the Ku-band data at Locations 1 and 2 with the October 2011 master, are presented in Figures 5.8 and 5.9, respectively. Next, interferograms developed from the C-band data at Locations 2 using the October 2011 master, are presented in Figure 5.10. Since displacement values are wavelength dependent, and the C-band device operates at a longer wavelength, the displacement associated with one cycle of phase is approximately 28 mm, and is therefore less sensitive to displacements than the shorter-wavelength Ku-band device.

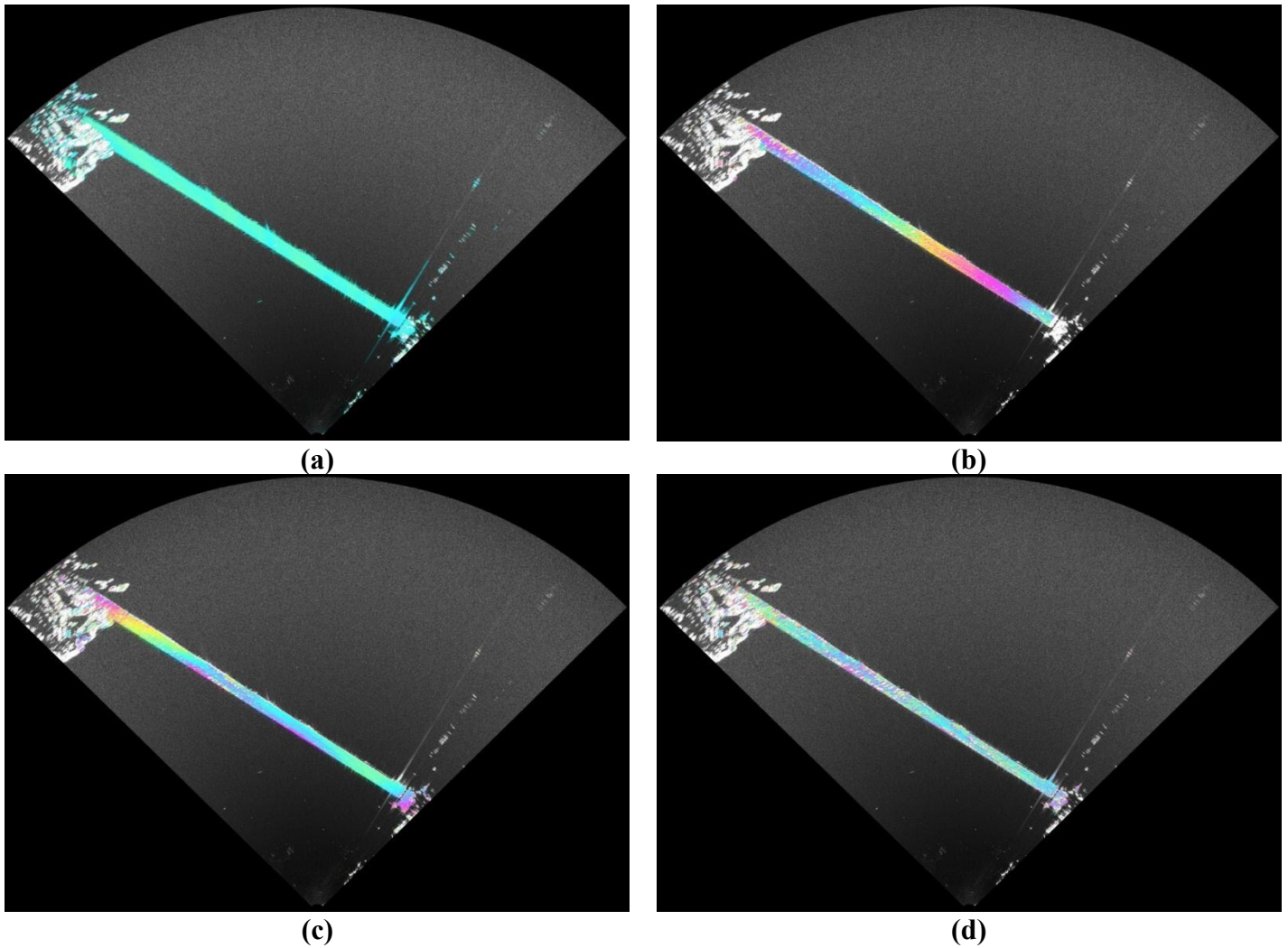

Figure 5.6 Stacked and unwrapped interferograms, using a September 2011 master, acquired at Loc 1 using the Ku-band device over timespans of: (a) minutes, (b) 1-month, (c) 2-months, (d) 5-months. One complete cycle of phase (i.e. cyan, yellow, purple, cyan) correlates to 8mm of line-of-sight movement.

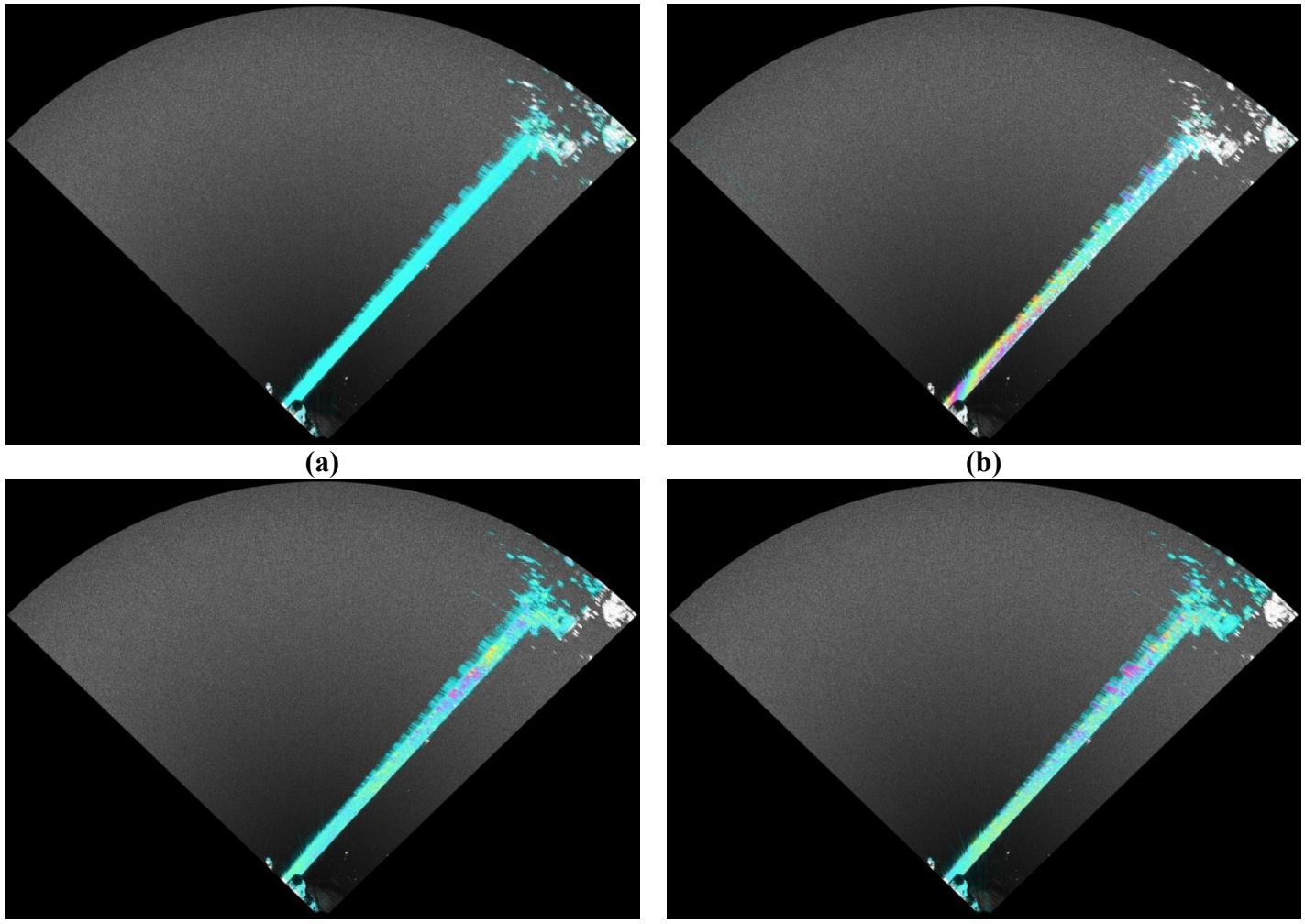

Figure 5.7 Stacked and unwrapped interferograms, using a September 2011 master, acquired at Loc. 2 using the Ku-band device over timespans of: (a) minutes, (b) 1-month, (c) 2-months, (d) 5-months. One complete cycle of phase (i.e. cyan, yellow, purple, cyan) correlates to 8mm of line-of-sight movement.

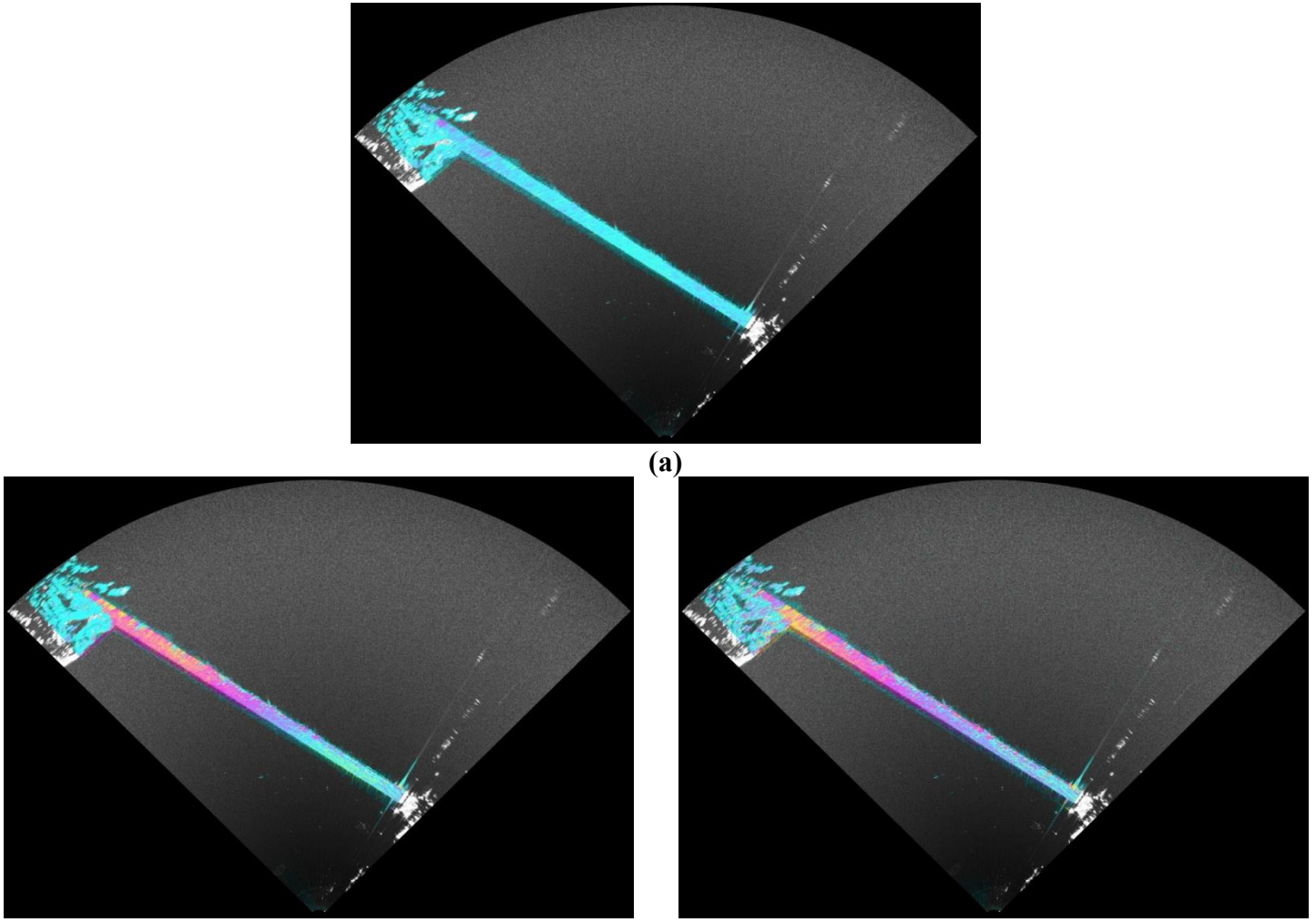

Figure 5.8 Stacked and unwrapped interferograms, using an October 2011 master, acquired at Loc. 1 using the Ku-band device over timespans of: minutes, (b) 1-month, (c) 4-months. One complete cycle of phase (i.e. cyan, yellow, purple, cyan) correlates to 8mm of line-of-sight movement.

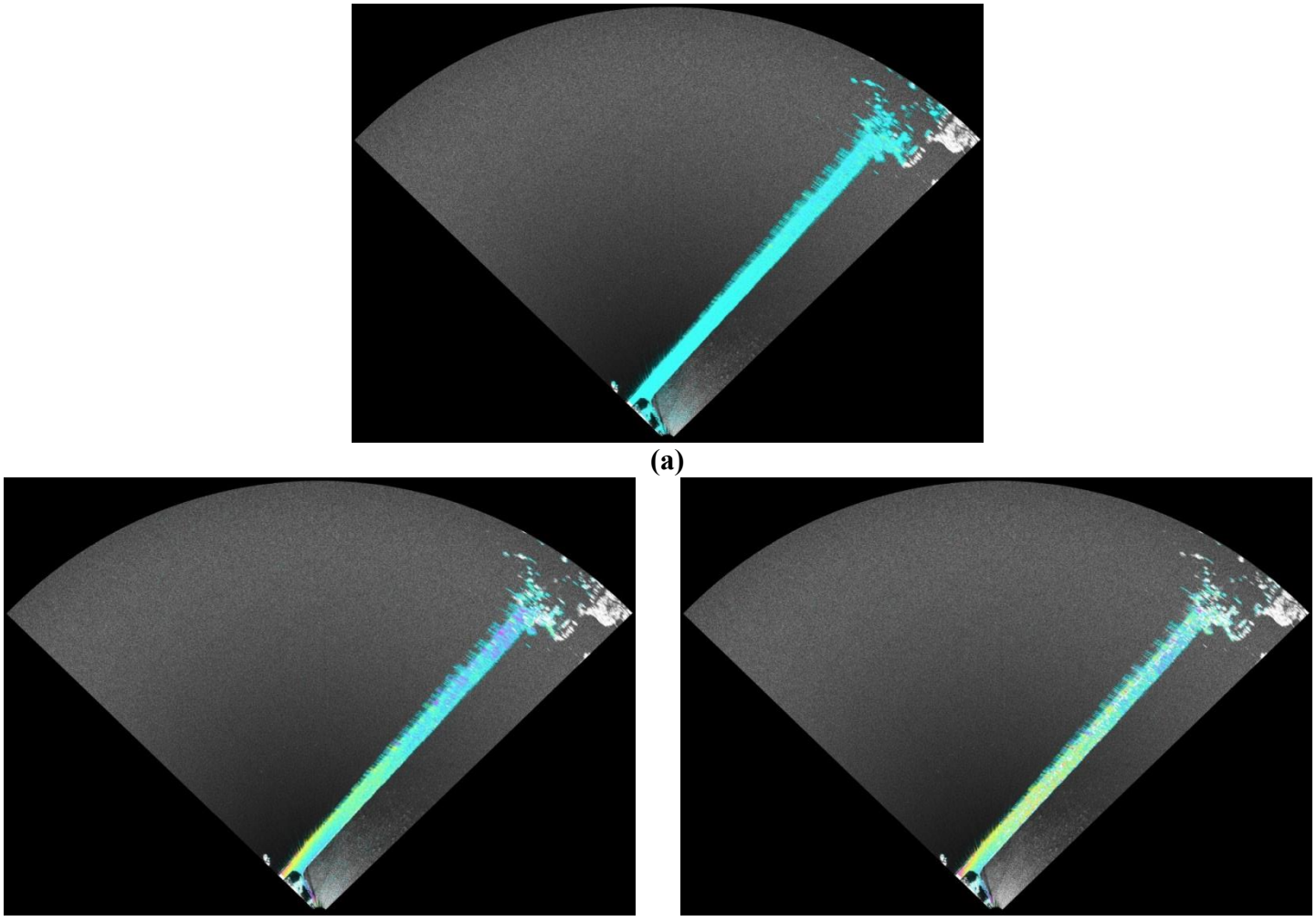

(a) **(b)** **(c)**

Figure 5.9 Stacked and unwrapped interferograms, using an October 2011 master, acquired at Loc. 2 using the Ku-band device timespans of: minutes, (b) 1-month, (c) 4-months. One complete cycle of phase (i.e. cyan, yellow, purple, cyan) correlates to 8mm of line-of-sight movement.

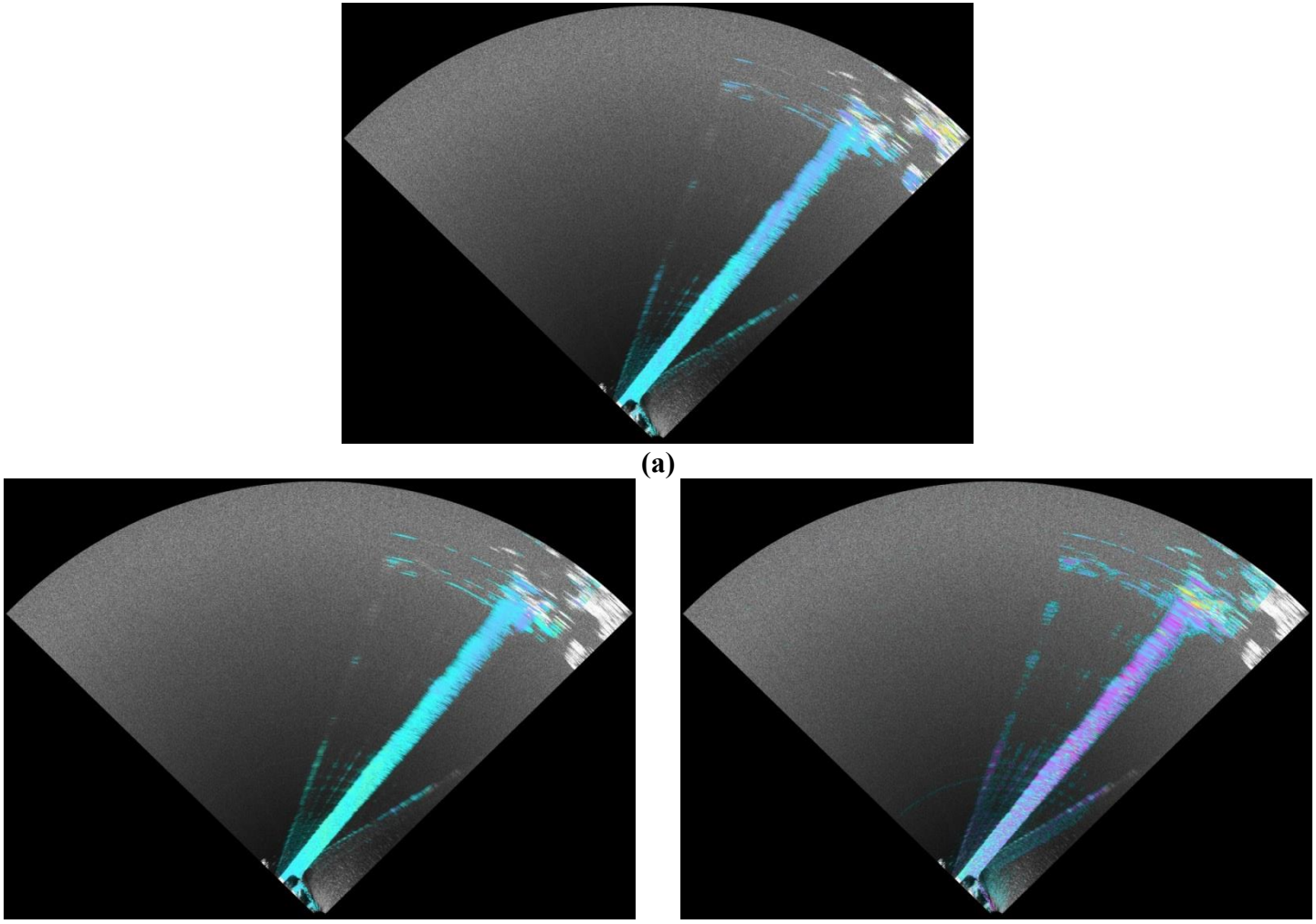

(a) **(b)** **(c)**

Figure 5.10 Stacked and unwrapped interferograms, using an October 2011 master, acquired at Loc. 2 using the C-band device over timespans of: minutes, (b) 1-month, (c) 4-months . One complete cycle of phase (i.e. cyan, yellow, purple, cyan) correlates to 28mm of line-of-sight movement.

5.3.2 Discussion of Interferometric Phase Measurements

Figures 5.6(a) and 5.7(a) show the interferometric phase measured from data acquisitions spaced only minutes apart. As expected, the entire dam face is cyan, indicating no change in phase and hence no displacement during this short time span. For the one-month measurement (September 2011-October 2011 timespan) with the Ku-band system, shown in Figures 5.6(b) and 5.7(b), a phase anomaly is evident in each figure. If the anomaly in Figure 5.6(b) is interpreted to be the result of movement of the dam, it equates to about 8 mm of displacement, and the anomaly in Figure 5.7(b) equates to about 5 mm of displacement toward the radar. The reservoir elevation dropped by about 12-feet during this time span, which suggests that the phase anomalies observed in these figures are the result of the movements of the dam due to unloading on the face of the dam. Under this change in loading, one might expect the predominant movement to be horizontal movement and normal to the longitudinal axis of the dam. It is important to understand that if this was the case, the GBIR would not record an equal phase change along the length. Instead, since the phase change is proportional to the cosine of the angle between the radar LOS and the direction vector, greater changes in phase should be observed for points on the dam that are close to the radar location where the cosine of the angle is larger (Figure 5.11). This expected phase ramp pattern is consistent with what was measured from Locations 1 and 2, as shown in Figures. 5.6(b) and 5.7(b).

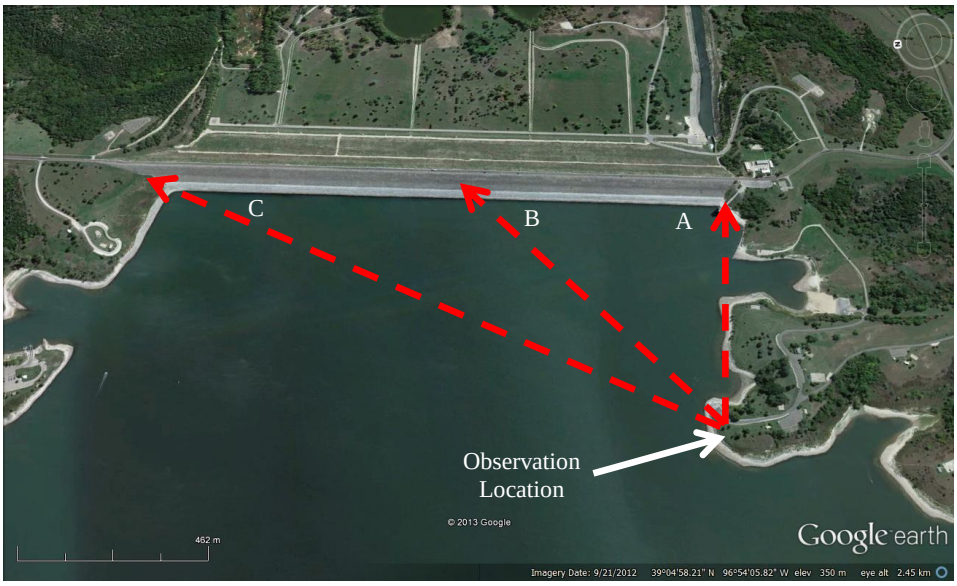

Figure 5.11 Example demonstrating different look angles along the dam face, from Loc. 1, as the radar sweeps over the dame face. View "A" would be most sensitive to deformation, while View C, would be the least sensitive to horizontal deformation of the embankment dam.

The anomalies observed in the September 2011-October 2011 timespan from both observation points exhibited phase changes that were consistent with horizontal deformations of 5 to 8 mm in the line of sight of the radar. No ground truth data was available to confirm that the dam did move slightly due to the change in reservoir elevation. However, based on measurements of other dams reported in the literature, it is certainly plausible that movements of this magnitude may occur. For example, Tedd et al. (1991) present deformation measurements of an earth dam during reservoir elevation changes, where partial drawdown of the reservoir resulted in horizontal deformations of approximately 10 mm in the upstream direction. However, imagery acquired over longer time spans using the September master (i.e. Figures 5.6(c), 5.6(d) and 5.7(c), 5.7(d)) did not show the same phase changes as were observed in the September 2011-October 2011 timespan. Given the constant reservoir level after the October measurements it was expected that the interferograms should have shown similar phase anomalies.

Furthermore, the interferograms developed using the October master, Figures 5.8, 5.9, 5.10, (no reservoir change) did not show any movement. Therefore, it is possible that the phase anomalies may have been artifacts of the processing or atmospheric effects.

Interferograms were developed from both the Ku-band and C-band measurements using the October acquisition as the master (Figures 5.8, 5.9, and 5.10). Due to technical difficulties, C-band data is only available for Location 2. Observing the only C-band data available in this study, no phase trends consistent with expected dam movements are present in Figure 5.10(a), (b), or (c). It appears that some atmospheric trends remained in Figure 5.10(c), even though an atmospheric model was applied to the dataset. The fact that no movement was observed with the less sensitive C-band device is not surprising giving the fact that higher-sensitivity Ku-band radar device did not detect any movement either.

5.3.3 Coherence Measurements

Development of interferograms requires that coherence levels are maintained during the time interval between measurements. In this section, coherence values are quantified and compared as a function of time (minutes to months), surface material (riprap versus vegetation) and radar frequency (Ku-band versus C-band). The coherence images presented in this section are "averaged" or stacked coherence images, meaning that several coherence images (each from a single interferogram) were included in the stack for a given time span. To quantify spatial coherence for specific locations on or near the dam face, several areas were selected where coherence was monitored, as shown in Figure 5.12. The "R" designates sections along the midslope of the dam with riprap

face and “V” designates vegetated regions on the abutments. Coherence imagery developed utilizing the September 2011 master and Ku-band system are shown in Figures 5.13 and 5.14, and the quantified coherence values for designated areas is shown in Figure 5.15. For each data point, approximately 15-pixels were averaged in close proximately to obtain the coherence value. Coherence imagery from data acquired using the Ku-band system and utilizing the October 2011 master is shown in Figure 5.16. Spatial coherence images acquired utilizing the C-band system and the October 2011 master are shown in Figure 5.17, and the quantified coherence for designated regions is shown in Figure 5.18. Finally, a quick note on interpretation of coherence imagery; brighter colors (i.e. yellow) indicate higher coherence values on the order of 0.7-1.0, purple indicates midrange coherence of approximately 0.4-0.7, blue indicates low values of coherence 0.0-0.4, and black represents zero coherence.

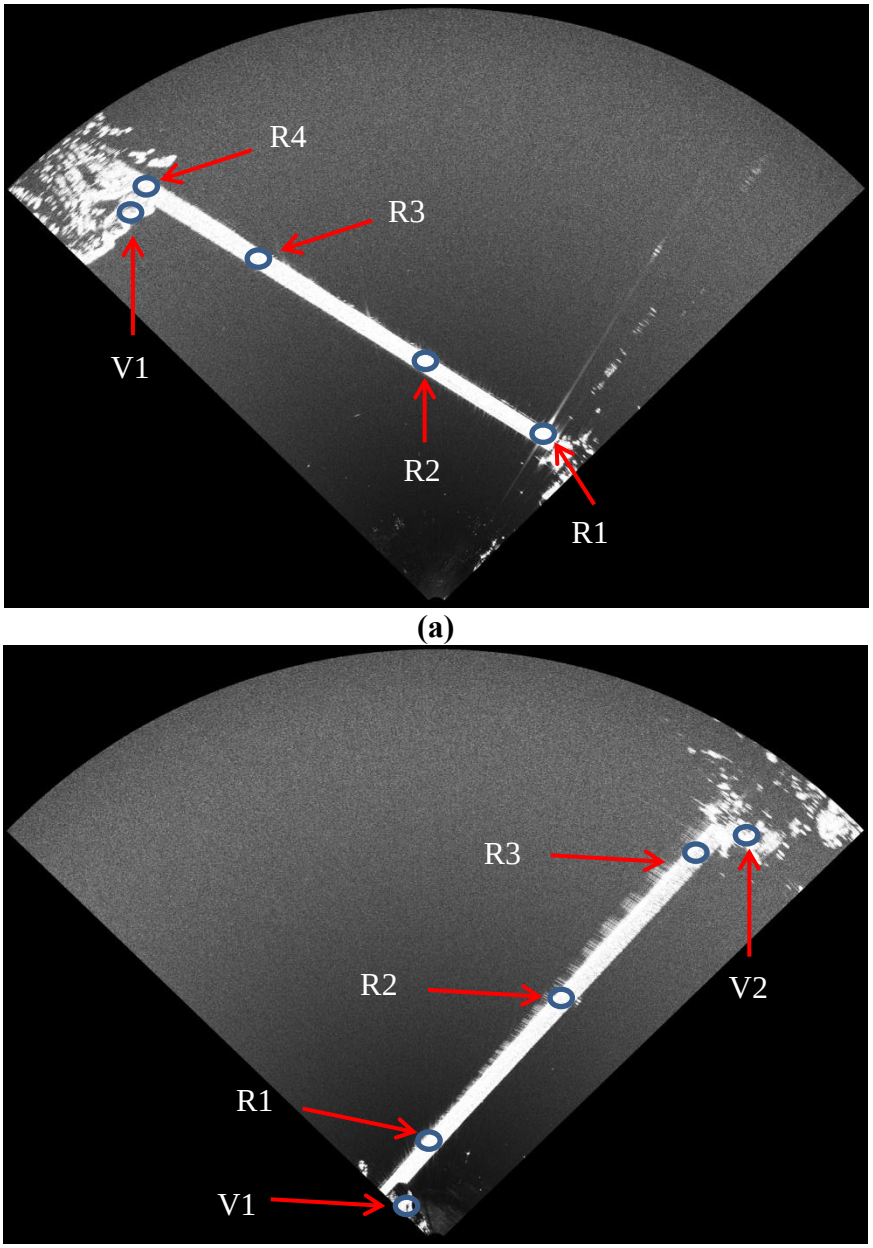

Figure 5.12 Radar intensity image with coherence locations marked for (a) Loc. 1 and (b) Loc. 2 at Milford Dam. Locations labeled with "R" are points on the riprap face, and locations labeled with "V" are vegetated areas.

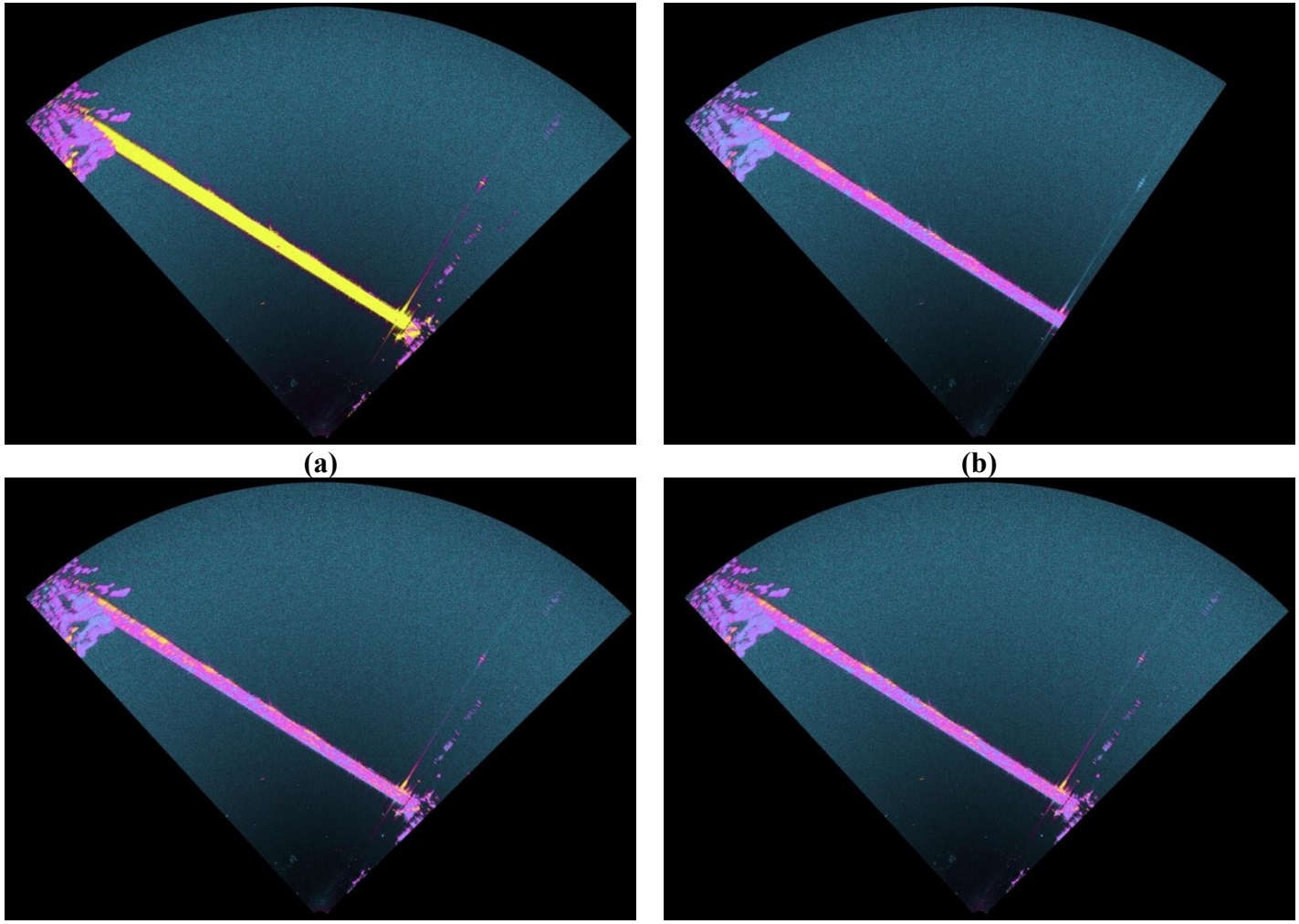

Figure 5.13 Stacked coherence imagery, using a September 2011 master, acquired at Loc. 1 using the Ku-band device over different timespans: (a) minutes, (b) 1-month, (c) 2-months, (d) 5-months. Yellow areas represent coherence values from 0.7-1.0, purple represents values from 0.4-0.7, blue represents values from 0.0-0.4, and black represents areas of zero coherence.

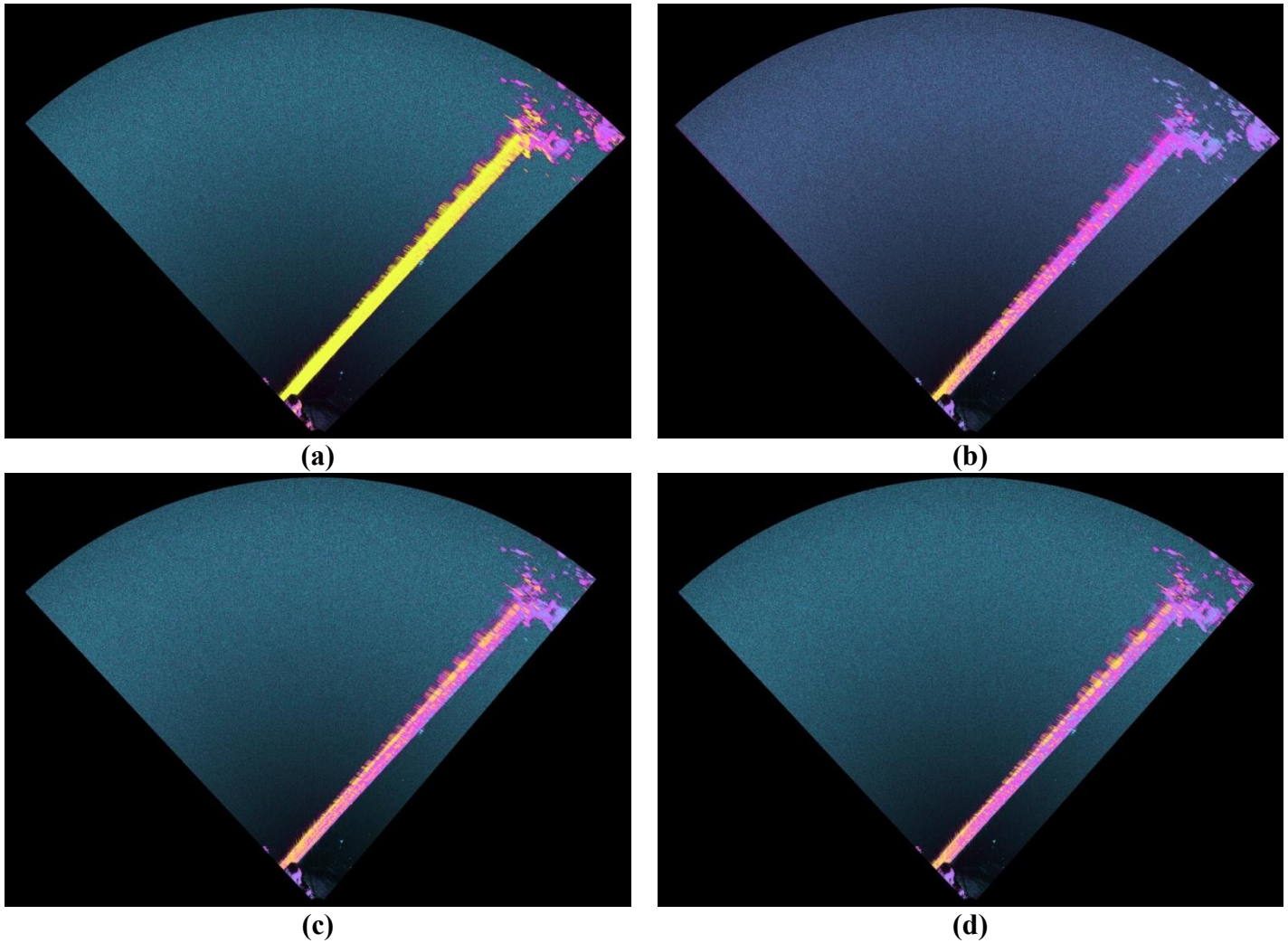

Figure 5.14 Stacked coherence imagery, using a September 2011 master, acquired at Loc. 2 using the Ku-band device over different timespans: (a)minutes, (b) 1-month, (c) 2-months, (d) 5-months. Yellow areas represent coherence values from 0.7-1.0, purple represents values from 0.4-0.7, blue represents values from 0.0-0.4, and black represents areas of zero coherence.

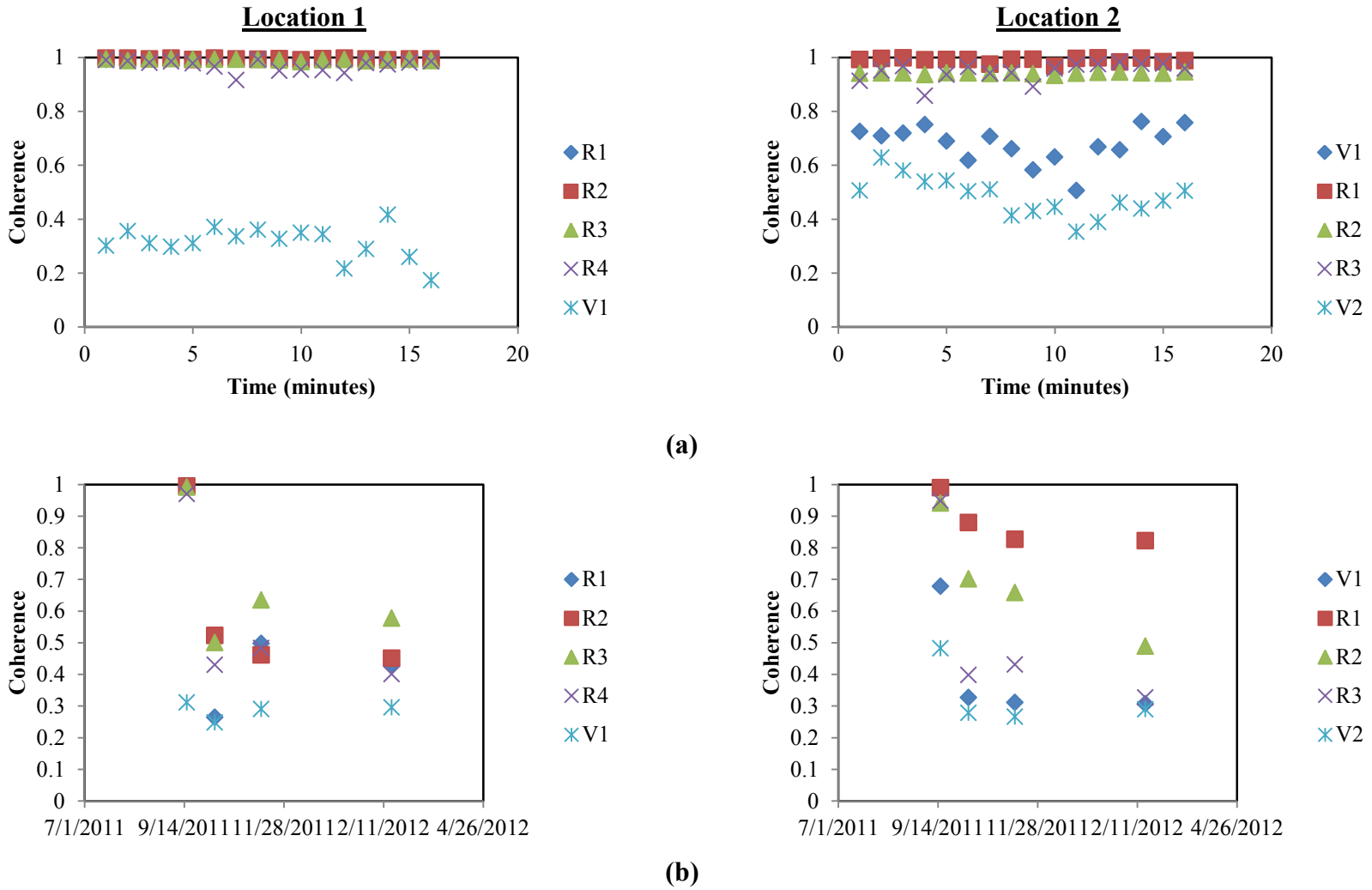

Figure 5.15 Time-dependent coherence derived using the September master (Ku-band) for (a) short and (b) long terms at Loc. 1 and 2

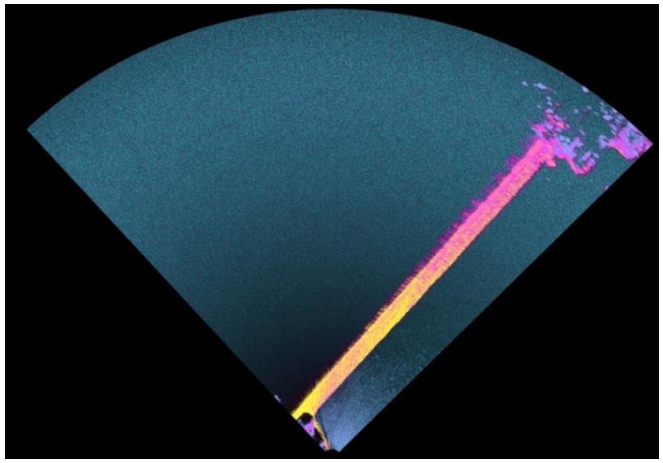

(a)

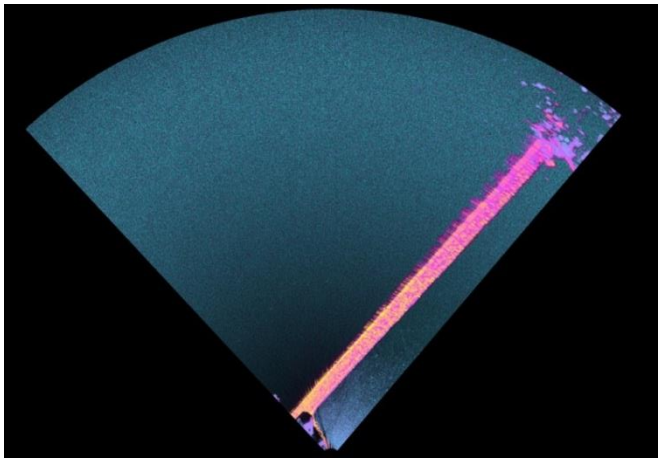

(b)

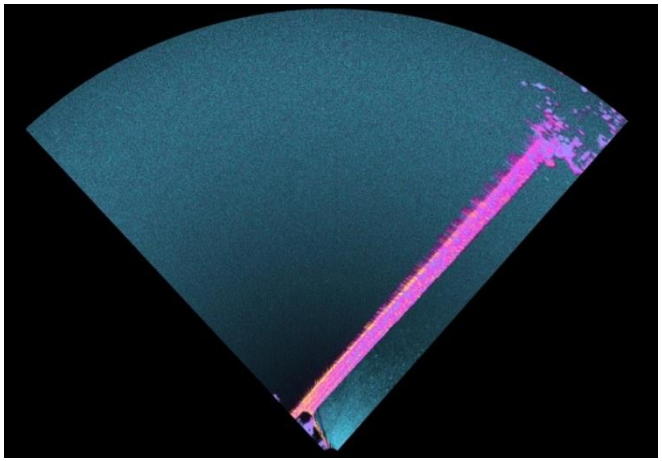

(c)

Figure 5.16 Stacked coherence imagery, using an October 2011 master, acquired at Loc. 2 using the Ku-band device over different timespans: (a) minutes, (b) 1-month, (c) 4-months. Yellow areas represent coherence values from 0.7-1.0, purple represents values from 0.4-0.7, blue represents values from 0.0-0.4, and black represents areas of zero coherence.

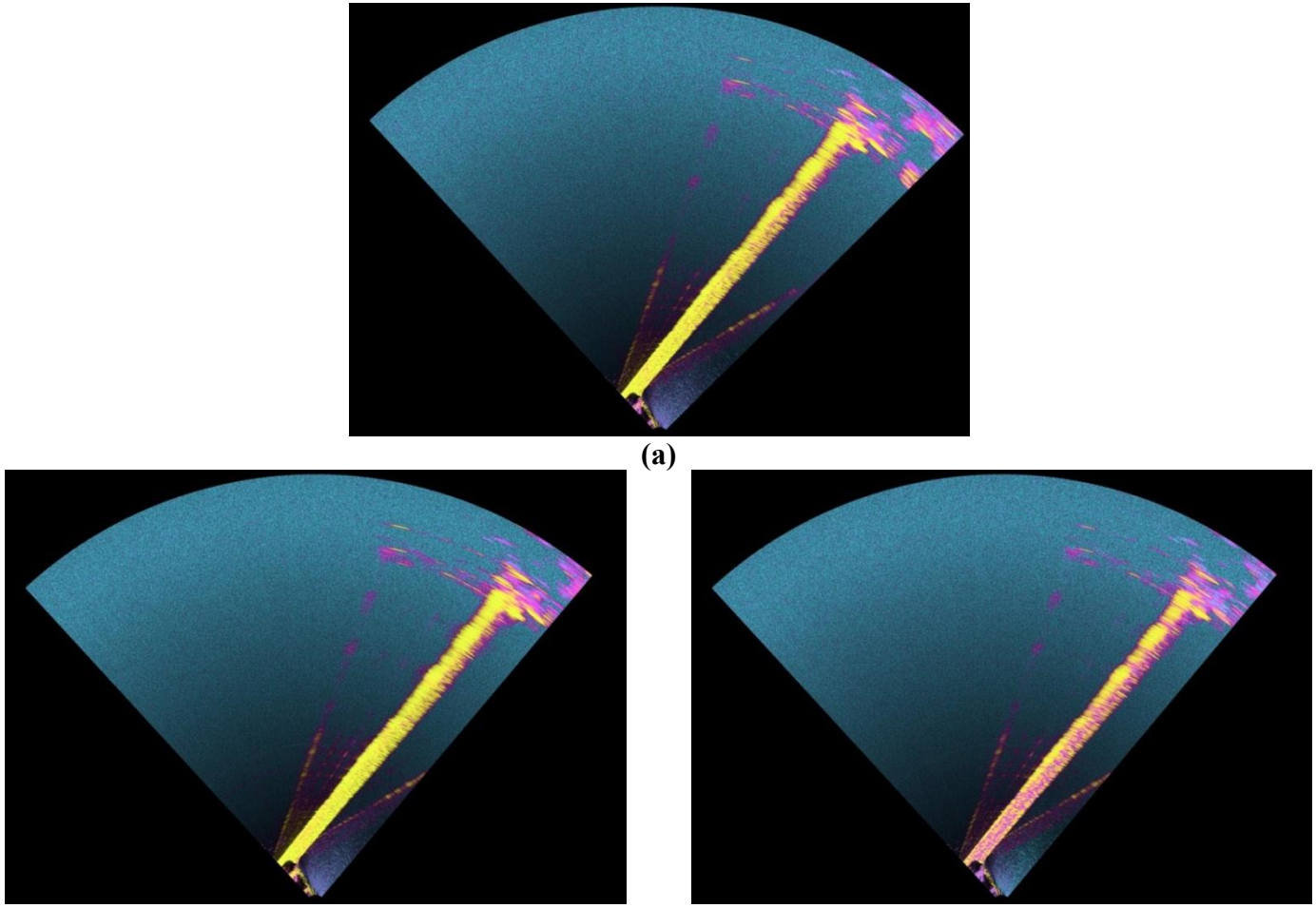

Figure 5.17 Stacked coherence imagery, using an October 2011 master, acquired at Loc. 2 using the C-band device over different timespans: (a) minutes, (b) 1-month, (c) 4-months. Yellow areas represent coherence values from 0.7-1.0, purple represents values from 0.4-0.7, blue represents values from 0.0-0.4, and black represents areas of zero coherence.

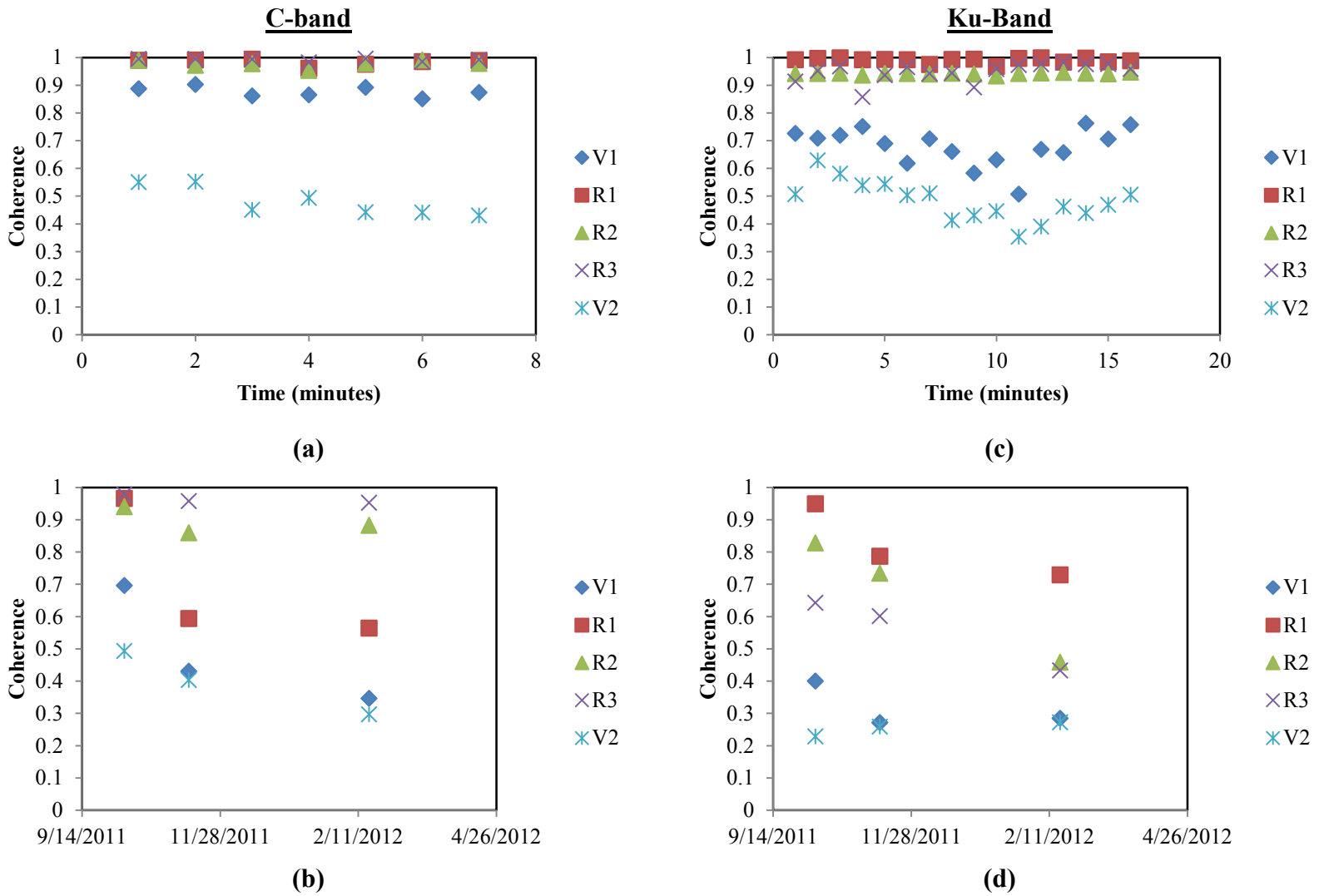

Figure 5.18 Time-dependent coherence derived using an October master for (a) short and (b) long terms using C-band, and (c) short and (d) long term coherence using Ku-band at Loc. 2

5.3.4 Coherence Measurements Discussion

High levels of coherence between radar imagery are an essential part of interferometric processing. Qualitative and quantitative assessments of coherence are valuable for understanding how coherence changes both temporarily and spatially at this site. To quantify coherence in this study, several points were selected in different areas of the imagery acquired from both locations (Figure 5.12), as was discussed previously in Section 5.3.3. Observing the coherence images collected with the Ku-band device using a September 2011 master (Figure 5.13 and Figure 5.14), it can be seen that coherence over the dam area degrades with increasing time intervals between acquisitions. Looking at the images acquired over a time span of several minutes, coherence is initially very high, but for repeat measurements acquired 1 month later, coherence levels have dropped. While qualitative measurements are useful, it is important to quantify these coherence results in relation to typical threshold values. The data presented in Figure 5.15 shows that coherence remains high on the riprap surface over the short-term (i.e. minutes), while the vegetated regions are at much lower values. It is important to note that while the vegetated areas vary, the coherence values are generally higher than the common lower limits usually placed on coherence during processing. Over the long-term, coherence on the riprap face decreased but stabilized and remained above typical coherence thresholds, while vegetated areas experienced a drop and stabilized with values generally below threshold limits.

Coherence values from measurements generated using different system frequencies were also studied. C-band data were only available from Location 2 using an October master (Figure 5.17) which was compared with data collected with the Ku band

from Location 2 using an October master (Figure 5.16). A comparison of Figures 5.16 and 5.17 shows the improved signal coherence obtained with the C-band system. However, as noted previously, the improved coherence comes at the cost of lower resolution measurements. Quantitative coherence values measured with the two systems are compared in Figure 5.18. The quantitative results confirm that over the short and long terms, the C-band system maintains coherence better than the Ku-band system. The Ku-band device maintains high coherence in the riprap face in the short term, but over time these points degrade, while the C-band tends to maintain high values over time (with the exception of point R1). In the vegetated areas, the single day and 1 month C-band coherence values are higher than the Ku band values, but fall to similar low levels (0.3) for the 4 month span.

The results from the coherence study show that periodic monitoring of dams with a riprap surface using timespans of five months or more between measurements is feasible using either the Ku or C-band system. However, both the Ku band and C-band failed to provide adequate coherence levels for measurements of vegetated surfaces over long-term measurement (4-months). It should be noted that the C-band data collected in this study was very limited and additional studies of the C-band device on vegetated slopes should be performed.

5.3.5 Discussion of Processing Issues using Post-Unwrapping Stacking Method

The purpose of this section is to illustrate and discuss the reasons why the default processing procedure (i.e. post-unwrapping stacking technique), did not work in some cases, and the specific alternative methods that were employed. The post-unwrapping

technique is described in detail in Section 5.2.1. Generally, this procedure follows a typical approach of unwrapping interferograms and then stacking them to produce higher quality results. The specific instances where the default procedure did not work are presented in Tables 5.4, 5.5, and 5.6. Figure 5.19 presents an example of a single interferogram that was processed using the default approach, but produced a fatal unwrapping error. This single interferogram is representative of the entire set of Location 1 data for the September 2011-October 2011 timespan. The fatal unwrapping error was believed to stem from large phase differences due to atmospheric changes or ramps toward the far side of the dam (Figure 5.20). Since coherent returns from the dam take up only a fraction of the scene size, the unwrapping program continued to fail as the unwrapping program has difficulty jumping over gaps of drastically different phase values in the dataset. Therefore, to overcome this issue, it was decided to combine interferograms prior to unwrapping and improve coherence over the entire dam structure. Ideally, this procedure would produce similar benefits as post-unwrapped stacking but these effects would be realized prior to unwrapping in an effort to support the unwrapping program. The pre-unwrapping stacking technique and its complications will be discussed by showing a processing example from the September-October 2011 - Location 1 dataset.

Presented in Figure 5.21 are complex interferograms generated from the September-October 2011 dataset. At this point, it is important to establish several assumptions that are made when using the pre-unwrapping stacking technique. Since interferograms are entered into a stack where only a simple average is applied to the dataset, all interferometric data are required to be similar, meaning that phase fringes

should be similar. This should be a reasonable assumption given that the data collected on each date were collected over a time frame (several hours) over which atmospheric conditions are not expected to change. Initially, all imagery shown in Figure 5.21 were entered into the averaged stack, but after thoroughly checking individual complex interferograms not every interferograms met the general assumption required for this technique. Two of the complex interferograms (005 and 007) showed different phase trends, suggesting that atmospheric conditions did vary over the short time span of the data collection, while two other interferograms (001 and 002) indicated a coregistration error. Therefore, images 001, 002, 005, and 007 were removed from the eligible images that could be entered into the stack. After these images were removed from the stack, the stack was successfully unwrapping and the clear phase signature shown in Figure 5.6(b) was developed.

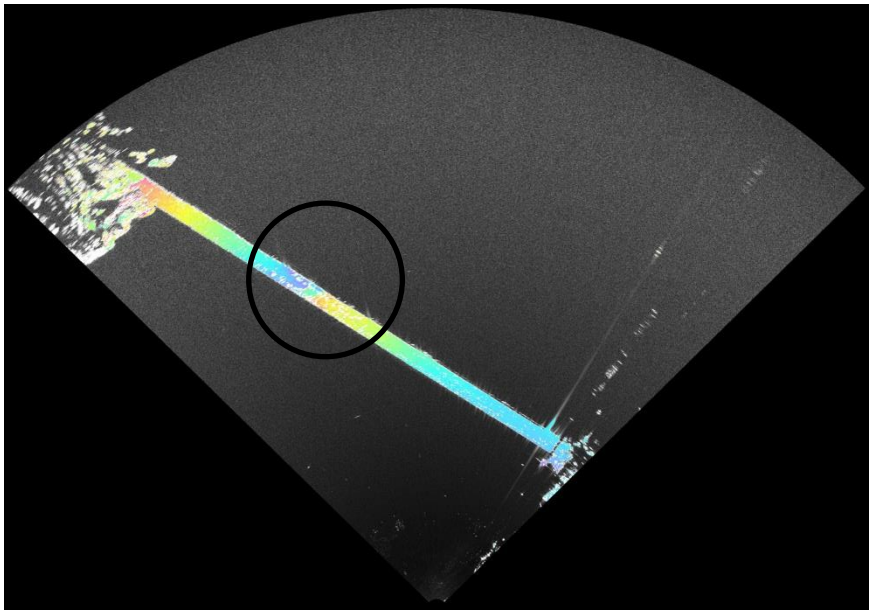

Figure 5.19 Example of failed post-unwrapped interferogram. Unwrapping error is shown inside the black circle.

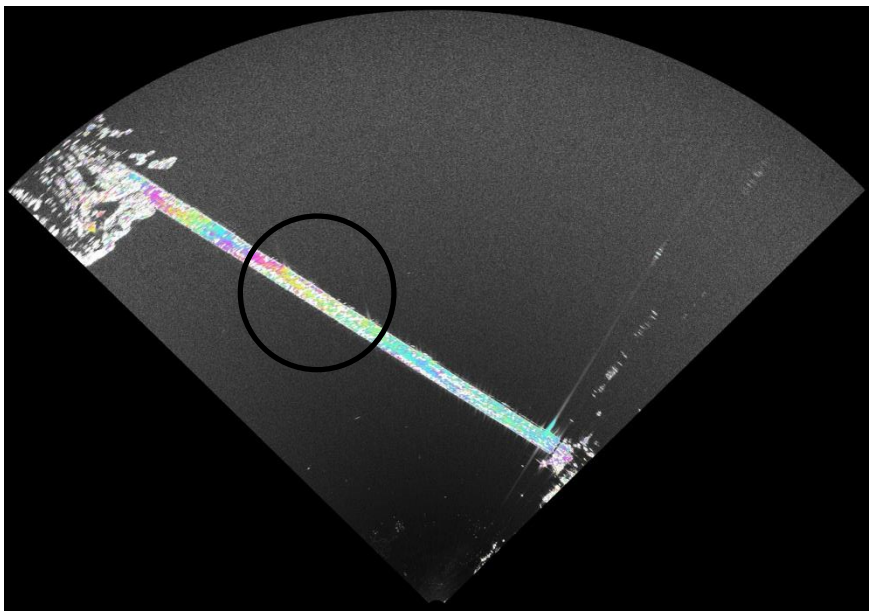

Figure 5.20 Example of single wrapped interferogram with an atmospheric ramp. Black circle indicates area where dropped data points create area where unwrapping program failed.

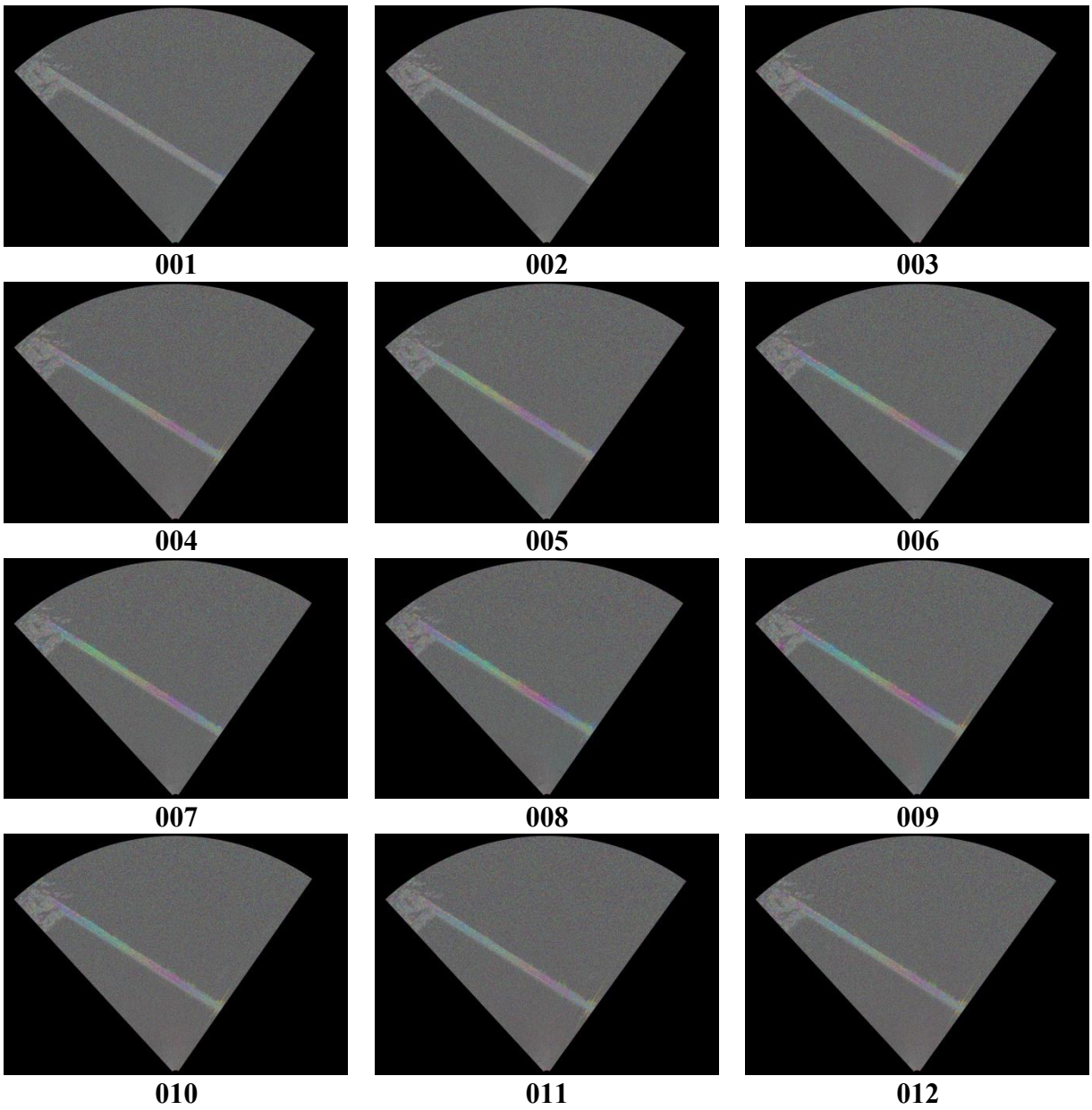

Figure 5.21 Complex interferograms input into first pre-unwrapping procedure stacking attempt (September-October 2011 timespan)

5.4 Summary and Conclusions

In this chapter, data collected from the reservoir side of a large embankment dam in Kansas were presented and discussed. During the observation period, reservoir pool levels decreased approximately 12 feet, which provided an opportunity to observe

possible small-scale embankment deformations caused by the reduction in pool level. In addition to phase measurements, coherence measurements were also acquired to study changes over time and assess the viability of using GBIR for repeat setup, periodic monitoring of dams. The data collected at the embankment dam were acquired primarily using the Ku-band device, but limited data were also collected using the C-band extension.

After data collection and analysis, it was clear that the repeat setup collections from the tripod system yielded high quality data, and did not present major coregistration problems. Therefore, this setup appears to be a viable approach for performing periodic monitoring of earth dams. During the observation period, reservoir levels decreased approximately 12 feet, during which time a probable mm-scale deformation was detected. However, measurements from other time spans did not show the same phase anomalies. Coherence measurements from the riprap embankment surface remained at or higher than acceptable levels which suggests that long-term monitoring of earth dams is viable for riprap covered embankments. Vegetated slopes could pose problems, as coherence data for vegetated areas showed levels at or below acceptable coherence levels. Atmospheric effects posed a major problem at this site, and appeared to change over short time spans (i.e. minutes). Due to the limited area of coherent radar returns in the imagery caused by the large water surface and embankment shadowing, conventional unwrapping techniques were problematic. In some cases, stacking of images with similar phase trends before unwrapping was required to overcome unwrapping issues. Based on limited comparisons of C and Ku-band devices, the C-band system, as expected, yielded higher coherence

levels than the Ku-band device. However, the coherence levels measured in vegetated areas were not greatly improved by using the C-band system.

Chapter 6: Monitoring Thermal Expansion of a Geosynthetic Landfill Liner

6.1 Introduction

The previous chapters focused on evaluating the application of GBIR for monitoring natural geotechnical materials such as soil, rock, and grassy slopes. In this chapter, results are presented from measurements at a site where the material of interest is a massive (approximately 409,464 ft^2) man-made geosynthetic landfill liner installed as part of a new bioreactor cell at the City of Columbia Landfill in Columbia, Missouri. The primary objective of this study was to assess the viability of using GBIR to detect and measure movements caused by thermal expansion of the geosynthetic liner. Geosynthetic liners are a common component in composite landfill liners, typically used in conjunction with compacted clay liners (Take, et al., 2012). During construction of composite liner system, geosynthetic liners are exposed to sunlight (for several days in some cases), and expand causing wrinkles in the liner, which can create difficulties with seaming as well as increase leakage rates through the liner system (Take, et al., 2012).

A single multi-hour long setup was used to measure movements associated with thermal changes, and document coherence changes as a result of the liner movement. To the author's knowledge, this is the first application of GBIR for monitoring landfill liner systems. Presented below is a description of the site, data collection procedures, and data processing procedures. Results from the displacement and coherence measurements are presented and discussed.

6.2 Description of Landfill Site

The City of Columbia, Missouri operates a 107-acre solid waste sanitary landfill, shown in Figure 6.1. The current disposal cell (Cell 4) was designed as a bioreactor facility, where liquids are added to the waste to accelerate decomposition and produce methane gas at a faster rate than is currently being generated in the older dry-tomb landfills (U.S. Environmental Protection Agency, 2012). Columbia started construction of a second bioreactor cell (Cell 5) in Summer 2011 (City of Columbia, 2012). The liner system for the bioreactor cell is designed to isolate the waste and collect and drain leachate that moves through the landfill. The landfill liner system consists of a 3-ft thick compacted clay liner overlain by a geosynthetic liner. The compacted clay liner was constructed with three drainage trenches (Figure 6.6), which will be used to collect leachate and recycle that leachate through the cell. The drainage trenches were cut approximately 1 feet into the compacted clay liner. The geosynthetic liner was placed in approximately 30 feet wide sections using a modified skid loader, and was laid from right to left in strips, as shown in Figure 6.2. The geosynthetic liner is approximately 50 mm thick. Different sections of the geosynthetic liner were connected via welded seams. Overlying the geosynthetic liner is a geotextile, which is similar to thin fabric.

Following installation of the geosynthetic liner and geotextile, a gravel drainage layer will be placed on top of the geotextile. One of the concerns during the construction of a liner system is the potential for excessive wrinkling of the geosynthetic prior to gravel backfilling due to thermal expansions. Void formation between the geosynthetic and clay may persist after installation of the gravel and waste, as documented in Take, et al. (2012).

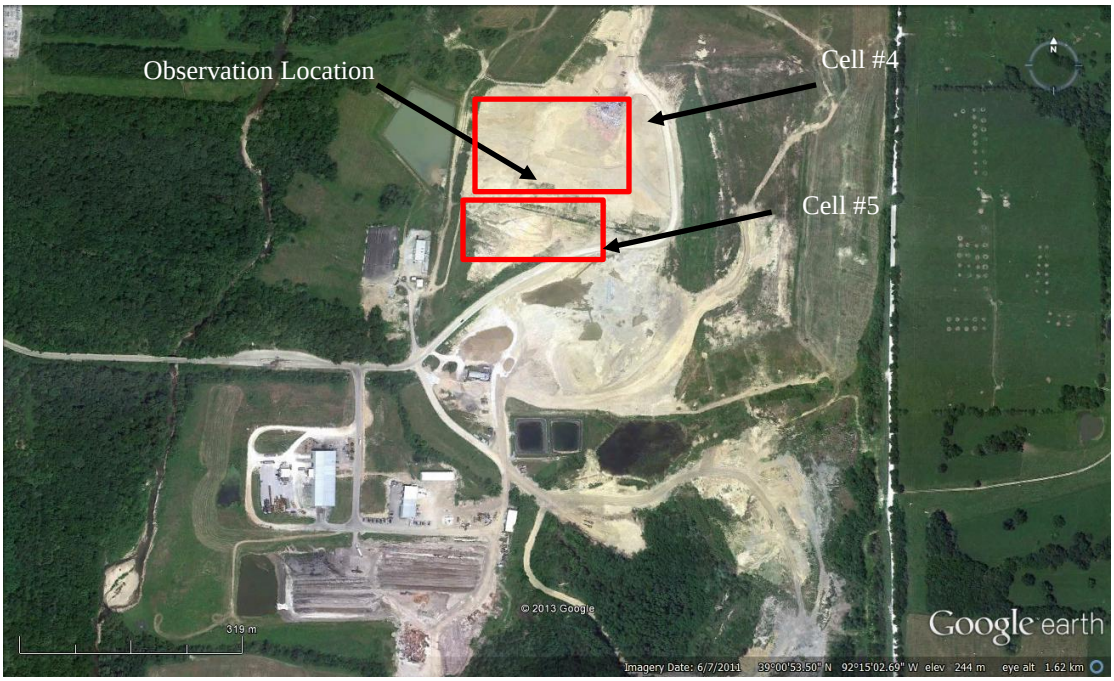

Figure 6.1 Google Earth image of the landfill complex with the area of interest (i.e. Cell 5) denoted with a red rectangle. Landfill Cells 4 and 5 are denoted by red boxes, and the observation location of the radar device is indicated with a black arrow.

Figure 6.2 Looking onto the site of interest (Cell 5) from Cell 4. The black surfaces are areas of the compacted clay liner overlain with geosynthetic material

6.3 Data Collection Procedures

Measurements with the GBIR were performed at this site after placement of the geosynthetic liner and prior to placement of the geotextile and gravel layer. The GBIR measurements were performed from the south side of Cell 4 about 100 feet above the geosynthetic liner in Cell 5. Figure 6.3 shows a picture of Cell 5 under construction (prior to placement of the liner) with an arrow indicating the approximate observation location of the GBIR. Figure 6.2 is a photo taken from Cell 4 near the GBIR location, which shows the GBIR equipment and landfill liner on the day of data acquisition. Specific locations information is presented in Appendix. As shown in Figure 6.2, the GBIR was mounted on the tripod and was secured with sandbags due to high winds. No monument (i.e. pin) was installed at this site because a continuous set-up was used to acquire the data. The measurements were performed on September 8, 2011 beginning at 6.50 AM, approximately 10 minutes prior to sunrise. Measurements were acquired every 5 minutes over a span of 1.5 hours. In total, 17 images were collected. The weather on September 8, 2011 was sunny and windy after sunrise, but prior to sunrise the area was cool with little wind. The air temperature was approximately 47°F before sunrise, and 70°F near the end of the study. Meteorological data were collected using a portable data logger that recorded temperature, humidity, wind, and precipitation data. All GBIR data were collected using a single continuous setup (i.e. the equipment was not broken down and repositioned). As shown in Figure 6.3, the radar had the ability to sweep approximately 180°, capturing the entirety of the landfill liner in each image.

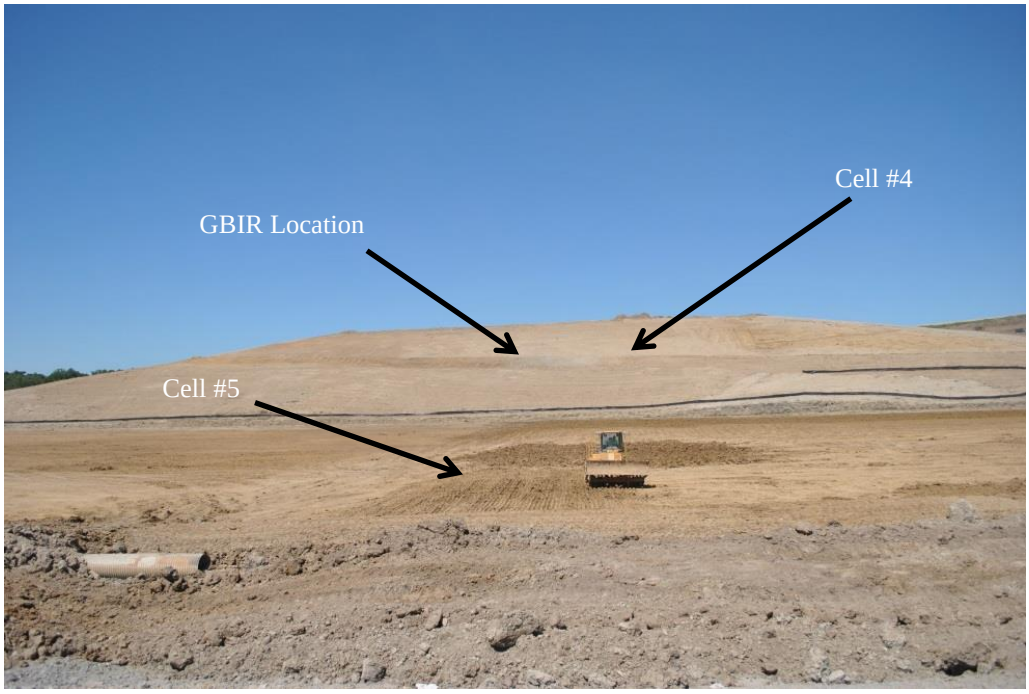

Figure 6.3 Photo taken prior to placement of geosynthetic in Cell 5 (near ground) with future location of the GBIR on Cell 4 indicated.

6.4 Data Processing Procedures

Radar data acquired at the landfill site were processed in accordance with procedures outlined in Section 2.4. All collected imagery were coregistered to the first image collected on September 8, 2012. Each progressing SLC was interfered with the master scene, generating 11 interferograms. The landfill data were multi-looked at 1 and 10 (Table 6.1). The higher multi-looking allowed data file sizes to be pared down, as well as reduced radar noise in the interferograms. Once the interfering process was completed, each interferogram underwent spectral filtering using an 8 x 8 pixel window, which is the smallest size available in the GAMMA software (Table 6.1). Since noise was a concern due to the rapidly changing surface, a composite filter was utilized, meaning both a coherence mask and intensity threshold was set to cull erroneous data. This type

of filter removed most of the phase noise (shown as random speckle), but the composite filter inadvertently removed some coherent signal that did not meet the intensity threshold (i.e. coherent signal but low intensity). After the filtering process was completed, each interferogram was unwrapped with no major problems were observed during this stage. After unwrapping, large radial phase ramps indicative of atmospheric path delays were manually identified. An atmospheric phase model (Table 6.1) was fit to each interferogram and then removed from the interferograms.

Table 6.1 **Processing details for Columbia Landfill data.**

Dataset	Interferogram Looks	Filter Used/ Window Size	Validity Mask Used (Coherence /Intensity Threshold)	Filter Coefficient Used	Atmospheric Phase Model Used
Columbia Landfill	1 & 10	Spectral/ 8	0.30/0.25	0.5	0: a0 + a1*x + a2*y + a3*x*y + a4*x^2 + a5*y^2

6.5 Field Measurement Results

A radar intensity image of the reference scene showing the landfill liner is presented in Figure 6.4. Specific regions of interest are noted in this figure, including the location of the radar and the locations of three drainage trenches. The geosynthetic liner was restrained in the field using sandbags placed in the drainage trenches, as shown in Figure 6.6. To aid the reader in interpreting the radar image, photos of the same scene taken from the vantage point of the radar are presented in Figures 6.5 and 6.6. These photos show the left side (denoted as “Side A”) and the right side (denoted as “Side B”) of the liner as seen from the radar point of view, as well as the drainage trenches where the liner was restrained from movements due to the placement of sandbags in the

trenches. As mentioned in Section 6.3, the first measurement was performed at 6:50 AM prior to sunlight hitting the landfill surface. Approximately 10 minutes after the scanning commenced, sunlight came into contact with Side B and gradually moved to Side A, over the course of the study. Ambient air temperature and relative humidity measurements collected at the time of each scan are shown in Figure 6.7. The air temperature ranged from 47°F to 70°F during the approximately 2 hour study. Unfortunately, it was not possible to collect temperature measurements on the surface of the landfill liner, which would have been preferred.

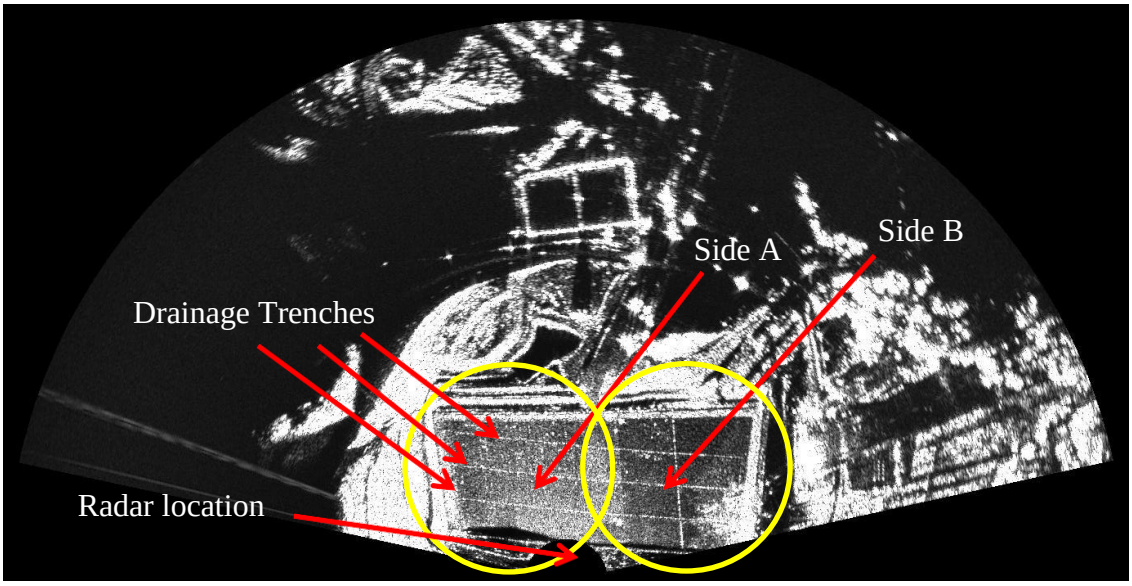

Figure 6.4 Radar intensity image with areas of the landfill liner denoted.

(a) **(b)**

Figure 6.5 Photographs of (a) left side "Side A" and (b) right side "Side B" of landfill geosynthetic liner. Photographs collected days after radar imagery collection.

Figure 6.6 Zoomed-in view of geosynthetic liner, showing drainage trenches with sandbags in the trenches restraining movement of the liner.

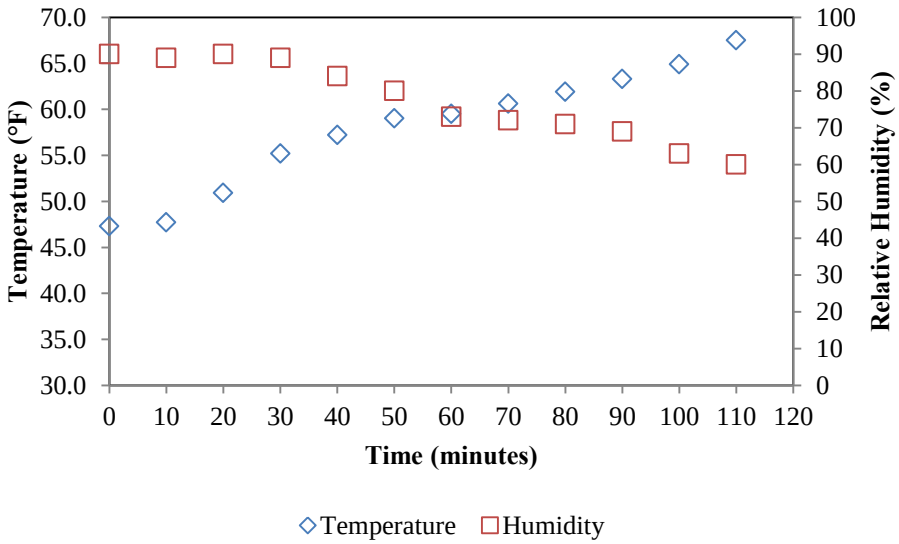

Figure 6.7 Ambient air temperature and relative humidity logged at radar location during September 8, 2011 landfill acquisition. Time zero is at 6:50 AM.

The unwrapped interferograms generated from the dataset acquired at this site showed strong atmospheric phase trends. As explained in Chapter 2, these atmospheric path delays are manually identified by radial phase fringes emanating from the observation location. Atmospheric phase contributions were expected as the temperature and humidity changed at the observation location during the morning hours (Figure 6.7). Three examples of unwrapped interferograms prior to removal of atmospheric phase are presented in Figures 6.8(a)–(c). The range-dependent color banding in these images is a hallmark of atmospheric effects. This trend was removed using the approach discussed in Section 6.4, resulting in the interferograms shown in Figures 6.8(d)-(f). From these figures, it can be observed that in the first five minutes no measurable movements occurred in the scene, as indicated by the uniform cyan color. At 30 minutes and 55 minutes, color changes in the liner portion of the image indicate movements of the liner.

With atmospheric contribution

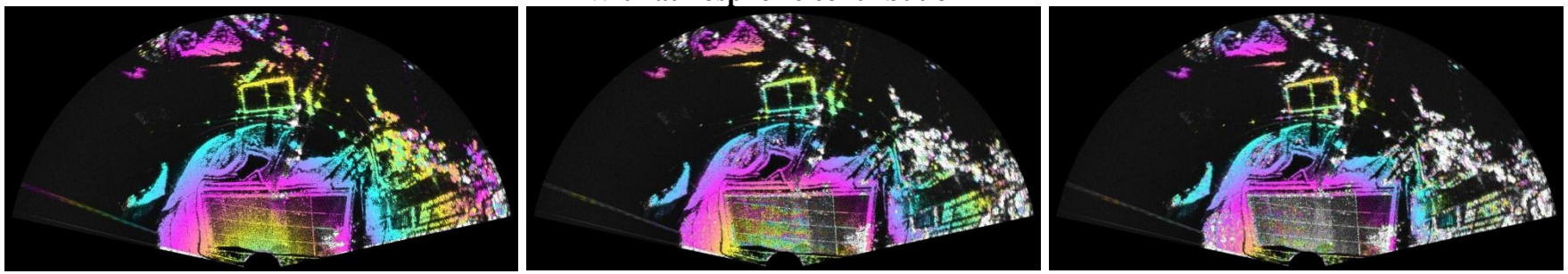

(a) 5 minutes **(b) 30 minutes** **(c) 55 minutes**

Atmospheric contribution removed

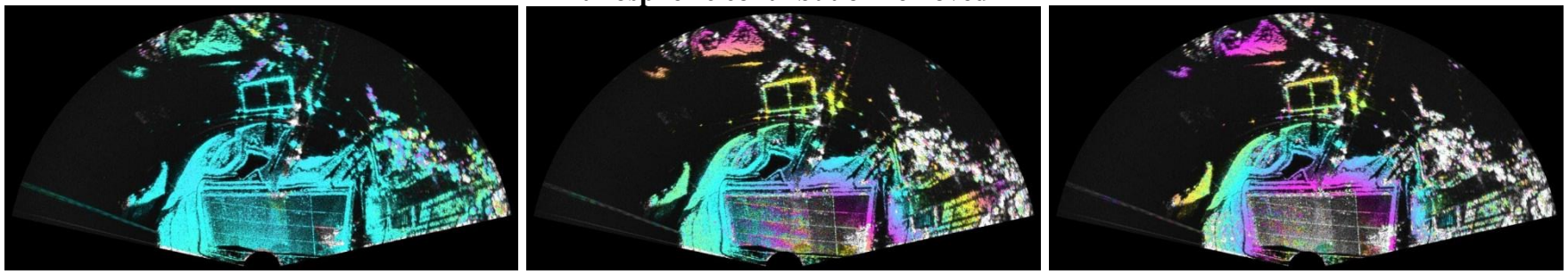

(d) 5 minutes **(e) 30 minutes** **(f) 55 minutes**

Figure 6.8 Unwrapped interferograms at 5 minutes, 30 minutes and 55 minutes after time zero, without atmospheric trend removed (a-c) and with atmospheric trend removed (d-f)

Zoomed-in views of the unwrapped interferograms at several time intervals (relative to the master image) showing only the liner portion of the radar image are presented in Figure 6.9. At five minutes, no changes in the liner are evident. At fifteen minutes, when the sun first moves across the liner, phase anomalies are evident on the right hand portion of the liner. The phase anomalies become more pronounced with time and propagate across the liner as the sun moves across the liner. It is also evident from these images that the deformations are localized around the drainage trenches where the liner is restrained from movement. The Ku-band frequency system utilized in this study has a wavelength of 17.2 mm meaning that one complete cycle of phase corresponds to almost 8 mm of displacement in the light-of-sight. The areas shaded in yellow represent approximately 2 mm of line-of-sight displacement, while the maroon areas are closer to 6 mm of line-of-sight displacement towards the radar. Although no ground truth data were available, from visual observations of the liner deformations it can be assumed that the liner deformations were primarily in the vertical direction.

The images shown in Figure 6.9 also show that with increasing time the coherence of the radar returns drops below the threshold of 0.3 used in this study. This can be seen by the increasing extent of the masked-out regions, which seem to propagate from right to left with time, ultimately resulting in the 55 minute interferogram having areas of limited coherent returns. Images of coherence as a function of time are shown in Figure 6.10. Yellow areas indicate high coherence (over 0.7), purple areas exhibit good coherence (0.4-0.7), blue areas are poor coherence (0.0-0.4), and areas of zero coherence are shown in black.

Average coherence values from five regions on the liner (shown in Figure 6.11) were quantified and plotted as a function of time, as shown in Figure 6.12. The rapid decrease in coherence with time is indicated in these figures. Low-intensity coherent points (over the coherence threshold, but under the intensity threshold) did not survive the filtering process. An example of this is shown in Figure 6.9(i), where the whole right side of the liner is masked, while in Figure 6.12 all points are generally above the coherence threshold, indicating that while these points are above the coherence threshold, they are of low-intensity. As mentioned above, this composite mask was necessary to avoid noise contamination.

Portions of the liner selected for time-dependent coherence monitoring are shown in Figure 6.11 with the quantified values presented in Figure 6.12. Values in Figure 6.12 were calculated by averaging 13 individual coherence values of adjacent pixels for each point in Figure 6.11. Figure 6.12 shows coherence dropping over the observed timespan in Side B before Side A.

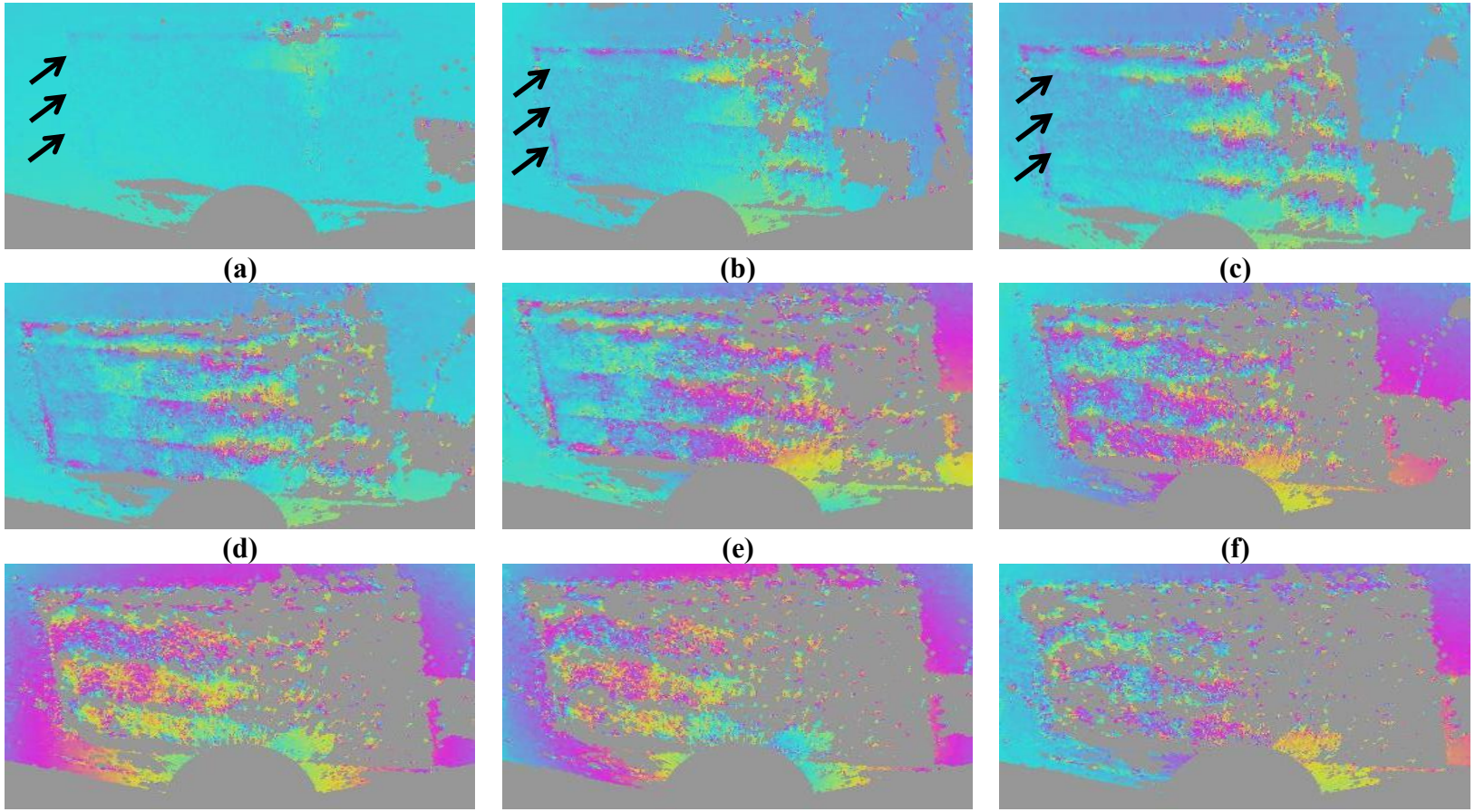

Figure 6.9 Zoomed-in view of Figure 6.8 capturing landfill liner at different acquisition times, relative to the time zero: (a) 5 minutes, (b) 15 minutes, (c) 20 minutes, (d) 25 minutes, (e) 30 minutes, (f) 35 minutes, (g) 40 minutes, (h) 45 minutes, (i) 50 minutes. Drainage trench

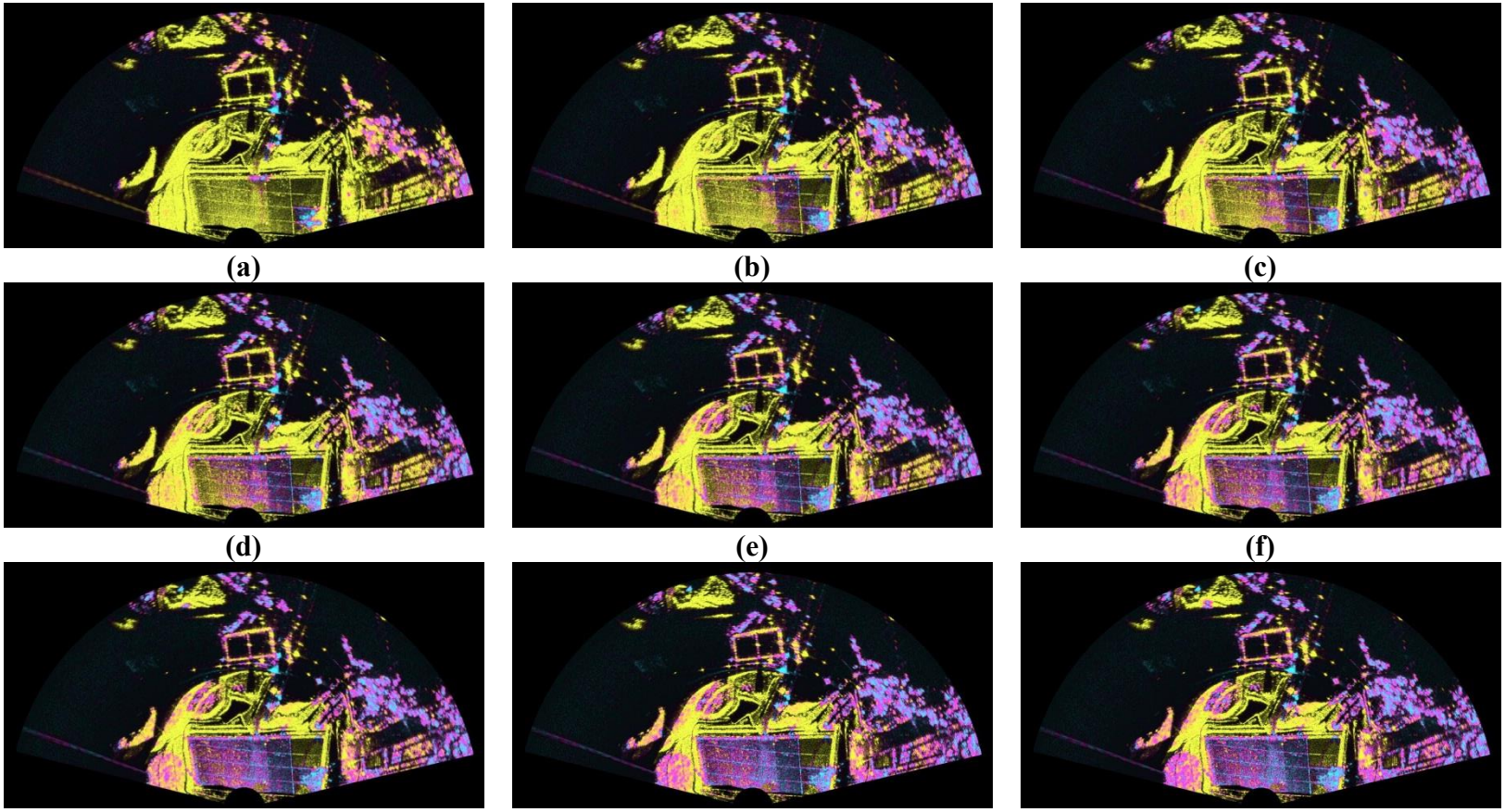

Figure 6.10 Spatial coherence of the entire scene at: (a) 5 minutes, (b) 15 minutes, (c) 20 minutes, (d) 25 minutes, (e) 30 minutes, (f) 35 minutes, (g) 40 minutes, (h) 45 minutes, (i) 50 minutes. Yellow areas represent coherence values from 0.7-1.0, purple represents values from 0.4-0.7, blue represents values from 0.0-0.4, and black represents areas of zero coherence.

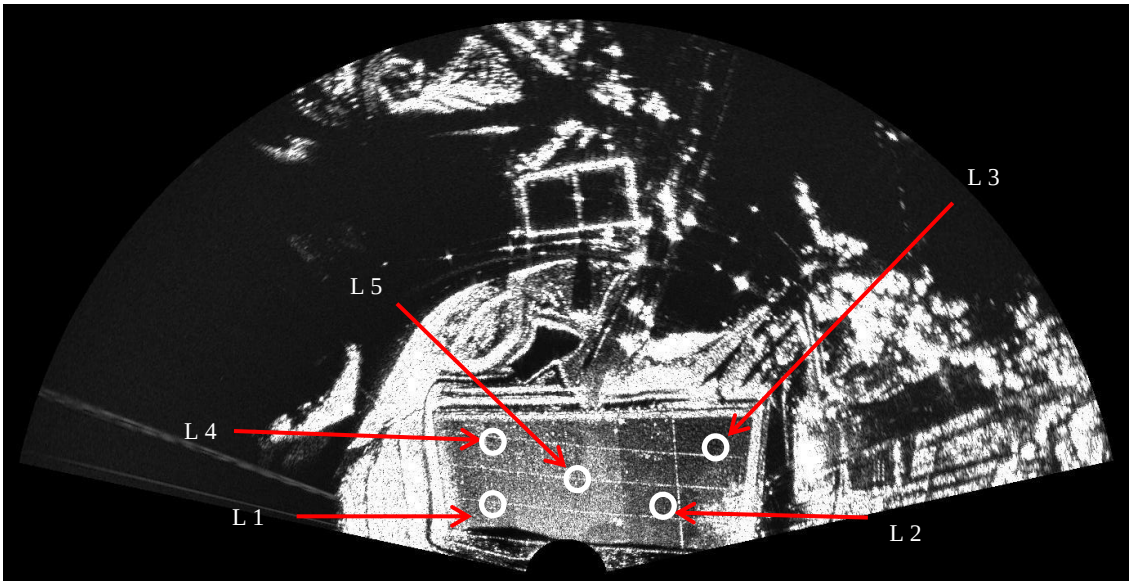

Figure 6.11 Intensity image acquired on September 8, 2011 with areas of monitored coherence indicated

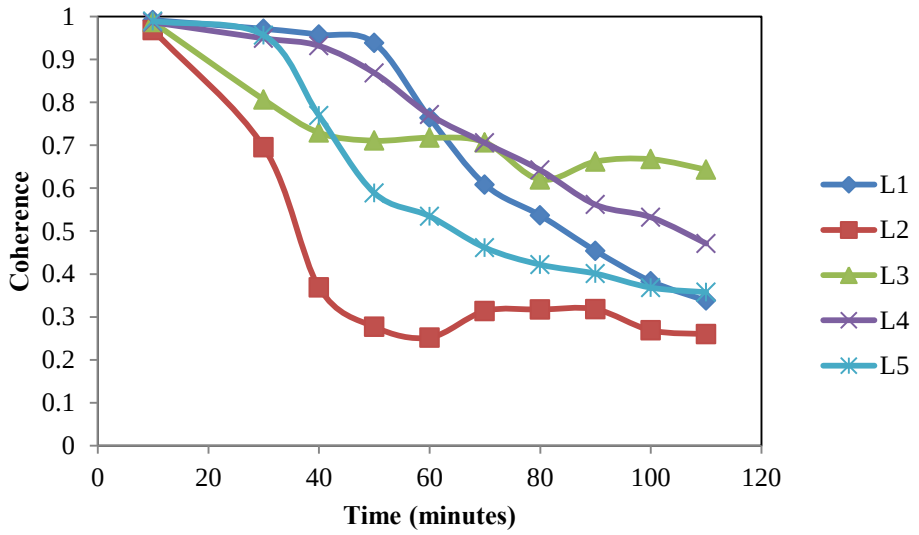

Figure 6.12 Coherence values for selected points on landfill liner over acquisition period. All points are on landfill liner, and are referenced in Figure 6.11.

6.6 Discussion of Field Measurements from Landfill Liner

This study focused on observing displacements of a landfill liner due to thermal variations on the liner. The results show that only 5 minutes of direct sunlight on the liner

resulted in displacements of approximately 2 mm in the radar line-of-sight, as shown in Figure 6.9(b). By the end of the study, after more than 50 minutes of sunlight exposure, several areas of the landfill liner showed displacements of approximately 8-mm (line of sight), as shown in Figure 6.9(i). Most of this movement is presumably in the vertical direction, as observed deformations appeared to be in the vertical direction. This assumption is consistent with findings presented in Take et al. (2012), which show that the liner tends to buckle immediately prior to imperfections (i.e. drainage trenches) in the compacted clay liner (Figure 6.13). It is important to note that the radar was only able to capture a portion of this vertical motion as the radar device emits a radar wave that is oblique to the assumed motion.

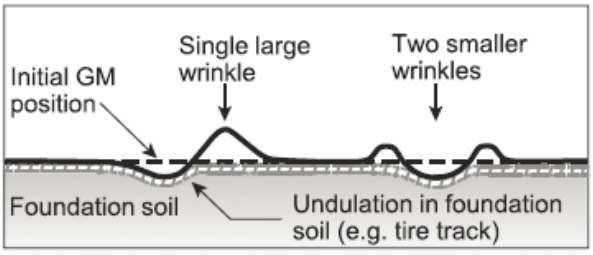

Figure 6.13 Geosynthetic liner effects near drainage trenches. After Take et al. (2012).

Previous research by Take et al. (2012) show that a majority of liner strains caused from temperature changes were in the vertical direction. These documented strain values presented in Take et al. (2012) were on the order of tens of millimeters as a result of an approxmiately 40°F increase in surface temperature of the liner. In this study, the actual changes of the liner tempertaure were not known, but were likely much higher than changes in air temperature. Take et al. (2012) presented data showing that wrinkes less than 20mm willAfter taking into consideration the fact that changes in ambient air

temperatures recorded in this study were likely lower than actual changes in the geosynthetic surface temperature, and the fact that the radar device only captured a component of the vertical motion, the displacement values presented in this chapter are plausible, when compared to Take et al. (2012).

Another portion of the liner study concerned changes in coherence during thermal displacement of the liner. In the first minutes of the study (Figure 6.12), coherence remained high for all areas, but as temperature increased coherence tended to decrease over areas of the liner (Figure 6.12). The large coherence changes are likely the result of the changing shape and geometry of the buckling landfill liner, which caused alterations in the backscatter properties. These coherence changes first manifested in the right portion of the liner, as sunlight initially contacted the geosynthetic liner surface in the initial 25 minutes of the study. As time progressed (and sunlight contacted the entire liner), coherence degraded over the center and left areas, as seen in Figure 6.10. These locations of the coherence changes mimic trends already discussed concerning displacement results, therefore it appears that movement of the liner is the main cause of coherence loss. It is important to note that the coherence data suggests that most coherence points are above acceptable minimum coherence levels (0.3 in this study). In this study, some coherent areas were masked because of the composite mask employeed in order to remove random phase.

The standard processing flow described in Chapter 2 to develop interferograms worked well as this site. No additional techniques or modifications were required to successfully process the data. Removal of atmospheric phase contamination in the landfill data was required to ensure that unwrapped phase data did not include

components of atmospheric path delay, which would induce apparent displacement of the liner. The data presented in Figure 6.8(a), (b), and (c) exhibit classic signs of atmospheric path delay (radial phase gradients emanating from the observation point), which was expected because temperatures and humidity changed over the course of the radar survey. A quadratic phase function (Table 6.1) was fit to the unwrapped phase data, and succesfully eliminated most of the atmospheric contamination (Figure 6.8(d), (e), and (f)) when it was subtracted from the interferograms. Areas near the landfill liner appear to have the atmosperhic phase contamination successfully removed, while areas further away from the observation point still exhbit an atmospheric path delay. The atmosperhic path delay residues are a result of the function not completely removing the contamination, as meteorological conditions were most likely not uniform over the entire site.

6.7 Summary and Conclusions

Ground-based radar measurements were applied to a geosynthetic liner for a new bioreactor cell that was under construction in Columbia, MO. Data were acquired using the Ku-band frequency device. The landfill liner was monitored at 5-minute intervals for a period of approximately 2 hours during which the air temperature and humidity increased as well as the liner temperature from direct sunlight. The interferometric results showed phase anomalies that began to appear as direct sunlight illuminated the liner surface. The phase anomalies in the interferograms propagated across the liner as the sunlight moved across the liner. The anomalies were most pronounced near trenches where the liner was restricted from movement. The initial phase anomalies correlated to

line-of-sight movements of 2 mm, while later observations showed movements of about 8 mm. The movements were interpreted to be caused by wrinkling of the liner near the drainage trenches, because of thermal expansion. Changes in coherence were measured and also showed a trend that seemed to propagate across the liner. The decrease in coherence with time was likely due to the changes in shape of the liner caused by the thermal expansion and wrinkling of the surface, which affected the backscattering properties of the liner.

This dataset has provided an unprecedented view of the thermal changes that take place in a large geosynthetic liner under thermal loading. Ground-based interferometric radar could be a very useful technology to monitor liner movements to ensure they do not exceed a given threshold prior to placement of the gravel layer. Take, et al. (2012) suggest that liner displacements of approximately 20mm or less will not result in wrinkling, and that larger displacements will result in wrinkling on the liner. Based on the results of this study, radar signal is likely to decorrelate when processed using a single master where displacements larger than 20mm are observed. Improved coherence is expected when a time-series approach (i.e. multiple masters) is employed.

Chapter 7: Conclusions and Future Work

7.1 Summary

The overall objective of this research was to evaluate and document the performance of GBIR for civil engineering applications that are not well represented in the current literature. Three possible applications of GBIR were investigated in this thesis, namely: (1) monitoring and detecting movements of unstable rockslopes, (2) performing periodic deformation monitoring of earth dams, and (3) measuring thermal movements of a massive geosynthetic liner during construction of a landfill. No published studies of GBIR for these applications were found in the literature. Specific objectives of this study were to: (1) quantify changes in coherence over short, intermediate and long terms, (2) assess the viability of using repeat setup data collection method, and (3) identify pitfalls in conventional data processing methods and evaluate alternative data processing strategies

Data were collected at three sites using the Ku-band GBIR system manufactured by GAMMA Remote Sensing, Inc. Each site discussed in this study was composed of different surficial materials, including rock slopes, riprap, vegetated areas and a geosynthetic landfill liner. For each site, unwrapped interferograms and spatially-derived coherence imagery were generated over different timespans, which ranged from minutes to several months. At one site, C-band GBIR data were acquired in addition to Ku-band data, which allowed for limited multi-frequency comparisons of deformation and coherence data. Deformation and coherence measurements for each site were presented

and discussed in separate chapters. Data processing techniques and strategies were reviewed for each site and discussed.

7.2 Conclusions

In general, the GBIR radar measurements were successfully performed at each of these sites and yielded high quality data and meaningful interferograms. Specific conclusions are presented below for each of the three studies that were performed.

GBIR for Rockfall Monitoring:

- Repeat setup data collection from a mast installed at this site yielded high quality data and did not present problems during coregistration and processing of data. This appears to be a viable approach for performing repeat setup measurements at rock slope sites.
- No movements of the rock slope in excess of approximately 0.25 inch were observed during the month-long data acquisition. Phase changes consistent with movements of less than 0.25 in. were observed at a few points on the slope but could not be confirmed with ground truth measurements.
- Coherence remained high (0.7 or greater) on the rock slope portion of the scene throughout the one-month measurement campaign, while vegetated regions decorrelated over the two week to month long intervals.
- Atmospheric effects were significant enough to require removal before the scenes could be interpreted

GBIR for Long-term Monitoring of Earth Dams:

- Repeat setup data collection from using the tripod yielded high quality data and did not present major problems in coregistration and processing of data. This appears to be a viable approach for performing periodic monitoring of earth dams
- During a period of decreased pool level, a probable mm-scale deformation of a dam embankment was detected. However, measurements over longer time intervals did not show the same phase anomalies.
- Coherence over the riprap embankment surface remained at or higher than acceptable levels over the span of five months, while coherence over vegetative surfaces was below acceptable levels. These results suggest that long-term periodic monitoring of earth dams is viable for sites with riprap embankments but may not work for grass-covered slopes.
- Atmospheric effects were very significant at this site and atmospheric conditions appeared to change over the span of minutes in some cases.
- The limited area of coherent radar returns (due to water and shadowing effects) in the dam imagery caused problems when using conventional processing techniques. Stacking of images with similar phase trends prior to unwrapping overcame this problem in some cases.
- Limited comparisons of the C-band system to the Ku-band system showed the expected result of higher coherence at the cost of lower resolution. In addition, coherence of the vegetated areas did not improve greatly with the C-band device.

GBIR for Monitoring Thermal Movements of a Geosynthetic Landfill Liner:

- Interferograms collected over a 1.5-hour span at 5 minute intervals showed movements that progressed across the liner as sunlight moved across the geosynthetic liner.
- The movements appear to be due to wrinkling and buckling of the liner and were more pronounced at trenches where movement of the liner was restricted.
- Coherence was initially high but decreased below threshold values with time. The progression of coherence changes across the liner suggests the loss of coherence was due to large changes in the shape and backscattering characteristics of the liner as it deformed.
- The loss of coherence due to large deformations of the liner, and use of a single master may limit the applicability of this method where large movements (20 mm or greater) are of most interest. However, use of multiple masters should maintain coherence over longer timespans, allowing larger deformations to be detected.
- Standard processing of the data and atmospheric phase removal methods worked well at this site.

7.3 Recommendations

Based on the findings documented in this thesis, the following recommendations are made for future studies of GBIR in civil engineering applications.

- Measurements should be performed at sites where reliable ground truth data is available. For example, kinematic GPS and optical survey measurements could be

performed. Including ground truth into future studies will also help define the accuracy and precision of the GBIR measurements.

- Further data should be collected using the C-band device in order to definitively draw conclusions about deformation and coherence results presented in this thesis, as only a very limited study was conducted.
- Accurate meteorological data should be acquired at each site using an automated data logging device. Meteorological data can be used in a forward model for more accurate atmospheric phase contribution simulation and removal. This approach should be conducted on both repeat-pass and single time-series studies.
- For applications requiring high spatial coherence (e.g. rockslope and earth dams cases), use of a pixel-by-pixel calculation of coherence from multiple images should be studied to improve interferogram quality prior to phase unwrapping.
- The geosynthetic liner dataset should be reanalyzed using a time-series processing approach. This scheme should employ multiple masters, and could potentially improve coherence over larger timespans, thereby allowing greater deformations to be detected.

REFERENCES

Alba, M. et al., 2008. *Measurement of Dam Deformations by Terrestrial Inteferometric Techniques.* Beijing, The International Archives of the Photogrammetry, Remote Sensing and Spatial Information Sciences .

Bamler, R. and Hartl, P., 1998. Synthetic Aperature Radar Interferometry. *Inverse Problems,* Volume 14, pp. R1-R54.

Blacus, V., 2012. *Electromagnetic Spectrum.* [Online]
Available at: http://en.wikipedia.org/wiki/Electromagnetic_spectrum
[Accessed 06 June 2013].

Bozzano, F., Mazzanti, P., Prestininzi, A. and Scarascia Mugnozza, G., 2010. Research and Development of Advanced Technologies for Landslide Hazard Analysis in Italy. *Landslides,* Volume 7, pp. 381-385.

Casagli, N., Catani, F., Del Ventisette, C. and Luzi, G., 2010. Monitoring, Predicition, and Early Warning Using Ground-Based Radar Interferometry. *Landslides,* 7(3), pp. 291-301.

Casagli, N. et al., 2003. *Ground-Based SAR Interferometry as a Tool for Lanslide Monitoring During Emergencies.* Toulouse, IEEE.

City of Columbia, 2012. *Landfill and Compost Facility.* [Online]
Available at:
http://gocolumbiamo.com/PublicWorks/Solidwaste/sanitarylandfill.php
[Accessed 06 October 2012].

Coffman, R. A., 2009. *Processing of Synthetic Aperture Radar Data as Applied to the Characterization of Localized Deformation Features,* Columbia: University of Missouri-Columbia.

Corsini, A. et al., 2006. Space-Borne and Ground-Based SAR Interferometry as Tools for Landslide Hazard Management in Civil Protection. *International Journal of Remote Sensing,* 27(12), pp. 2351-2369.

Del Ventisette, C., Casagli, N., Fortuny-Guasch, J. and Tarchi, D., 2011. Ruinon Landslide (Valfurva, Italy) Activity in Relation to Rainfall by Means of GBInSAR Monitoring. *Landslides, Online First,* pp. 1-13.

Fielding, E. J., Blom, R. G. and Goldstein, R. M., 1998. Rapid Subsidence Over Oil Fields Measured by SAR Interferometry. *Geophysical Research Letters,* 25(17), pp. 3215-3218.

GAMMA Remote Sensing AG, 2001. *GAMMA Portable Radar Interferometer II (GPRI-II),* Guemligen: GAMMA Remote Sensing AG.

GAMMA Remote Sensing AG, 2007. *Documentation-Theory: Interferometric SAR Processing,* Gumligen: GAMMA Remote Sensing AG.

GAMMA Remote Sensing AG, 2008. *Differential Interferometry and Geocoding Software-DIFF & GEO,* Gumligen: Gamma Remote Sensing.

GAMMA Remote Sensing AG, 2008. *SAR, InSAR, and DInSAR Processing with GAMMA Software,* Gumligen: GAMMA Remote Sensing AG.

GAMMA Remote Sensing AG, 2010. *Documentation-User's Guide: Interferometric SAR Processing- ISP,* Gumligen: Gamma Remote Sensing.

Goldstein, R. M. and Werner, C. L., 1998. Radar Interferogram Filtering for Geophysical Applications. *Geophysical Research Letters,* pp. 4035-4038.

Goldstein, R. M., Zebker, H. A. and Werner, C. L., 1988. Satellite Radar Interferometry: Two-Dimensional Phase Unwrapping. *Radio Science,* pp. 713-720.

GroundProbe, 2012. *GroundProbe: Slope Stabilty.* [Online]
Available at: http://www.groundprobe.com/slopestability.html
[Accessed 09 October 2012].

Hanssen, R. F., 2010. *Radar Interferometry.* Dordrecht: Kluwer Academic Publishers.

IDS Corporation, 2013. *Our Solutions & Products.* [Online]
Available at: http://www.idscorporation.com/georadar/our-solutions-products
[Accessed 15 June 2013].

Jenkins, W. et al., 2012. *Deformation Measurements of Earth Dams Using a Ground Based Interferometric Radar (GBIR).* Denver, Colorado, Association of State Dam Safety Officials.

Jensen, J. R., 2000. *Remote Sensing of the Enviroment: An Earth Resource Perspective.* Upper Saddle River, New Jersey: Prentice Hall.

Leib, J., 2010. *denverpost.com.* [Online]
Available at: http://www.denverpost.com/ci_14735610?source=pkg
[Accessed 08 June 2012].

Lingua, A., Piatti, D. and Rinaudo, F., 2008. *Remote Monitoring of a Landslide Using an Integration of GB-INSAR and LIDAR Techniques.* Beijing, IEEE.

Li, Z. W. et al., 2007. Atmospheric effects on repeat-pass InSAR measurements over Shanghai region. *Journal of Atmospheric and Solar-Terrestrial Physics,* Volume 69, pp. 1344-1356.

Luzi, G., Crosetto, M. and Monserrat, O., 2010. *Advanced Techniques for Dam Monitoring.* Zaragorza, Spain, II International Congress on Dam Maintenance and Rehabilitation.

Luzi, G. et al., 2007. Monitoring of an Alpine Glacier by Means of Ground-Based SAR Interferometry. *IEEE Geoscience and Remote Sensing Letters,* 4(3), pp. 495-499.

Luzi, G. et al., 2006. Advances in Ground-Based Microwave Interferometry for Landslides Survey: A Case Study. *International Journal of Remote Sensing,* 27(12), pp. 2331-2530.

McHugh, E. L., Dwyer, J., Long, D. G. and Sabine, C., 2006. *Applications of Ground-Based Radar to Mine Slope Monitoring,* Cincinnati: CDC.

Mecatti, D. et al., 2010. *Monitoring Open-Pit Quarries by Interferometric Radar for Safety Purposes.* Paris, EuMA.

Meinel, H. H., 1995. Commerical Application of Millimeterwaves History, Present Status, and Future Trends. *IEEE Transactions on Microwave Theory and Techniques,* pp. 1639-1653.

Miller, P. K., Vessely, M., Olson, L. D. and Tinkey, Y., 2013. *Slope Stability and Rock-Fall Monitoring with a Remote Interferometric Radar System.* San Diego, ASCE.

Noferini, L. et al., 2006. *Ground-Based Radr Interferometry for Monitoring Unstable Slopes.* Denver, IEEE.

Noon, D. and Harries, N., 2007. *Slope Stability Radar for Managing Rock Fall Risks in Open Cut Mines.* Perth, Large Open Pit Mining Conference.

Olson Instruments, Inc, 2012. *NDE, SHM & Geophysical Instruments.* [Online] Available at: http://www.olsoninstruments.com/ibis-l.php [Accessed 09 October 2012].

Olson Instruments, 2013. *Olson Instruments | Monitor Earth Movement.* [Online] Available at: http://www.olsoninstruments.com/ibis-l.php [Accessed 24 June 2013].

Pieraccini , M. et al., 2006. *Ground-Based SAR for Short and Long Term Monitoring of Unstable Slopes.* Manchester, EuMA.

Pieraccini, M. et al., 2003. Landslide Monitoring by Ground-Based Radar Interferometry: A Field Test in Valdarno (Italy). *International Journal of Remote Sensing,* 24(6), pp. 1385-1391.

Pieraccini, M. et al., 2004. High-speed CW Step-Frequency Coherent Radar for Dynamic Monitoring of Civil Engineering Stuctures. *IEEE Electronic Letters,* 40(14).

Pieraccini, M. et al., 2000. Interferometric Radar for Remote Monitoring of Building Deformations. *Electronic Letters,* 36(6), pp. 569-570.

Richards, J. A., 2009. *Remote Sensing with Imaging Radar.* Heidelberg: Springer.

Richards, M. A., 2005. *Fundamentals of Radar Signal Processing.* New York: McGraw-Hill.

Skolnik, M. I., 2001. *Introduction to Radar Systems.* New York: McGraw-Hill.

Stramondo, S., Moro, M., Doumaz, F. and Cinti, F. R., 2005. The 26 December 2003, Bam, Iran Earthquake: Surface Displacement from Envisat ASAR Interferometry. *International Journal of Remote Sensing,* 26(5), pp. 1027-1034.

Strozzi, T., Werner, C., Wiesmann, A. and Wegmuller, U., 2012. Topography Mapping With a Portable Real-Aperature Radar Interferometer. *IEEE Geoscience and Remote Sensing Letter,* 9(2), pp. 277-281.

Take, W. A., Watson, E., Brachman, R. W. I. and Rowe, R. K., 2012. Thermal Expansion and Contraction of Geomembrane Liners Subjected to Solar Exposure and Backfilling. *Journal of Geotechnical and Geoenvironmental Engineering,* 138(11), pp. 1387-1397.

Tarchi, D., Leva, D. and Sieber, A., 2000. SAR Interferometric Techniques from Ground Based System for the Monitoring of Landslides. *IEEE,* pp. 2756-2758.

Tarchi, D. et al., 1999. *SAR Interferometry for Structural Changes Detection: a Demonstration Test on a Dam.* Hamburg, IEEE.

Tarchi, D., Rudolf, H., Pieraccini, M. and Atzeni, C., 2000. Remote Monitoring of Buildings Using a Ground-Based SAR: Applicaiton to Cultural Heritage Survey. *International Journal of Remote Sensing,* 21(18), pp. 3545-3551.

Tedd, P., Charles, J., Watford, B. and Claydon , J., 1991. *Deformation of Ramsden Dam During Reservoir Drawdown and Refilling.* Nottingham, 6th Conference of the British Dam Society.

Teza, G. et al., 2008. Ground-Based Monitoring of High Risk Landslides Through Joint Use of Laser Scanner and Interferometric Radar. *International Journal of Remote Sensing*, 29(16), pp. 4735-4756.

U.S. Environmental Protection Agency, 2012. *Wastes-Non-Hazardous Waste-Municipal Solid Waste.* [Online] Available at: http://www.epa.gov/wastes/nonhaz/municipal/landfill/bioreactors.htm [Accessed 06 October 2012].

United States Army Corps of Engineers, 2012. *Kansas City District: Milford Lake.* [Online] Available at: http://www.nwk.usace.army.mil/Locations/DistrictLakes/MilfordLake.aspx [Accessed 03 September 2012].

United States Army Corps of Engineers, 2013. *Dam Safety Program Activities.* [Online] Available at: http://www.usace.army.mil/Missions/CivilWorks/DamSafetyProgram/ProgramActivities.aspx [Accessed 01 June 2013].

Werner, C., Strozzi , T., Wiesmann, A. and Wegmuller, U., 2008. *GAMMA's Portable Radar Interferometer.* Lisbon, LNEC.

Werner, C., Strozzi, T., Wiesmann, A. and Wegmuller, U., 2009. *A Real-Aperture Radar for Ground-Based Differential Interferometry.* Boston, IEEE.

Wolff, C., 2013. *Radar Basics.* [Online] Available at: http://www.radartutorial.eu/index.en.html#this [Accessed 26 February 2013].

APPENDIX

Table A.1 Coordinates for radar observation locations presented in this thesis.

Location	Point	Coordinates	
		Northing	Easting
Glenwood Canyon	Single Point	39.58309333	-107.19435167
Milford Dam	Location #1	39.07755167	-96.90672167
	Location #2	39.09179333	-96.89886000
Columbia Landfill	Single Point	39.01681333	-92.25027667